PRECISION MEASUREMENTS OF THE PROPERTIES OF THE HIGGS BOSON USING THE CMS DETECTOR

by
Jeffrey Davis

A dissertation submitted to The Johns Hopkins University in conformity with the requirements for the degree of Doctor of Philosophy

Baltimore, Maryland
October 2025

Abstract

The Higgs Boson, first discovered in 2012, was the first and only new fundamental particle found at the LHC since data taking began in 2009. Even promising alternative models of new physics, such as Super Symmetry, have yet to be experimentally confirmed 15 years after the LHC first started collecting data. With the apparent lack of new physics at the TeV scale, model independent, precision measurements of the Higgs boson may be the only way to provide hints about the nature of physics beyond the standard model. Effective field theory (EFT) provides a model independent framework for searching for new physics in this era of precision measurements. Rather than looking for new resonances, the effects of beyond standard model physics are characterized by small deviations in observables from the standard model prediction or enhanced rates of rare processes.

In this thesis, I will present various studies and analyses involving precision measurements of the Higgs boson's properties. First, I will detail various contributions to the tracker alignment, which is crucial for precision measurements at the LHC. Then I will present phenomenological studies applied to LHC data including contributions to the various tools (specifically JHUGen and MELA) that make my analyses and many others on CMS possible. I will show results targeting the γH production process and constraints on the Yukawa couplings of light quarks. Finally, I will present simultaneous constraints on eight anomalous couplings of the Higgs boson to vector bosons using the four-lepton final state. Results are interpreted in the EFT framework using data collected by the CMS experiment during Run 2 and Run 3 of the LHC.

Abstract

These results represent the most model independent constraints on the Higgs boson couplings to date and are the first constraints on anomalous couplings in this final state including the LHC Run-3 dataset.

Keywords: Johns Hopkins, PhD, dissertation, EFT, Higgs Boson, Yukawa couplings, CMS

Primary reader and thesis advisor

Dr. Andrei Gritsan
Professor
Department of Physics and Astronomy
Johns Hopkins University, Baltimore MD

Secondary readers

Dr. Petar Maksimovic
Professor
Department of Physics and Astronomy
Johns Hopkins University, Baltimore MD

Dr. Tobias Marriage
Professor
Department of Physics and Astronomy
Johns Hopkins University, Baltimore MD

Dr. Jacob Khurgin
Professor
Whiting School of Engineering
Johns Hopkins University, Baltimore MD

Dr. Toni Sculac
Professor
Faculty of Science,
University of Split, Croatia

This thesis is dedicated to my family, friends, collaborators, and comrades

Acknowledgment

The content of this thesis represents the bulk of the academic work I have done in the last 6 years of my life. As with any great undertaking, it truly takes a village. Support takes many forms, be it academic, monetary, spiritual, emotional, etc. and I do not distinguish any as being more important than the other. As such, it would be impossible for me to list all the names of the people who have helped me get to this point. I apologize in advance if I have forgotten to include anyone.

To my advisor, Andrei: Thank you for always pushing me to be the best scientist I could be. From the beginning of graduate school you never expected anything less than excellence from me. I admire your desire to always approach an analysis from the perspective of what is correct rather than what is easiest. You have always supported me and my scientific results and have consistently made sure that I receive recognition from the collaboration for the hard work that I do. Thank you for an amazing six years of science.

To my CJLST colleagues: It was amazing to work in such a collaborative group. In my unbiased opinion, the CJLST framework for $H \to 4\ell$ reconstruction is one of the finest products on CMS. The willingness of all of you to share expertise and do code development is something that I will not take for granted. The work in this thesis could not have been done without all of your individual contributions to the framework.

To everyone I worked with from the JHU group including Mohit, Heshy, Ulascan, Nick,

Zhiyuan, Rouxi, Lucas, Savvas, Yafou, Matej, Petar, Morris, Michalis, Markus, Toni, and others: Working with you all was such a joy. I hope we can all collaborate in the future. To the younger students in Andrei's group: I know you will do great things scientifically and I cannot wait to see your next exciting results.

To my comrades Janvi, Justin, Wisam, Begum, Lily, Lyla, Alaa, Connor, Ana, and Sandy, among others: We originally met during the TRU unionization campaign, where eventually I was convinced to become a member of the bargaining committee. We got very close during the year-long contract fight. I thank you all for restoring my faith in humanity and the possibility of a better tomorrow. Thank you for showing me the power of collective action and what true community looks like. I am honored to be your friend. I hope we realize our collective dream that one day people will no longer have to fight for the right to live with dignity.

To my amazing parents: I thank you for your unconditional love and understanding. I cannot express how much it means to me that you are only a phone call away. You always know exactly how to cheer me up during difficult times and do whatever you can to help. To my sisters, Rachel and Alison, thank you for being with me on this journey. It was amazing to watch your lives unfold over the past 6 years. I am so proud to be your big brother.

To my partner Erini: You know more than anyone how difficult this journey was. You were literally there every step of the way and without your support I don't know where I would be. Thank you for helping me stay grounded all these years. While the world crumbles around us, you make every day brighter. Thank you for showing me a

way to live without compromising who I am. I cannot wait to see what our future holds. I love you more than anything.

To the city of Baltimore: Thank you for having me. I hope that one day your relationship with JHU is no longer one of exploitation, displacement, dispossession, medical debt, and police violence. You will always hold a special place in my heart.

Reality is not destiny

– Eduardo Galeano

Table of Contents

List of Tables

List of Figures

Chapter 1

Introduction

The Standard Model (SM) of particle physics, proposed almost 50 years ago [1], remains our most successful description of Nature at the fundamental level. In 2012, one of the final great predictions of the SM, the Higgs boson, was finally observed at the LHC, nearly 40 years after the SM was initially created [2]. The announcement of the discovery of the Higgs boson was a watershed moment in particle physics. However, despite this last missing piece of the SM finally being experimentally confirmed, there are still many unresolved problems and phenomena which cannot be explained.

Outstanding questions such as the origins of matter, fermion flavors, mass, and dark matter cannot be answered by the SM. It is not difficult to realize that the SM is an incomplete description or particle physics. The primary contradiction within particle physics is that the SM is so obviously incomplete while also being able to predict particle interactions with incredible precision. However, the predictive power of the SM can also be our window into physics beyond the SM (BSM). Measuring small deviations from the SM prediction may provide some hint of new physics within our experimental reach [3]. The Higgs boson, by virtue of being the newest particle is also the least studied. Therefore, precision measurements of the properties of the Higgs boson may help us answer some of the biggest questions in physics.

1.1 The Standard Model

The SM of particle physics characterizes the interactions of elementary particles. An elementary particle is any particle that is not composed of smaller constituent particles. Currently there are 17 known elementary particles. These particles can be categorized as either fermions or bosons. Fermions have $\frac{1}{2}$-integer spin and obey the Pauli exclusion principle, whereas bosons have integer spin (0 or 1 in the SM) and do not obey the Pauli exclusion principle. Fermions constitute all visible matter in the universe and bosons mediate the interactions between them.

There are currently three fundamental forces described by the SM, known as the electromagnetic, weak and strong forces. Although gravity is a fundamental force of nature, a quantized theory of gravity has not been completed yet and therefore it is not included in the SM. The force carrier of the electromagnetic force, the photon γ, mediates interactions between all particles that have an electromagnetic charge. All particles that have an electroweak iso-spin are affected by the weak force, with force carriers Z, W^+, W^-. The strong force is mediated by gluons g which interact with all particles that have a color-charge. The 12 fermions can be split into two equal-sized families of particles known as quarks and leptons. Quarks have an electromagnetic charge of $\pm\frac{1}{3}e$ or $\pm\frac{2}{3}e$ and carry an additional color-charge, either red,blue, or green. Leptons are colorless particles which can be charge-less or have electromagnetic charge e. The charge-less leptons are called neutrinos, and since they are both charge-less and color-less, they only interact through the weak force. A diagram illustrating the fundamental particle interactions in the SM is shown in Fig. 1.1

1.2 Symmetries and Conservation Laws

The SM is a relativistic quantum field theory with the underlying gauge-symmetry, $SU(3) \times SU(2) \times U(1)$. In general, a quantum field theory does not have to have any underlying symmetry. However, without underlying symmetries, solutions may become unstable and lead to non-physical results. Noether's theorem describes an interesting consequence of underlying symmetries in field theories. Noether's theorem states that every continuous global symmetry of the action leads to a conserved current and thus a conserved charge for solutions of the equations of motion. The inverse of this theorem also implies a conserved charge indicates that there is some underlying symmetry [4].

Experimental observations which hinted at underlying conservation laws were instrumental in the construction of the SM. In the following sections I will show how the SM can be constructed by enforcing gauge symmetries on the free particle Lagrangian. I will also show the consequences of spontaneous symmetry breaking and how the Higgs mechanism generates massive fermions and vector bosons.

1.2.1 Quantum Electrodynamics

Quantum Electrodynamics is a field theory that describes the interaction of charged particles with the electromagnetic field. The free field Lagrangian for fermions, is given as

$$\mathcal{L} = \bar{\psi}(i\gamma^{\mu}\partial_{\mu} - m)\psi \tag{1.1}$$

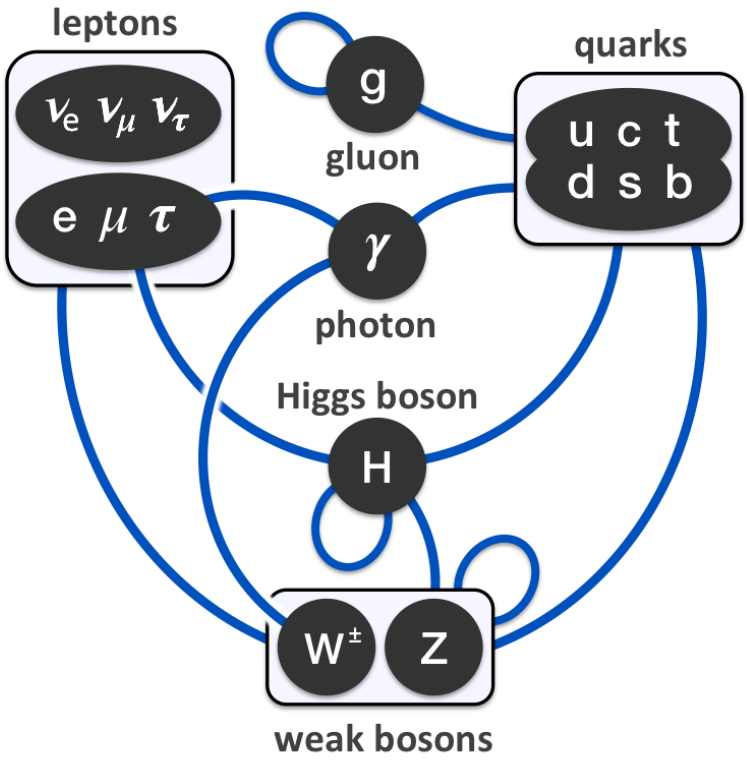

Figure 1.1: Graph-diagram representing all elementary particles and their interactions. A solid line connecting one particle to another denotes a possible interaction. A loop indicates that a particle can interact with itself or other particles of the same type. [5]

where ψ is the charged fermion field, γ^μ are the Dirac matrices, and m is the fermion mass. It is clear that this Lagrangian is invariant under the field transformation $\psi \to e^{i\theta}\psi$. This global symmetry is described by the group $U(1)$, corresponding to a shift in the phase of the fermion field. The global $U(1)$ symmetry also implies that our theory is locally invariant under $U(1)$. Enforcing this constraint, the field transformation becomes $\psi \to e^{i\theta(x)}\psi$ where $\theta(x)$ is now a space-time dependent phase. Maintaining the local symmetry requires that the derivative ∂_μ be replaced with the covariant derivative $D_\mu = \partial_\mu - iqA_\mu$ where q is some constant and A_μ is a field that transforms as $A_\mu \to A_\mu + \partial\theta(x)$.

Expanding the covariant derivative in Eq. (1.1), we are left with the Lagrangian,

$$\mathcal{L} = \bar{\psi}(i\gamma^\mu\partial_\mu - m)\psi - q\bar{\psi}\gamma^\mu\psi A_\mu \tag{1.2}$$

This Lagrangian now includes an interaction term between the fermions and the gauge field A_μ. However, it is still unclear exactly what the meaning of A_μ is. Naturally, one might expect that since the particles are charged, this new field A_μ may be related to the electromagnetic field in some way. The free field Lagrangian of the electromagnetic field is

$$\mathcal{L}_{EM} = \frac{1}{4}F_{\mu\nu}F^{\mu\nu} \tag{1.3}$$

where $F_{\mu\nu} = \partial_\mu A_\nu - \partial_\nu A_\mu$ is the field strength tensor of the electromagnetic field. This Lagrangian also obeys $U(1)$ symmetry. Therefore, one might identify that the gauge

field A_μ introduced by localizing $U(1)$ symmetry in Eq.(1.2) is the electromagnetic field and q is the charge of the fermions. Combining Eq. (1.2) and Eq. (1.3), we are then left with the SM QED Lagrangian describing charged fermion interactions:

$$\mathcal{L}_{QED} = \bar{\psi}(i\gamma^\mu D_\mu - m)\psi + \frac{1}{4}F_{\mu\nu}F^{\mu\nu} \tag{1.4}$$

Apllying Noether's theorem to this Lagrangian we find a conserved current $j^\mu = -q\bar{\psi}\gamma^\mu\psi$. The global $U(1)$ symmetry led to the conservation of the charged fermion current.

1.2.2 Electroweak Theory

In the previous section, we arrived at the SM QED Lagrangian by enforcing a local symmetry of an already known free field Lagrangian. However, in some cases, experimental data informs the construction of a new Lagrangian. In 1957, Cobalt-60 experiments performed by Wu revealed the first evidence of parity violation [6]. One of the most shocking consequences of parity violation is that chirality is a fundamental property of nature. In order to explain these experimental observations a new theory must differentiate between left and right handed fermions. Under the assumption that there are no right handed neutrinos, the left and right handed fermions can be grouped into doublet and singlet states respectively [7][8][9]. For left handed fermions we have separate doublets for lepton and neutrino states given as:

$$\psi_L = \begin{pmatrix} \nu_L \\ \\ l_L \end{pmatrix}, \begin{pmatrix} u_L \\ \\ d_L \end{pmatrix} \tag{1.5}$$

and the singlet states for right-handed leptons are given as

$$\psi_R = l_R, u_R, d_R \tag{1.6}$$

The free particle Lagrangian including left and right handed fermions is then

$$\mathcal{L} = i\bar{\psi}_L \gamma^\mu \partial_\mu \psi_L - i\bar{\psi}_R \gamma^\mu \partial_\mu \psi_R - m(\bar{\psi}_R \psi_L + \bar{\psi}_L \psi_R) \tag{1.7}$$

ψ_L are complex doublets and should be symmetric under $SU(2)$. The singlet states must also be symmetric under $U(1)$. Localizing this symmetry, it follows that the left-handed and right-handed fermion fields transform as

$$\psi_L \to e^{i\alpha \cdot T + i\beta Y_L} \psi_L \tag{1.8}$$

$$\psi_R \to e^{i\beta Y_L} \psi_R \tag{1.9}$$

In order for the Lagrangian to be locally invariant under these transformations, the derivative must be replaced with the covariant derivatives

$$D_L = \partial^\mu + igW^{i,\mu}T^i + i\frac{g'}{2}Y_L B^\mu \tag{1.10}$$

$$D_R = \partial^\mu + i\frac{g'}{2}B^\mu \tag{1.11}$$

where T^i are the generators of $SU(2)$ i.e the Pauli matrices σ_i, and constants g and g' are the weak isospin and weak hyperchange couplings. The three generators of $SU(2)$ and the single generator of $U(1)$ leaves us with 3 x 1 new gauge fields $((W^1, W^2, W^3) \times B)$mediating the interactions of the left and right handed fermions. The free field Lagrangian for these new fields is then

$$\mathcal{L}_{B,W} = -\frac{1}{4}B_{\mu\nu}B^{\mu\nu} - \sum_i \frac{1}{4}W_{i,\mu\nu}W^{i,\mu\nu} \tag{1.12}$$

where $W^i_{\mu\nu} = \partial_\mu W^i_\nu - \partial_\nu W^i_\mu - g\epsilon^{ijk}W^j_\mu W^k_\nu$ and $B^{\mu\nu} = \partial_\mu B_\nu - \partial_\nu B_\mu$ are the field strength tensors for the new gauge fields. The physical states $(Z, W^\pm, A)$ of the electroweak gauge bosons are formed as a mixture of the guage eigenstates.

$$W^\pm = \frac{W^1_\mu \mp iW^2_\mu}{\sqrt{2}} \tag{1.13}$$

$$Z_\mu = W^3_\mu \cos\theta_W - B_\mu \sin\theta_W \tag{1.14}$$

$$A_\mu = W^3_\mu \sin\theta_W + B_\mu \cos\theta_W \tag{1.15}$$

where θ_W is the Weinberg angle with $\cos\theta_W = \frac{g}{\sqrt{g^2+g'^2}}$. We are also now left with two

new conserved currents, fermion isospin and hypercharge. In the Electroweak sector all interactions must conserve T_3 and Y_L, which are the z-component of the isospin and the weak hypercharge respectively. However, plugging the covariant derivative definitions into Eq. (1.7) leaves a few glaring issues. Introducing masses to any of the physical fields in the resulting Lagrangian will break the gauge invariance. However, the short range of the weak force indicates that the force carriers should be massive. The theory for weak interactions under $SU(2) \times U(1)$ is not compatible with the theory for quantum electrodynamics $U(1)$ which is gauge invariant for massive fermions. Another issue with this theory is that even with some ad hoc inclusion of the weak boson masses it has been shown that the $W^+W^- \to W^+W^-$ scattering process violates unitary at high energies. These theoretical issues can be addressed through the Higgs mechanism described in section 1.3, which provides an explanation for the generation of masses for the weak bosons and fermions and prevents weak theory from breaking at high energies.

1.2.3 Quantum Chromodynamics

The final piece of the SM, quantum chromodynamics, or QCD, describes the interactions of quarks and gluons via the strong force. Early developments in the formulation for the strong force started in the early 60s with the development of the quark model as a way to describe the "zoo" of new particles being discovered in collider experiments. Gel-mans organizations of mesons and baryons according to strangeness and charge, looked like the group representation of SU(3), hinting at some underlying symmetry in the hadron sector [10]. Gell-man posited that this was due to an underlying flavor symmetry of three different particles with fractional charge and $\frac{1}{2}$-integer spin. These

particles, called quarks, were the fundamental particles that made up the sea of hadrons. The Δ^{++} baryon [11] provided a hint that the underlying SU(3) flavor symmetry was only approximate since in the flavor eigenstate basis the Δ^{++} wavefunction could not be constructed in an anti-symmetric way, violating the Pauli exclusion principle. It was later theorized that the underlying symmetry was $SU(3)_C$ where C corresponds to the "color charge" red, blue, or green [12]. Experimental evidence from deep inelastic scattering experiments at SLAC in 1969 showed the first direct evidence that the proton contained three particles [13]. Experimental results also showed that these particles were not rigidly constrained inside the proton, instead behaving as free particles. For this reason they were named partons instead of quarks. It was only after the discovery of asymptotic freedom in QCD, which explains why quarks are confined at low energies and behave as free particles at high energy [14], that the quark theory and color charge were integrated into the SM.

The derivation of the SM QCD Lagrangian closely follows that of the QED Lagrangian in Eq. (1.2.1). The free quark Lagrangian takes the form

$$\mathcal{L} = \bar{q_f^c}(i\gamma^\mu \partial_\mu - m)q_f^c \tag{1.16}$$

where c is the color index and f is the quark flavor. Enforcing a local SU(3) symmetry requires the covariant derivative to be defined as

$$D_\mu = \partial_\mu + ig_s T^a G_\mu^a \tag{1.17}$$

where g_s is the strong coupling constant, $T^a = \frac{\lambda^a}{2}$ are the generators of $SU(3)$ G^a_μ is the corresponding gauge field. Applying this redefinition of the derivative to Eq. (1.16) and including the free gluon theory we are left with the SM QCD Lagranginan

$$\mathcal{L} = \bar{q^c_f}(i\gamma^\mu D_\mu - m)q^c_f - \frac{1}{4}G^a_{\mu\nu}G^{a\mu\nu} \tag{1.18}$$

where $G^a_{\mu\nu} = \partial_\mu G^a_\nu - \partial_\nu G^a_\mu - g_s f_{abc} G^b_\mu G^c_\nu$. The structure of the field strength tensor results in tri-linear and quadratic self interactions of the gluon fields which are responsible for the asymptotic freedom of the theory at high energies. The strength of strong force is energy dependent with coupling strength $\alpha_s = \frac{g_s^2}{4\pi} \propto \frac{1}{log(q^2/\Lambda^2)}$, where q^2 is the energy scale of the process and Λ is a parameter $\approx 300\,\text{MeV}$ [15]. At low energies α_s becomes extremely large, leading to quark confinement in hadrons. As a consequence of the global $SU(3)_C$ symmetry of the QCD theory, color is a conserved current of the SM.

1.3 The SM Higgs Boson

1.3.1 Generation of Weak Gauge Boson Masses

The Higgs-Mechanism was developed and introduced in the late 1960's in order to address the contradictions between weak theory and QED, and explain the generation of gauge boson masses [16] [17]. The Higgs mechanism introduces a complex scalar field Φ, now called the Higgs field. This field can be expressed as an SU(2) doublet of the form

$$\Phi = \begin{pmatrix} \frac{\phi_1 + i\phi_2}{\sqrt{2}} \\ \\ \frac{\phi_3 + i\phi_4}{\sqrt{2}} \end{pmatrix} \tag{1.19}$$

the free field Lagrangian of this field is given by

$$\mathcal{L}_\Phi = (\partial_\mu \Phi)^\dagger (\partial^\mu \Phi) \tag{1.20}$$

and since the Φ field should also have $SU(2) \times U(1)$ symmetry, the derivatives must transform as in 1.10. In the Higgs mechanism the field also has a non-zero vacuum potential

$$V(\Phi) = \mu^2 |\Phi|^2 - \lambda^2 |\Phi|^4 \tag{1.21}$$

This potential is known as the Higgs potential (illustrated in Fig. 1.2)and describes the Higgs fields' self-interactions. When $\mu^2 < 1$ the ground state of $V(\Phi)$ becomes completely degenerate with minima at $|\Phi^2| = \frac{\mu^2}{2\lambda^2}$. This selection of a specific ground state is known as spontaneous symmetry breaking. Spontaneous symmetry breaking occurs when the ground state of a system does not respect the global symmetry of the Lagrangian. The typical convention is to choose $\phi^+ = 0$ and $\phi^0 = v$ where $v^2 = \frac{-\mu^2}{\lambda}$ is the vacuum expectation value. The ground state of the Higgs field is now

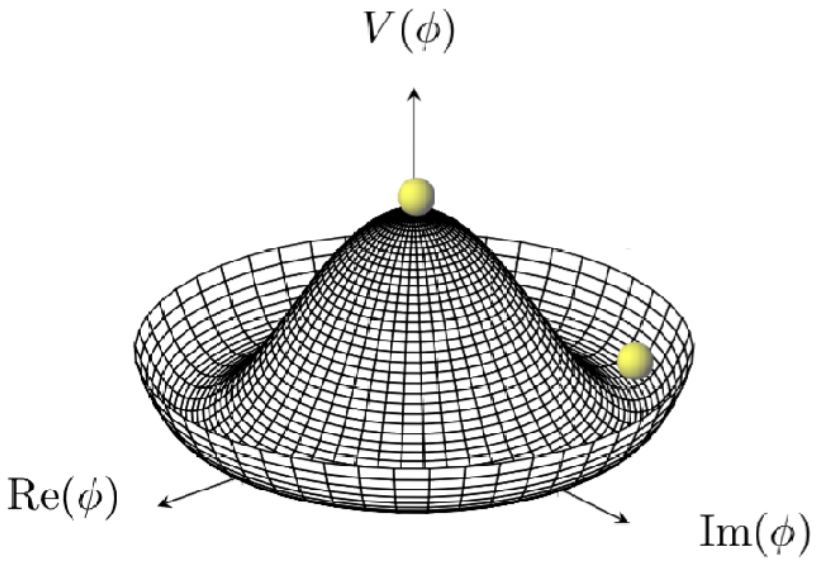

Figure 1.2: Diagram of the Higgs Potential. The golden balls represent the equilibrium points in the potential.

$$\Phi = \begin{pmatrix} 0 \\ \\ \frac{v}{\sqrt{2}} \end{pmatrix} \tag{1.22}$$

We now need to determine the unbroken symmetry group for the ground state of this system. First, we must find the generators Q of the unbroken symmetry. The generator of this group must be Hermitian and satisfy the relation $Q\Phi = 0$. We then find Q is of the form

$$Q = \begin{pmatrix} 1,0 & \\ & \\ 0,0 & \end{pmatrix} = T^3 + Y \tag{1.23}$$

showing that the symmetry has broken to $SU(2) \times U(1) \rightarrow U(1)_{EM}$ with electromagnetic charge Q. Goldstones theorem states that for a system with a global internal symmetry group G which is spontaneously broken down to a subgroup H there is a massless mode corresponding to each broken generator [18][19][20]. Therefore in going from four generators to one generator, we would expect 3 massless scalar Goldstone bosons to appear in the theory. However, since the Lagrangian in Eq. (1.20) is still globally symmetric under $SU(2) \times U(1)$, the Goldstone modes are not real particles and must acquire a mass through a gauge transformation called the unitary gauge. The remaining unbroken symmetry will have a corresponding massless gauge field.

Before deriving the masses of the vector bosons, we can derive the Higgs mass by perturbative expansion H around the ground state of the free theory in Eq. (1.20).

$$\Phi = \begin{pmatrix} 0 \\ \\ \frac{v+H}{\sqrt{2}} \end{pmatrix} \tag{1.24}$$

Inserting Eq. (1.24) into the Lagrangian in Eq. (1.20) and Eq. (1.21) we find

$$\mathcal{L}_\Phi = (\partial_\mu H)^\dagger(\partial^\mu H) - \lambda v^2 H^2 - \lambda v H^3 - \frac{\lambda}{4} H^4 \tag{1.25}$$

From this equation we see that the Lagrangian now has a mass-like term proportional to H^2. The corresponding Higgs mass is $M_H = \sqrt{2\lambda v}$. The masses of the weak bosons are generated from enforcing a local $SU(2) \times U(1)$ symmetry on the Higgs field. In the unitary gauge, the covariant derivative reduces to that of Eq. (1.10). We can then derive the masses of the vector bosons through a perturbative expansion of the Lagrangian and taking $H \to 0$ to remove the interaction terms which will not generate the mass.

$$\begin{aligned}\mathcal{L} = (D_\mu \Phi)^\dagger (D^\mu \Phi) &= |(\partial^\mu + igW^{i,\mu}T^i + i\frac{g'}{2}Y_L B^\mu) \begin{pmatrix} 0 \\ \\ \frac{v}{\sqrt{2}} \end{pmatrix}|^2 \\ &= \frac{v^2 g^2}{8}(W^1_\mu W^{1\mu} + W^2_\mu W^{2\mu}) + \frac{v^2}{2}(gW^3_\mu - g' B_\mu)^2 \end{aligned} \tag{1.26}$$

Redefining the fields according to Eq. (1.13) gives us the following terms grouped by (W^+, W^-, Z)

$$\frac{g^2 v^2}{8} W^+_\mu W^{\mu +} + \frac{g^2 v^2}{8} W^-_\mu W^{\mu -} + \frac{v^2(g^2 + g'^2)}{8} Z_\mu Z^\mu \tag{1.27}$$

with $M_{W^\pm} = \frac{gv}{2}$, $M_Z = \frac{v\sqrt{g^2+g'^2}}{2}$ and $M_A = 0$. Through the Higgs mechanism we are left with three massive weak bosons and one massless vector boson.

1.3.2 Generation of Fermion Masses

The final piece of electroweak theory is the generation of fermion masses. Analogously to the generation of the weak boson masses, fermion masses can be generated through interactions with the fermion and Higgs field. These interactions are described with the Yukawa Lagrangian

$$\mathcal{L}_Y = -Y^d_{ij}\bar{\psi^q_{Li}}\Phi d_{Rj} - Y^d_{ij}\bar{\psi^q_{Li}}\epsilon\Phi^* d_{Rj} - Y^l_{ij}\bar{\psi^l_{Li}}\Phi l_{Rj} \tag{1.28}$$

where $Y^{d,u,l}$ are 3×3 complex matrices corresponding to up-type quarks, down-type quarks, and leptons respectively, Φ is the complex scalar Higgs field, and i, j correspond to the 3 generations of quarks and leptons. ψ_L represents the left handed SU(2) doublets and d_R, u_R, l_R are the right handed singlets. Expanding around the ground state of the Higgs field $\Phi = (0, \frac{v+H}{\sqrt{2}})$ and taking $H \to 0$ we find mass terms proportional to

$$m_f = Y^{d,u,l}_{ij}\frac{v}{\sqrt{2}} \tag{1.29}$$

However, there is no reason for the matrices Y to be diagonal which implies a mixing of the flavor states in the weak eigenstate basis. However, in experiment we observe

flavor states with distinct masses, therefore to extract the physical masses of the fermions we must diagonalize Y. The matrices that diagonalize $Y^{u,d}$ give rise to the CKM matrix which governs transitions between quark flavors through interactions mediated by the W boson. The CKM matrix also allows for a complex-phase that results in CP-violation [21], one of the requirements for baryogenesis in the early universe [22]. Since Y^l is diagonal it implies that lepton mass eigenstates are also weak eigenstates, implying that lepton flavor is conserved in the SM. If right-handed neutrinos existed, then there would be equivalent mass terms proportional to $Y^{\nu}_{i,j}\frac{v}{\sqrt{2}}$ that would give the physical neutrino mass terms. Although in the SM, neutrinos are precisely massless, experiments at SNO lab have shown that neutrinos undergo flavor oscillations, indicating that they have mass [23]. There are multiple ways to extend the SM to generate neutrino masses. One way is to introduce sterile neutrinos, which are new particles that do not interact through the strong, weak, or electromagnetic force. After electroweak symmetry breaking, the neutrinos will acquire a mass term from the Yukawa interaction with the sterile neutrino, the Higgs boson and the left-handed fermions. One could also imagine that the neutrino mass is generated by new physics at a higher energy scale that is inaccessible at the LHC. In this case, by treating the SM as an approximation of the true high-energy theory, one can construct an effective Higgs-neutrino interaction term which will generate a neutrino mass after electroweak symmetry breaking. Either of these extensions to the SM result in interesting consequences, such as violation of lepton flavor and number conservation, and the generation of a Majorana mass term which implies that neutrinos are their own antiparticle [24]. The origin of neutrino masses and whether or not they are acquired through interactions with the Higgs field is still a mystery in the SM.

1.4 The Higgs as a portal to BSM physics

So far, at the LHC, the Higgs boson is the only new fundamental particle that has been discovered. This represents a sort of crisis in the field of particle physics. There was a hope that probing physics at the TeV scale would reveal new fundamental interactions or particles besides the Higgs boson. This was mainly motivated by potential solutions to the hierarchy problem. Under the assumption that the scale of new physics is at the scale of the Planck mass $M_p \sim 10^{19}$ GeV (the scale of quantum gravity), radiative corrections to the Higgs boson mass require enormous fine tuning to keep the physical Higgs boson mass at 125 GeV [25]. This fine tuning is considered unnatural since the scale of the corrections is much larger than the mass of the Higgs boson. Theories such as supersymmetry (SUSY) provided a way out from this unnaturalness. SUSY posited that there was an underlying symmetry between fermions and bosons, where each SM particle had its own supersymmetric particle with the exact same mass and quantum numbers besides spin. Above the SUSY breaking scale, the radiative corrections to the Higgs mass from the SM particles are exactly canceled by their supersymmetric partners [26]. Most importantly, SUSY provided predictions for new particles and interactions which could be experimentally verified at the LHC. However, after almost 15 years there has yet to be experimental evidence of SUSY and the phase space of allowed theories is getting smaller. In the absence of anything else, the Higgs boson may be our only window into physics beyond the SM before the next generation of colliders with $\sqrt{s}$ $\mathcal{O}(10$ TeV) comes online.

The SM is a very accurate description of nature. However, it is merely a useful mathematical description of what we observe and does little to answer "why" nature

is the way that it is. For example, while the Higgs mechanism can explain how fermions, and weak bosons acquire their mass, it provides no explanation for how or why electroweak symmetry breaking occurs in the first place and what sets the value of those masses.

The Higgs potential, a term in the Lagrangian attached by hand, also has profound effects on early universe cosmology. The Higgs potential has a non-zero vacuum expectation value and can be interpreted as a contribution to the vacuum energy density ρ_{vac}. In the SM the vacuum energy density is calculated to be $\rho_{vac} \sim 1.2 \times 10^8\,\mathrm{GeV}^4$ which is in direct contradiction to the observed energy density $V_{vac} \sim 10^{-10}$ eV^4 [27]. This vast difference in prediction and observation is known as the cosmological constant problem. In early universe cosmology the process in which the Higgs potential took its current shape is called the electroweak phase transition. This phase transition is expected to have taken place a nanosecond after the big bang. At some critical temperature $T_c \sim 160\,\mathrm{GeV}$ the phase transition occurs when the universe either falls from the unstable maximum at $H = 0$ and chooses a ground state as in Fig. 1.2 or tunnels from the local minima at $H = 0$ to the ground state at $|H| = v/\sqrt{2}$. These transitions, illustrated in Fig. 1.3 are referred to as first- and second-order phase transitions. The first-order phase transition would leave a signal in the gravitational wave background and is required to explain the observed matter-antimatter asymmetry, but the first-order phase transition is not possible without BSM physics [28]. By studying the Higgs boson and the shape of the potential, we might be able to learn more about the origins of electroweak symmetry breaking and underlying symmetries.

Although the Higgs mechanism provides an explanation for how vector bosons and

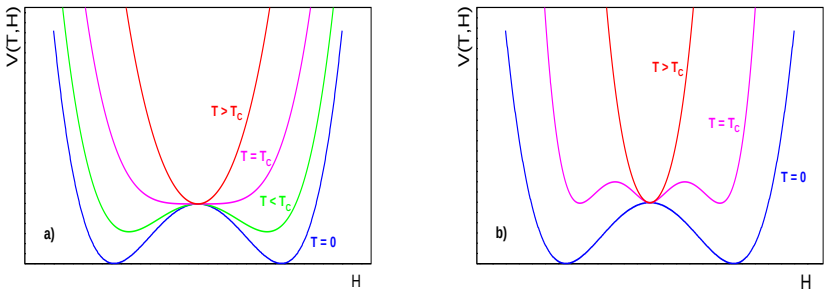

Figure 1.3: Higgs potential for several temperatures compared with the critical temperature T_c for a) second order phase transition. b) first order phase transition.

fermions acquire mass, the actual mass terms (15 in total) in the Lagrangian are completely unconstrained and must be measured experimentally. The strength of the Higgs Yukawa couplings are directly responsible for flavor mixing in the quark sector, and all known CP-violation. This implies that the Higgs boson is connected to fundamental questions of particle physics such as the origins of mass,flavor, and CP-violation [3]. Because the Higgs boson couples to all particles that have a mass, there may also be some link between the Higgs bosom sector and dark matter. This may be detected in the observation of invisible Higgs boson decays, or deviations from the SM prediction for the Higgs boson width. The Higgs boson can also provide clues to the nature of new physics at higher energy scales. Since the Higgs boson's couplings to other particles can be easily calculated, any measured deviations from the SM expectations must indicate some new heavy physics interfering with the SM process.

All of the reasons described in this section demonstrate that the Higgs boson may be viewed as our portal to BSM physics, due to its connection to many of the biggest questions in particle physics. Therefore, a program of precision measurements of the

Higgs boson properties may be the only way towards an understanding of new physics beyond the SM at the LHC.

Chapter 2
The CMS Experiment

2.1 Introduction

All of the experimental data in this thesis was collected from the Compact Muon Solenoid (CMS) experiment at the Large Hadron Collider(LHC), located at the European Organization for Nuclear Research (CERN) in Geneva Switzerland. The first discussions for a TeV scale hadron collider facility were being had as early as 1976, around the time that CERN decided to construct the Large Electron-Positron Collider; almost 35 years before the LHC would first come online. The director generals of CERN in 1977 recommended that the LEP tunnel should be constructed large enough to accommodate the ring of superconducting magnets required to accelerate protons over 3 TeV [29]. The first conference discussing the feasibility of such a facility occurred in 1984 in Lusanne [30]. A few years later in 1992, the CMS collaboration published its letter of intent for the construction of a general purpose detector at the LHC [31].

In the following sections, I will describe briefly the technical specifications of the LHC and CMS detector, as well as the performance of the detector subsystems. The LHC, and the multiple experiments it houses, is a marvel of human ingenuity and collaboration. I am one person among thousands of scientists, engineers, computer scientists, construction workers, etc. who have contributed to this experiment over the course of 50 years. Some of those people who started thinking about the LHC in

the late 1970s would not live long enough to see the first scientific results.

2.2 The Large Hadron Collider

In order to study the Higgs boson, particles have to be both accelerated to a large energy and collided at a fast rate in order to produce them. The Large Hadron Collider (LHC), located 100m underground near Geneva, Switzerland, accelerates and collides protons at center-of-mass energies of 13 (in Run2) or 13.6 TeV (in Run3) at four interaction points along a 27km circumference tunnel. Depending on the data taking era the protons start out as a hydrogen gas and are linearly accelerated to either 50 MeV (Run2) or 160 MeV (Run3). The protons are then injected into the Proton Synchrotron Booster (PSB), a small accelerator with 25m radius that accelerates the protons up to 2 GeV. Once the protons reach this energy, they are then injected into the Proton Synchrotron (PS) and after that, the Super Proton Synchrotron (SPS). Once the protons are accelerated to 450 GeV they are injected into the LHC. Once injected into the LHC, these proton bunches are accelerated by a series of 1232 superconducting dipole magnets up to 6.5-6.8 TeV while various quadrupole magnets focus and condense the bunches. During operation, there are two proton beams traveling in opposite directions, each consisting of roughly 2800 bunches of protons. The two beams are collided at four different interaction points along the LHC tunnel where the main experiments (ALICE, ATLAS, CMS, LHCb) are located. The rate of bunch crossings at the LHC is about 1 every 25 nanoseconds, with up to 60 proton-proton interactions per crossing. This corresponds to a collision rate on the order of a billion per second. The LHC produces roughy 200 petabytes of

data per year, which necessitated the construction of a distributed global computing infrastructure in order to accommodate this massive data flux.

2.3 The CMS Detector

The CMS detector was designed to be a general purpose particle detector. As such, it is capable of precise tracking and energy measurement of electrons, muons, photons, and hadrons, which are then used to reconstruct kinematic information about the inital short-lived states produced during the collision. The CMS detector is cylindrical in shape, consisting of concentric layers centered around the proton-proton interaction point. A cross-section of the CMS detector is shown in Fig. 2.1. The central feature of the CMS apparatus is a superconducting solenoid of 6m internal diameter, providing a magnetic field of 3.8T. Within the solenoid volume are a silicon pixel and strip tracker, a lead tungstate crystal electromagnetic calorimeter (ECAL), and a brass and scintillator hadron calorimeter (HCAL), each composed of a barrel and two endcap sections. Forward calorimeters extend the pseudorapidity (η) coverage provided by the barrel and endcap detectors. Muons are measured in gas-ionization detectors embedded in the steel flux-return yoke outside the solenoid. A more detailed description of the CMS detector, together with a definition of the coordinate system used and the relevant kinematic variables, can be found in Ref. [32, 33]

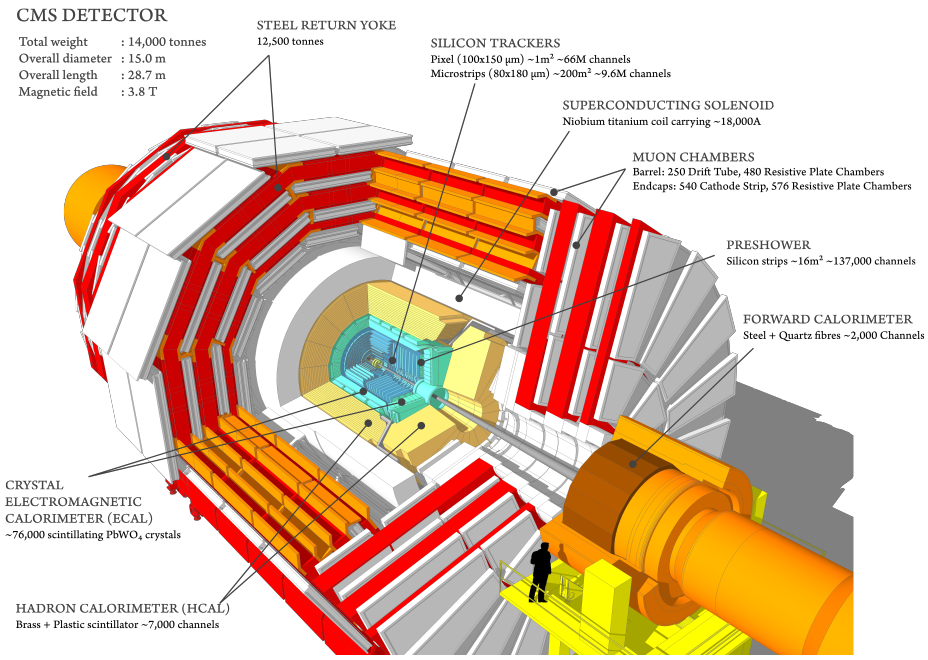

Figure 2.1: Diagram of the CMS detector showing various subsystems. Courtesy of the CMS collaboration [34].

2.4 Detector Subsystems

2.4.1 Silicon Tracker

The innermost subdetector of the CMS experiment constitutes the largest silicon tracker in the world, both in terms of the total surface area and the number of sensors. The mechanical structure of the silicon tracker consists of several high-level structures: two half barrels in the barrel pixel tracker (BPIX), four half cylinders in the two forward pixel tracker regions (FPIX), two half barrels in the strip tracker inner barrel (TIB) and in the strip tracker outer barrel (TOB), two endcaps in the tracker inner disks (TID) and in the tracker endcaps (TEC). For the Phase-0 (Phase-1) detector, the half barrels in the BPIX consist of three (four) layers and the half cylinders in the

FPIX consist of two (three) disks, separated in the plane parallel to the beam axis and perpendicular to the LHC plane. In the barrel, groups of eight pixel modules are mounted on rods arranged in cylindrical layers. The rods are mounted such that the modules of two adjacent ladders are rotated by 180 degrees around z with respect to each other, thus having the silicon surface pointing inwards or outwards. In the FPIX, modules are supported by blades arranged in a turbine-like geometry, each hosting two modules mounted back-to-back, pointing in opposite directions.

As charged particles travel through the silicon of the tracker, they interact with electrons in the crystal lattice. This interaction creates an electron-hole pair in the silicon medium. The electrons drift through the silicon and this signal is collected by the readout chip. The pixel modules provide the precise hit position in the plane of each sensor which allows for extremely precise vertexing and track reconstruction. During the 2009-2016 (2017 - 2026) LHC running periods, the silicon tracker consisted of 1440 (1856) silicon pixel and 15 148 silicon strip detector modules. After the 2016 data-taking period, the pixel detector was upgraded to its Phase-1 configuration. The upgraded pixel detector features one more layer in the barrel, and one more disk in each of the forward pixel endcaps, than the pixel detector that was in use up to the end of 2016 (Phase-0 pixel detector). This extended the acceptance of the tracker from a pseudorapidity range $|\eta| < 2.5$ to $|\eta| < 3.0$, and improved the impact parameter resolution. Before the Phase-1 upgrade, the track resolutions were typically 1.5% in transverse momentum (p_{T}) and 25–90 (45–150) µm in the transverse (longitudinal) impact parameter for nonisolated particles of $1 < p_{\mathrm{T}} < 10$ GeV and $|\eta| < 1.4$ [7]. For nonisolated particles of $1 < p_{\mathrm{T}} < 10$ GeV and $|\eta| < 3.0$, the track resolutions

are typically 1.5% in p_{T} and 20–75 µm in the transverse impact parameter for data recorded after the Phase-1 upgrade

2.4.2 Electromagnetic Calorimeter

The CMS electromagnetic calorimeter (ECAL) measures the energy of electrons and photons. The ECAL consists of a single layer of 82000 lead tungstate scintillators surrounding the silicon tracker. This material has a small radiation length of 0.89 cm and light decay time below 25ns making it ideal for the high radiation environment of the LHC. When a photon or an electron passes through the lead tungstate, the electron recoils off of heavy nuclei in the crystal. This recoil accelerates the electron, causing it to lose energy from bremsstrahlung radiation in the form of photons. Similarly, high energy photons will interact with the heavy nuclei to produce electron positron pairs. The electrons will radiate more photons which will then pair produce to form more electrons and so on. This cascade of particles is called an electromagnetic shower. The scintillated light emitted from this shower will travel through the crystal and be collected by photodetectors. A pre-shower detector is placed in front of the end-caps of the ECAL, which provides good enough spacial resolution to help distinguish between single high energy photons and two closely spaced low energy photons originating from the decay of a neutral pion [35].

2.4.3 Hadronic Calorimeter

The CMS hadronic calorimeter (HCAL) measures the energy and arrival time of hadrons. The HCAL is a sampling calorimeter composed of alternating layers of plastic scintillator and brass absorber layer. When a hadron passes through the

absorber material a cascade of particles called a hadronic shower is induced. Most of the energy from the shower is absorbed in the brass material. However, particles from this shower, passing through the scintillator, emit light which is detected by fiber optic wires connected to photomultipliers which amplify the signal. The amount of light detected is then used to estimate the energy of the incoming hadron [36].

2.4.4 Muon Tracker

The final layer of the CMS detector is the muon system. The entire muon system is located outside of the solenoid magnet coil. Four concentric "muon stations" separated by layers of steel called the "return yoke". These layers are needed to control the magnetic field outside of the 3.8T superconducting magnets. During operation they become saturated with a magnetic field of 2T with a magnetic field in the opposite direction of inside of the solenoid. Muons are the only particle that will not deposit all of its energy inside of the CMS detector. For this reason, the only way to measure muon energy is by measuring the curvature of the muon trajectory in the magnetic field. The muon system utilizes a variety of detector technologies including drift tubes (DTs), cathode strip detectors (CSCs), resistive plate chambers (RPCs) and gas electron multiplier chambers (GEMs). The RPCs and GEMs do not provide position and are used as a redundant system for triggering on muons in case of failure of the DT and CSC trigger system [37].

2.5 Trigger and Event Reconstruction

As described in Sec. 2.2, there are billions of collisions happening per second inside the CMS detector. Because of this extremely high interaction rate, it is impossible to record all record all event data from each beam crossing. However, not every event is actually worth saving. For example, most of the proton proton interactions are glancing blows with low total momentum transfer, which are unlikely to have created the heavy particles we wish to study.

Events of interest are selected using a two-tier trigger system. The first level, composed of custom hardware processors, uses information from the calorimeters and muon detectors to select events at a rate of around 100kHz within a fixed latency of about $4\,\mu$s [38]. The second level, known as the high-level trigger, consists of a farm of processors running a version of the full event reconstruction software optimized for fast processing, and reduces the event rate to around 1kHz before data storage [39, 40].

Full event reconstruction is performed with the particle flow algorithm. The particle-flow algorithm [41] aims to reconstruct and identify each individual particle in an event, with an optimized combination of information from the various elements of the CMS detector. The energy of photons is obtained from the ECAL measurement. The energy of electrons is determined from a combination of the electron momentum at the primary interaction vertex as determined by the tracker, the energy of the corresponding ECAL cluster, and the energy sum of all bremsstrahlung photons spatially compatible with originating from the electron track. The energy of muons is

obtained from the curvature of the corresponding track. The energy of charged hadrons is determined from a combination of their momentum measured in the tracker and the matching ECAL and HCAL energy deposits, corrected for the response function of the calorimeters to hadronic showers. Finally, the energy of neutral hadrons is obtained from the corresponding corrected ECAL and HCAL energies.

When a high energy quark or gluon is produced at the LHC, due to color confinement, they will immediately hadronize to form a color-neutral state. This process results in a narrow cone of particles called a "jet". Jets are clustered from particle-flow candidates using the anti-k_{T} algorithm [42, 43] with a distance parameter of either 0.4 (AK4 jets) or 0.8 (AK8 jets). The jet momentum is defined as the vector sum of all particle momenta in a jet and is found from simulation to be, on average, within 5–10% of the true momentum over the entire p_{T} spectrum and detector acceptance [44].

Chapter 3
Tracker Alignment

3.1 Introduction

In the CMS tracker, the precision of a single hit in a pixel module is typically on the order of a few microns. However, this precision by itself does not guarantee good track parameter resolution. In order to reconstruct particle tracks with enough precision for physics requirements, the positions and orientations of each module must also be known to a few micron precision. Tracker alignment, in its simplest description, is the process of inferring the position and orientation of each module in the tracker using particle tracks from a combination of collision data and cosmic rays.

In the track-based alignment approach, the alignment parameters $\mathbf{p}$ are derived by minimizing the following χ^2 function:

$$\chi^2(\mathbf{p},\mathbf{q}) = \sum_{j}^{\text{tracks}} \sum_{i}^{\text{hits}} \left(\frac{m_{ij} - f_{ij}(\mathbf{p},\mathbf{q}_j)}{\sigma_{ij}^{\text{m}}} \right)^2, \tag{3.1}$$

where

- $\mathbf{p}$ represents the alignment parameters (also called alignables), which refer to the hierarchical components of the tracking system whose positions and orientations can be corrected during the alignment process

- $\mathbf{q}$ represents the track parameters (signed radius of curvature,the angles of the

trajectory and impact parameter transverse to (and along) the beamline and the deflection by multiple scattering [45]),

- m is the measured hit position, f is the interpolated impact point position of a track, and

- σ^{m} represents the uncertainty in the measurements (local hit resolution, alignment uncertainty).

The number of alignables varies depending on the desired granularity of the alignment. For an alignment of the large mechanical structures in the pixel tracker, six parameters for the position and orientation of each of the structures would typically be used, leading to 36 parameters in total. In contrast, the alignment of every single module of the whole tracker, including eight or nine parameters per module describing corrections to the position, orientation, and surface deformations, would require several hundreds of thousands of alignment parameters.

During operation of the detector, changes in running conditions, such as changes of the magnetic field or changes in temperature, are sometimes unavoidable. As a result, the alignment must be constantly updated and evaluated for performance both during and after data taking periods. This change is reflected with a new set of alignment constants that is updated for different data taking periods. In the following section, I will describe the CMS tracker alignment procedure, and validations of the alignment performance in Run2 of the LHC.

3.2 HipPy Alignment Algorithm

The HipPy algorithm is based on the hits-and-impact-points algorithm [46, 47] with additional features introduced using the constraints developed for the BaBar track-based alignment [48]. It has been used extensively during commissioning of the CMS tracker [49] and during the CMS start-up period in Run 1 [50, 51]. Further improvements were introduced during Run 2, and the improved algorithm is now named hits-and-impact-points-past-year-1 (HipPy). The most important technical improvements in the HipPy alignment fit algorithm are:

1. The inclusion of alignment parameters beyond the three position and three orientation coordinates of each sensor, namely the curvature of the sensors.

2. The possibility to apply a weight to certain types of input to balance statistical and systematic uncertainties.

3. The option to perform sequential, hierarchical alignment over multiple time periods, when the time stability of the structures differs among the hierarchical levels.

4. The inclusion of possible mass and/or vertex constraints in certain types of events with known physics process.

The main distinguishing feature of the HipPy algorithm, compared with MillePede-II, is its local nature. The position and orientation of each sensor are determined independently of the other sensors. This approach has advantages and disadvantages compared to MillePede-II. One disadvantage is that multiple iterations of running

the algorithm are required to solve correlations between the sensor parameters. The number of iterations can be several dozen up to a hundred. This means multiple runs of the CPU-expensive track fits are needed, which limits the practical application of this algorithm. Advantages include the native integration with CMS software, immediately providing features such as the CMS Kalman filter code for track propagation without additional development. As a result, any constraint, such as mass or vertex constraints, implemented in the CMS software can be incorporated in the algorithm. Each iteration of the algorithm is a very simple application of a small matrix inversion. This simplicity and dependence on the CMS software makes the HipPy algorithm complementary to MillePede-II.

The diagram in Fig. 3.1 shows the design of the HipPy algorithm with the sequence for the event, track, and hit selection, including the application of the weight factors and constraints. The arrows indicate the flow of information and the dashed arrows indicate features that are not used in this work. The track data are categorized in several paths (vertical arrows pointing down) and the corresponding constraints are applied in each event during the track fit with a given set of alignment conditions (indicated by the red box). During the minimization procedure, different weights are assigned to different types of input, and a new set of alignment conditions is passed back to the track fitting procedure (vertical arrow pointing up). The process is repeated until convergence is reached. The inclusion of the laser calibration data [49, 50] was developed during Run 1 but the laser system was not supported anymore in Run 2. The optical survey data constraint was used during the Run 1 start-up [50] and was used as a constraint to a prior geometry during the Run 2 start-up. The main

new features of the HIPPY algorithm discussed above are indicated in the diagram. These are the multi-IOV reconstructed track data, the sensor surface deformation database object in addition to the sensor position, the division of input track data into categories with the corresponding constraints, and the application of weights to certain types of input in the minimization process. Further details can be found in the description of Fig. 10 in Ref. [48].

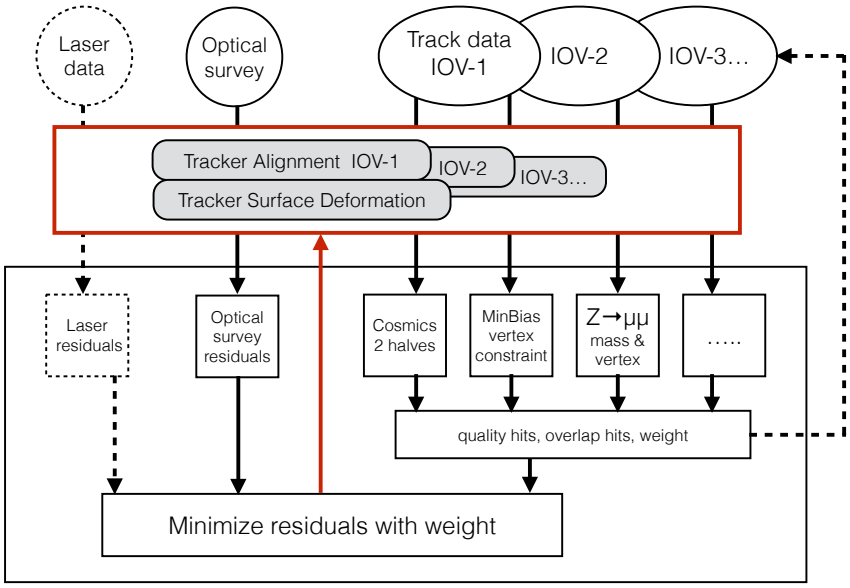

Figure 3.1: Diagram of the HIPPY algorithm design with the sequence for event, track, and hit selection, including application of the weight factors and constraints. Not all features were used in the Run 2 alignment procedure, as described in the text. The algorithm operates in iterative mode, indicated with the arrows.

3.3 Systematic misalignments

Systematic shifts of the assumed positions of the silicon modules of the tracker, when compared with the actual positions of the active elements, can occur. Such shifts will be called systematic distortions, or misalignments, of the tracker geometry. These

systematic misalignments may cause biases in the track reconstruction and this can have a negative impact on physics measurements. Therefore, a dedicated program of studies of such systematic distortions was developed. Weak Modes (WM) are a class of these systematic distortions. These are transformations that change a set of valid tracks into another set of valid tracks and satisfy $\Delta\chi^2 \approx 0$. They may arise when the alignment parameters of all modules are free in the alignment fit without additional constraints. Although such a transformation does not affect the individual track parameter fit performance in the alignment procedure, it may affect certain topologies of the tracks or correlations between tracks that are later used in physics measurements.

The most obvious example of a WM is a global movement of the whole detector, but more subtle effects are possible. The fact that all collision tracks come from the centre of the detector and that the detector is symmetric around the beam axis may cause certain WM biases that leave the χ^2 of the individual collision tracks invariant. Such a systematic distortion is not necessarily a WM, but the effect may be especially large in the direction with the weakest constraints.

In this section, we first present the methods used to detect the presence of systematic distortions in the alignment constants, then we review nine canonical systematic distortions. At this stage, only pure systematic distortions are discussed, without considering any alignment procedures.

3.3.1 Validation of systematic distortions

Several validations are used to check the effect of misalignments and determine whether a particular set of alignment constants performs well. A validation is essentially a measurement of a variable of interest that is also a metric for the alignment performance. The quantities we choose to study typically have a known value under perfectly aligned conditions. For example, a distribution of residuals is expected to peak at 0 with a given width. The difference in parameters between two halves of a cosmic ray track is also expected to be 0 on average. The mass of a reconstructed Z boson should be around 91.2 GeV. By detecting deviations from these expected values, especially deviations as functions of the track location or direction, we can search for biases.

3.3.1.1 Geometry comparison

Once the alignment fit has been performed, the new geometry is compared with a reference geometry, such as the design geometry or a previously aligned geometry. Systematic differences in such a comparison may reveal distortions in the tracker geometry. Although it is not possible to assess the validity of systematic shifts in the module positions from geometry comparisons alone, they may serve as a guide and visualization of possible effects in the tracker. Certain distortions may be known to be unphysical from the detector design constraints, and would form an early warning of biases in the alignment procedure prior to more detailed tests with the reconstructed track data. The geometry comparison validation was derived from the tools developed for the optical survey constraint within the HipPy algorithm discussed in Section 3.2. These tools match two geometries by translating and rotating certain structures before the differences between the geometries are calculated. These differences are treated

as survey residuals in the alignment algorithm [50]. The global shift and rotation of large structures are removed and the module displacements Δz, Δr, and $\Delta\phi$ are measured with respect to the reference geometry as a function of z, r, and ϕ. The other coordinates (x, y, and z) and three angular rotations can be visualized in this manner as well.

Geometry comparison validation is performed without any reconstructed track data and can be applied with reference to any prior geometry, such as design, survey, or previously aligned track-based geometry.

3.3.1.2 Cosmic ray muon track validation

The track parameter resolutions can be validated by independently reconstructing the upper and lower portions of cosmic ray muon tracks that cross the tracker and comparing the track parameters at the point of closest approach to the nominal beamline. We will refer to this procedure as the cosmic ray muon track split validation. This method is powerful because we know that the two halves of a given cosmic ray track should have the same parameters at the point closest to the nominal beamline, while each half of a track mimics a regular collision track originating from that point. Systematic differences between the track halves can indicate a misalignment.

Cosmic ray muon tracks and collision tracks have different topologies. Therefore, systematic distortions that may appear as WMs with collision tracks may be well constrained or visible with cosmics. In particular, the fact that these tracks do not originate at the centre of the detector means they connect the top and bottom halves of the detector directly through a single track. Such a connection is not possible

with tracks originating from the beam collision point. This effect is shown in Fig. 3.2. Since cosmic ray muons leave predominantly vertical tracks, they primarily constrain horizontal modules along the z-axis and have limited sensitivity for aligning vertical modules in the endcap regions or modules connecting different parts of the detector in the horizontal direction.

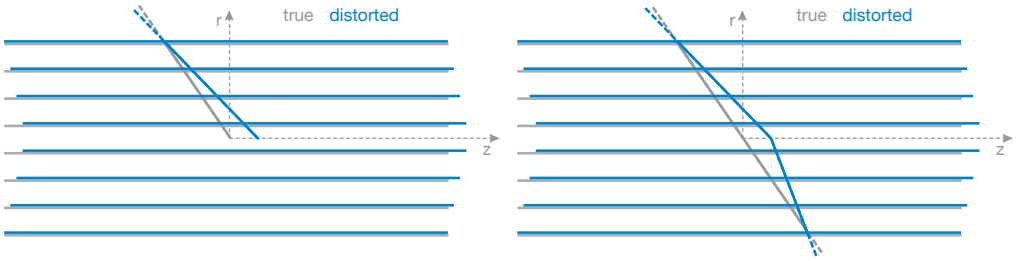

Figure 3.2: Diagram demonstrating distortions of the tracker geometry that may not affect the consistency of a reconstructed collision track with the measured hits (left), but introduce a kink when reconstructing the two halves of a cosmic ray muon track (right), leading to an inconsistency. This illustrates the telescope effect from Table 3.1.

Cosmic ray muon track validation can be performed without data from beam collisions and serves as an early validation of the detector geometry before LHC operation starts. It remains a powerful tool during collision data taking because of the unique topology of the cosmic ray muon tracks.

3.3.1.3 Overlap of hits within the same layer of modules

The overlap validation monitors the alignment by using hits from tracks passing through regions where modules overlap within a layer of the tracker. It can be performed either with the cosmic data or with data from beam collisions. Tracks are required to have two hits in separate modules within the same layer. In this method

we take advantage of the small distance between the two hits, and therefore the small uncertainty in the track parameter propagation between the two modules. The double difference in estimated and measured hit positions is very sensitive to systematic deformations. Unexpected deviations between the reconstructed hits and the predicted positions can indicate a misalignment. This is characterized by a nonzero mean of the difference of residuals. An illustration of the overlap measurements is shown in Fig. 3.3. The quantity of interest is the difference of residuals calculated as

$$(\text{hit}_A - \text{prediction}_A) - (\text{hit}_B - \text{prediction}_B), \tag{3.2}$$

where $\text{hit}_{A,B}$ refers to the position of a hit in module A or B, and $\text{prediction}_{A,B}$ refers to the position of a predicted impact point of the track in module A or B derived from its fit using measurements in other modules. The advantage of the overlap method is that most uncertainties in the track propagation are cancelled in the difference $(\text{prediction}_A - \text{prediction}_B)$. The difference of residuals is expected to be zero on average for a perfectly aligned detector. A positive shift in the mean is expected for expansion and a negative shift for contraction.

In Fig. 3.3, the overlap between modules A and B constrains the circumference of the detector, and therefore its radial scale, when measured for all pairs of modules. Figure 3.4 shows an example of the module overlaps in the ϕ and z directions for three representative modules in the first layer of the BPIX. The overlap between modules A and B constrains the circumference of the detector, as in Fig. 3.3. The overlap between modules A and C constrains the distance between modules in the z direction, and therefore the longitudinal scale.

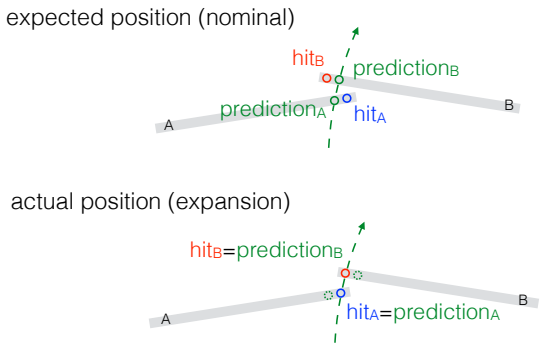

Figure 3.3: Diagram demonstrating the overlap regions of two representative modules A and B. In the upper diagram, the predicted track impact points (green circles) and the actual hits with charge depositions (red and blue circles) do not coincide because of a wrong prediction of the module positions. In the lower diagram, the actual module positions are shown for the geometry with radial expansion, and the predicted impact points and hits coincide. Uncertainties due to track propagation are ignored in this illustration, but are greatly reduced in the difference of residuals as discussed in the text. The green dashed circles in the lower diagram indicate predicted impact points from the nominal geometry in the upper diagram.

3.3.1.4 Dimuon validation

In an ideally aligned tracker, the reconstructed $X \to \mu\mu$ invariant mass should be minimally dependent on where in the detector the muons travel. Therefore, the quality of the set of alignment constants can be assessed by looking for biases in the reconstructed mass of a known resonance X. Any resonance can be used, but in practice we primarily consider Z boson decays into muons. This is because Z bosons are often produced with a relatively small boost, which results in the two muons passing through opposite ends of the tracker. Figure 3.5 shows an example of a systematic distortion to which $Z \to \mu\mu$ decays are very sensitive (twist distortion, described in Section 3.3.2).

Each selected event, with its reconstructed mass, is placed into a bin depending on the

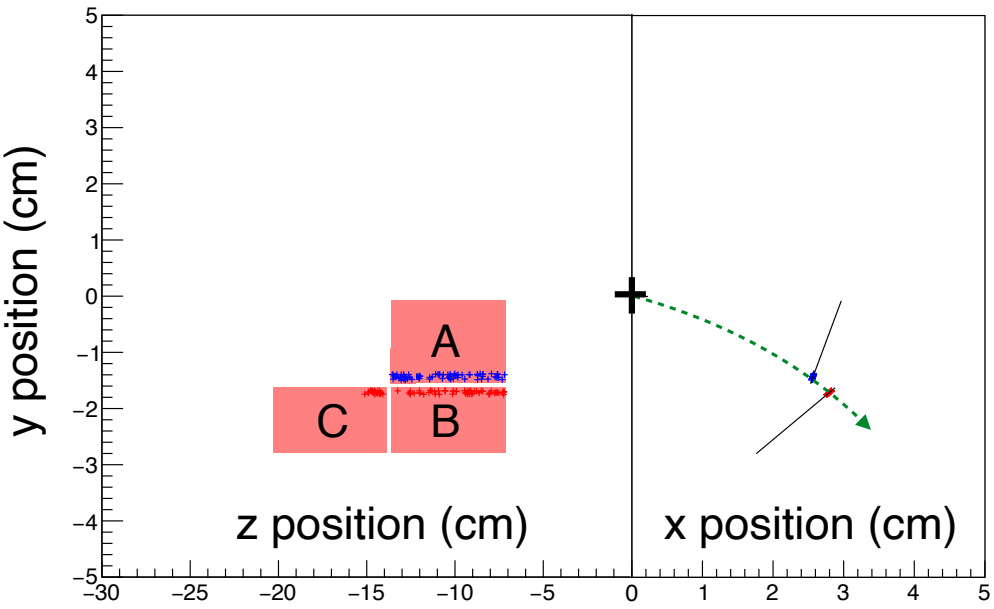

Figure 3.4: Diagram demonstrating the overlap regions of three representative modules A, B, and C in the first layer of the barrel pixel detector. The y-z view (left) and y-x view (right) are shown for the same modules. The overlap hits are indicated with the blue (inner) and red (outer) crosses and appear in tracks with hits in two consecutive modules in the same layer of the detector. The black cross represents the interaction point. The overlap between modules A and B constrains the distance between modules in the ϕ direction, whereas the overlap between modules A and C constrains the distance between modules in the z direction.

η and ϕ of the muons. The mass distribution of each bin is then fit with a Gaussian function, and the mean of this function is recorded as the reconstructed mass in that bin. The bins are then used to construct profiles of the invariant mass as a function of η or ϕ. Misalignment in the tracker may be detected if the mean reconstructed mass strays from the expected value of 91.2 GeV, either uniformly or as a function of η and ϕ.

Dimuon validation is performed with the LHC collision data after a sufficiently large

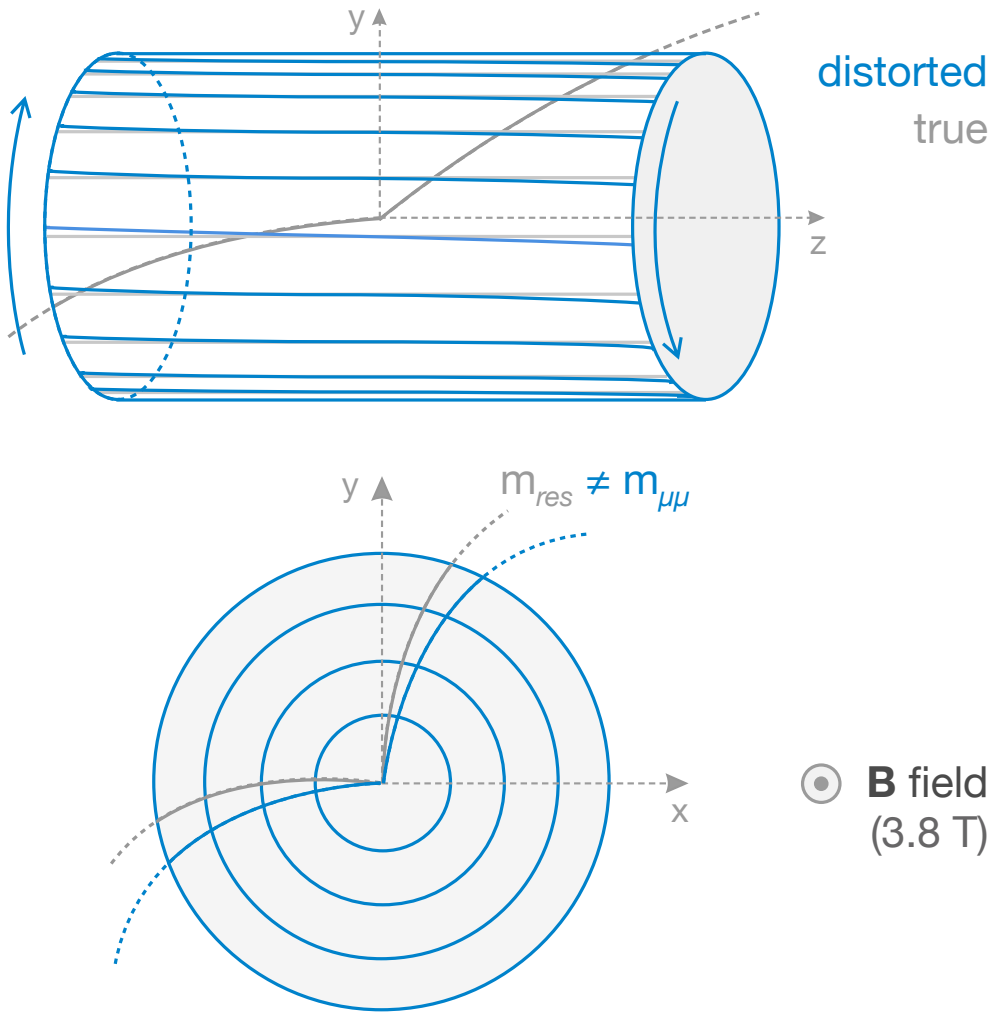

Figure 3.5: Diagrams demonstrating distortions of the tracker geometry in the r-z view (upper) and in the x-y view (lower) with the reconstructed muon pair from a $Z \to \mu\mu$ decay. The invariant mass of the pair of muons deviates from the expected value and becomes a function of the track parameters. This illustrates the twist effect from Table 3.1.

sample of $Z \to \mu\mu$ events has been accumulated. Therefore, this validation is powerful in stable operating conditions.

3.3.2 Modelling and validation of global systematic distortions

To study systematic distortions, and WMs in particular, we introduce nine first-order deformations natural for the cylindrical geometry of the CMS tracker and parameterize them with simple models described by a single parameter ϵ for each distortion. The systematic displacements from the reference geometry in Δz, Δr, and $\Delta\phi$ are functions of z, r, and ϕ, with an overall scaling given by ϵ. The functional forms used to generate each systematic misalignment are listed in Table 3.1.

Table 3.1: The nine basic systematic distortions in the cylindrical system, with the names of each systematic misalignment, the function by which the misalignment is generated, and a validation type sensitive to the misalignment. The parameter $z_0 = 271.846\,\text{cm}$ is half of the length of the CMS tracker, and ϕ_0 is an arbitrary constant phase.

	Δz	Δr	$\Delta\phi$
	z expansion	*bowing*	*twist*
vs. z	$\Delta z = \epsilon z$	$\Delta r = \epsilon r(z_0^2 - z^2)$	$\Delta\phi = \epsilon z$
	overlap	overlap	$\mathrm{Z} \to \mu\mu$
	telescope	*radial*	*layer rotation*
vs. r	$\Delta z = \epsilon r$	$\Delta r = \epsilon r$	$\Delta\phi = \epsilon r$
	cosmics	overlap	cosmics
	skew	*elliptical*	*sagitta*
vs. ϕ	$\Delta z = \epsilon\cos(\phi + \phi_0)$	$\Delta r = \epsilon r\cos(2\phi + 2\phi_0)$	$\Delta\phi = \epsilon\cos(\phi + \phi_0)$
	cosmics	cosmics	cosmics

The sign of ϵ is critical in the description of its value for misalignments. To save computing time, MC simulations are always performed using the ideal geometry, and the track reconstruction is performed with a possibly misaligned geometry. That is,

the detector position remains fixed to the ideal geometry, and the geometry used in the reconstruction changes. When discussing data, the opposite convention is more natural: the geometry used in the reconstruction is initially fixed and the detector itself moves. Taking the radial misalignment as an example, a value of $\epsilon > 0$ means that the geometry used for reconstruction is expanded in the r direction with respect to the geometry used during data taking. If this happens in data, we call it a radial contraction, because the detector has moved with respect to the expected position.

The nine basic systematic distortions summarized in Table 3.1 are not necessarily WMs when considering all possible topologies of tracks. We found that cosmic ray muon track, overlap, and dimuon validation are sufficient to detect these global, coherent movements of modules. This is illustrated in Fig. 3.6, where for each of the nine misalignments a representative validation using one of the three techniques is shown. In all cases, the five distributions are constructed using an MC simulation where the true positions of the modules are known. The distributions correspond to $\epsilon = 0$ (no misalignment) and two nonzero values of ϵ, both positive and negative. Where appropriate, the mean (μ) and root-mean-square (RMS) of the distributions are also given in the figure legends.

The uniform misalignment of the tracker in the z direction is known as z expansion (or contraction). In the BPIX, z expansion can be detected using overlapping sensors in the same layer. This validation is not possible with the silicon strip modules because there is no precise measurement of the z coordinate. We find that a change in ϵ causes a shift in the mean of the distributions for overlaps in the z direction. The design of the silicon pixel detector does not provide a z overlap for modules at the

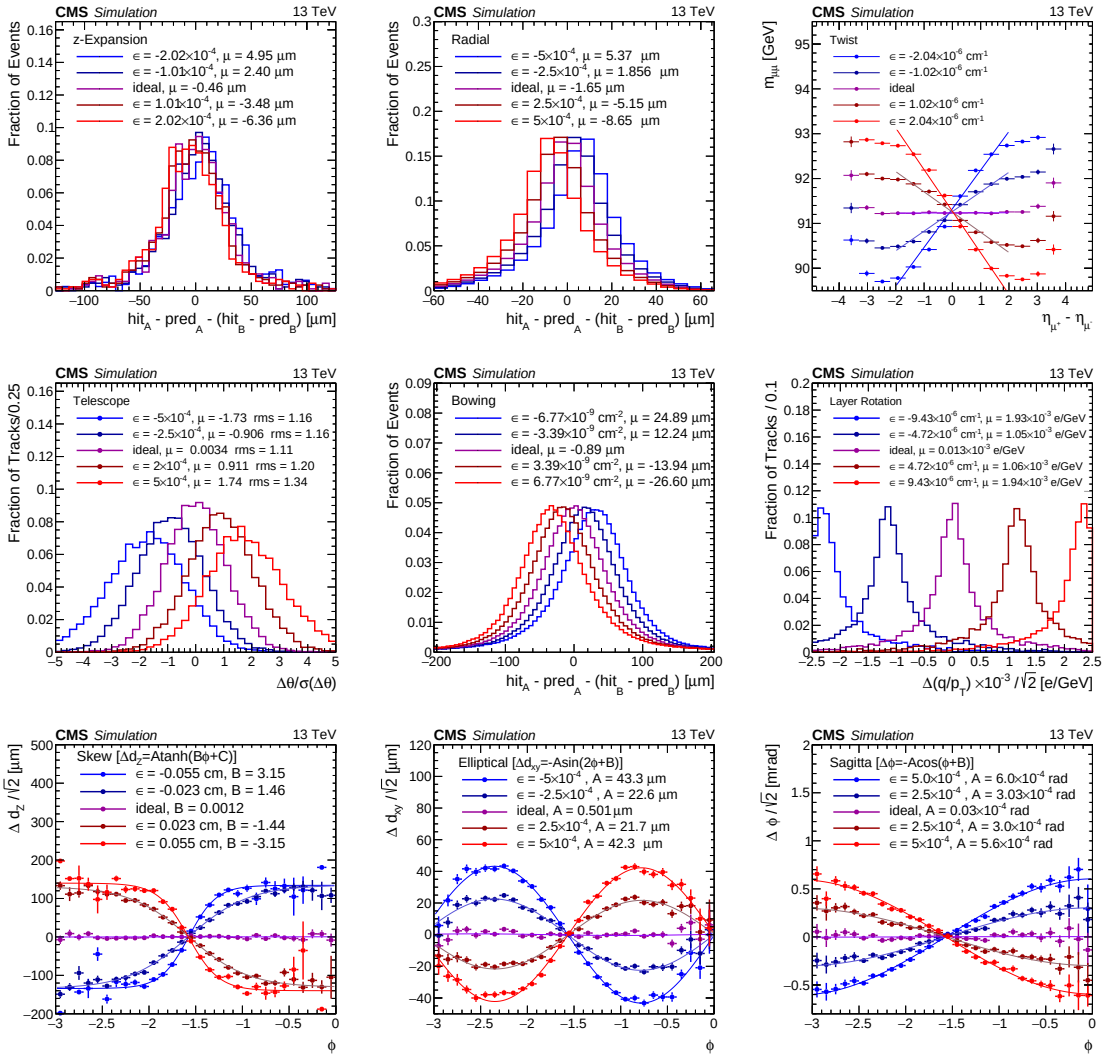

Figure 3.6: Validation of the nine basic systematic distortions summarized in Table 3.1 using reconstructed MC simulations with five variations of the misalignment parameter ϵ in each case. The ideal geometry in MC simulation corresponds to $\epsilon = 0$. The horizontal lines show the uncertainty on the average of a measurement in a given bin. The most sensitive validation out of cosmic ray muon track, overlap, or dimuon validation is employed in each case, as discussed in more detail in the text and as indicated in Table 3.1. In the bottom row, the formulae indicate the functional form of the fit used to extract the parameter quoted in the legend, which can be used to quantify the distortion. The convention for the sign of ϵ is discussed in the text and corresponds to a distortion in the geometry used for the reconstruction of MC events. This is opposite to the sign of the distortion if it were to be introduced in simulation of the detector components traversed by the charged particles.

same azimuthal angle, but it is possible for modules that are near in ϕ. Figure 3.6 (top row, left) shows the distribution of differences of residuals in the overlapping modules in the z direction with modules overlapping in the z direction in the BPIX for cosmic muon events in MC simulation. The z expansion misalignment is tested with $\epsilon = -2.02 \times 10^{-4}$, -1.01×10^{-4}, 0, 1.01×10^{-4}, and 2.02×10^{-4}. Constraining the z expansion in the strip detector is a more challenging task. For example, the global z position of the silicon modules in the endcap detectors is weakly constrained. Although the distribution of material has been studied extensively and is well described in Ref. [52], certain biases in the track reconstruction may appear if inactive material is not fully included in the detector model. This may lead to distortions in the detector geometry appearing in the form of a z expansion.

Radial expansion (or contraction) is the uniform misalignment of the tracker in the r direction as a function of r ($r \to r + \epsilon r$). Because of the uniform and symmetric nature of this misalignment, it is not easily detected with cosmic ray muon track splitting or $\mathrm{Z} \to \mu\mu$ decays. However, it is easily detected using the overlap validation, since in the case of a radial expansion, modules that overlap in the radial direction will move apart uniformly. Therefore, the difference between the true and the predicted hit locations in two overlapping modules is a good indicator of a radial expansion or contraction. The linear relationship between the mean of the overlap validation figures and the magnitude of the radial misalignment are used to categorize the presence of radial expansion or contraction in pp collision data. Figure 3.6 (top row, middle) shows the distribution of overlaps in the ϕ direction for modules overlapping in the ϕ direction in the BPIX for collision events in MC simulation. The MC events are

simulated with $\epsilon = 5 \times 10^{-4}$, 2.5×10^{-4}, 0, -2.5×10^{-4}, and -5×10^{-4}.

Twist is the misalignment of the tracker in the ϕ direction as a function of z. As such, twist shows up clearly in the $Z \to \mu\mu$ validation, and also in the overlap validation. The parameter used is the slope of the invariant mass $m_{\mu\mu}$ vs. $\Delta\eta_{\mu\mu}$ distribution. It ranges from $\Delta\eta_{\mu\mu} = -2$ to $+2$, as the distribution becomes nonlinear for larger values of $\Delta\eta_{\mu\mu}$. Figure 3.6 (top row, right) shows the profile of invariant mass $m_{\mu\mu}$ vs. $\Delta\eta_{\mu\mu}$ for $Z \to \mu\mu$ events in MC simulation. The MC events are simulated with $\epsilon = 2.04 \times 10^{-6}$, 1.02×10^{-6}, 0, -1.02×10^{-6}, and $-2.04 \times 10^{-6}\,\mathrm{cm}^{-1}$.

The telescope effect is the uniform misalignment of the tracker in the z direction as a function of r ($z \to z + \epsilon r$). This creates concentric rings that are offset in the z direction, and this misalignment can be visualized by imagining an actual telescope. Because of its z dependence, the telescope effect is identified primarily using the reconstruction of cosmic ray muon tracks. Figure 3.6 (middle row, left) shows the distribution of $\Delta\theta/\sigma(\Delta\theta)$ for cosmics in MC simulation. The MC events are simulated with $\epsilon = 5 \times 10^{-4}$, 2.5×10^{-4}, 0, -2.5×10^{-4}, and -5×10^{-4}.

Bowing is the misalignment of the tracker in the r direction as a function of z. It is similar to the radial expansion, and differs only by the fact that the bowing effect is a function of z. Figure 3.6 (middle row, middle) shows the distribution of overlaps in the ϕ direction with modules overlapping in the ϕ direction in the TOB for cosmic ray muon tracks in MC simulation. The MC events are simulated with the ideal detector geometry and reconstructed using five geometries, corresponding to the bowing misalignment with $\epsilon = 6.77 \times 10^{-9}$, 3.39×10^{-9}, 0, -3.39×10^{-9}, and

$-6.77 \times 10^{-9}\,\mathrm{cm}^{-2}$.

Layer rotation is the misalignment of the tracker in the ϕ direction as a function of r. The outer layers twist with a different magnitude to that of the inner layers. This distortion is easily picked up with cosmic ray muon track splitting, since we can see a change in track curvature between the two track halves. As such, we take the mean of a value proportional to the curvature for each value of ϵ. Figure 3.6 (middle row, right) shows the distribution of $\Delta(q/p_{\mathrm{T}})$ for cosmic events in MC simulation. The MC events are simulated with $\epsilon = 9.43 \times 10^{-6}$, 4.72×10^{-6}, 0, -4.72×10^{-6}, and $-9.43 \times 10^{-6}\,\mathrm{cm}^{-1}$.

Skew is the misalignment of the tracker in the z direction as a function of ϕ. Because of the ϕ dependency, it can be detected with cosmic ray muon track splitting. The distribution of Δd_z vs. ϕ can be fit with a hyperbolic tangent function, $A \times \tanh(B(\phi + C))$, from which we can extract ϵ. Figure 3.6 (bottom row, left) shows the profile of $\Delta d_z/\sqrt{2}$ vs. ϕ for cosmic events in MC simulation. The MC events are simulated with $\epsilon = 5.5 \times 10^{-2}$, 2.25×10^{-2}, 0, -2.25×10^{-2}, and $-5.5 \times 10^{-2}\,\mathrm{cm}$.

Elliptical distortion is the uniform misalignment of the tracker in the r direction as a function of ϕ ($r \to r + r\epsilon\cos(2\phi + \delta)$). Because of its ϕ dependency, elliptical distortion is easily detected with cosmic ray muon track splitting. This misalignment is especially clear in the modulation of the difference in the impact parameter Δd_{xy} as a function of the azimuthal angle of the track. We fit a sinusoidal function to this modulation, $\Delta d_{xy} = -A \times \sin(2\phi + B)$, and find a linear relationship between A and ϵ. Figure 3.6 (bottom row, middle) shows the profile of $\Delta d_{xy}/\sqrt{2}$ vs. ϕ for cosmic ray

muon events in MC simulation. The MC events are simulated with $\epsilon = 5 \times 10^{-4}$, 2.5×10^{-4}, 0, -2.5×10^{-4}, and -5×10^{-4}.

Sagitta distortion is the uniform misalignment of the tracker in the ϕ direction as a function of ϕ. As with the elliptical misalignment, the ϕ dependence in the sagitta distortion means it can be detected with cosmic ray muon track splitting validation. The effect of the misalignment can be seen in distributions of $\Delta\phi$ vs. ϕ. The distributions of $\Delta\phi$ vs. ϕ are fit with a cosine function, $\Delta\phi = -A\cos(\phi + B)$, from which we can extract ϵ. Figure 3.6 (bottom row, right) shows the distribution of $\Delta\phi$ vs. ϕ for cosmic events in MC simulation. The MC events are simulated with $\epsilon = 5 \times 10^{-4}$, 2.5×10^{-4}, 0, -2.5×10^{-4}, and -5×10^{-4}.

As the above studies show, various systematic distortions in the tracker geometry can be detected using combinations of different types of tracks and hits. Therefore, it is essential to combine all this information in the alignment procedure, which will be discussed in the next section. Balanced information in the input to the alignment procedure would ensure that such distortions are not present in the tracker geometry prepared for the reconstruction of tracks.

3.4 Trends in LHC Run2

3.4.1 Dimuon invariant mass reconstruction

The dimuon mass validation using $Z \to \mu\mu$ events was already discussed in Section 3.3. Beyond the improvement of the local precision, another improvement brought by the legacy reprocessing is related to the systematic distortions, as demonstrated in

Fig. 3.7. The sigmoid shape, typical of a twist distortion, is reduced in the legacy reprocessing when compared with the alignment during data taking and to the EOY reconstruction. Although the EOY reconstruction of the 2016 data did not suffer from such a distortion, that of the 2017 and 2018 data did suffer from it. For 2017, the distortion was improved by performing the alignment fit with MillePede-II in the legacy reprocessing. However, the distortion observed in 2018 was not removed by the same procedure and a twist transformation was applied in the opposite direction in addition to running MillePede-II for the legacy reprocessing. The reason for the need for extra processing in 2018 is not understood to date.

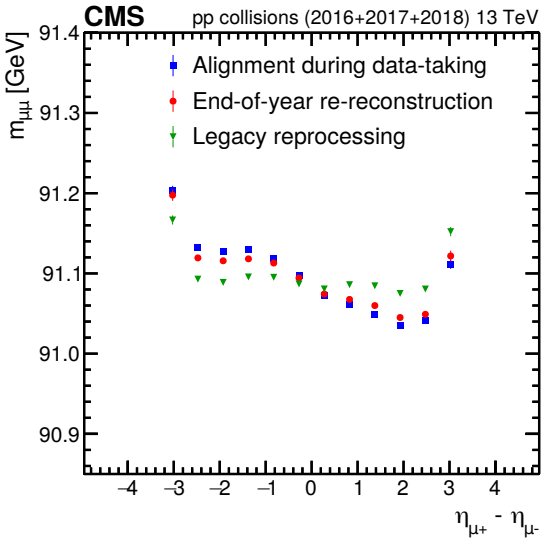

Figure 3.7: Reconstructed Z boson mass as a function of the difference in η between the positively and negatively charged muons, calculated from the full sample of dimuon events in the years 2016, 2017, and 2018. The error bars show the standard deviation of the invariant Z boson mass as retrieved from a fit of dimuon mass distribution to a Breit-Wigner convolved with a Crystal Ball function.

Further systematic distortions have been reduced with the legacy reprocessing. For instance, the bias in the reconstructed mass as a function of ϕ due to a systematic

distortion is periodic to first order, and the distributions are easily fit with a cosine function. As such, the amplitude of the fitted cosine function is a good measure for quantifying the magnitude of the bias in the reconstructed dimuon mass. The top figure of Fig. 3.8 demonstrates the periodicity of the reconstructed Z boson mass, whereas the bottom figure of Fig. 3.8 shows the amplitude of the reconstructed Z boson mass as a function of the delivered integrated luminosity. The amplitude shows the average spread of the reconstructed Z boson mass with respect to ϕ_{μ_+}, which is expected to be zero in a well-aligned detector. A nonzero amplitude indicates that the reconstructed mass has some dependence on the spatial coordinates of the detector. We observe an improvement in the legacy reprocessing compared with the earlier alignment procedures. However, the legacy reprocessing still shows a suboptimal performance in the 2018 data-taking year in comparison with the two other years. In addition to this, from the point of view of Fig. 3.8, the legacy reprocessing shows worse performance than the alignment during data taking, especially in the last 30 fb^{-1}. This is suspected to be related to the discrepancies between different IOVs with different configurations while operating the pixel detector, e.g. a change of voltage or annealing.

3.4.2 Cosmic ray muon track reconstruction

As was mentioned in Section 3.3, cosmic ray muon tracks are one of the key ingredients used to control systematic distortions in the alignment procedure. The quality of the alignment constants, and in particular the presence of certain systematic distortions, can also be better assessed by studying the performance of the reconstruction of cosmic ray muon tracks. Figure 3.9 shows $\Delta\eta$ and the difference in the impact parameter in the transverse plane between the two half tracks refitted from the hits of a cosmic ray

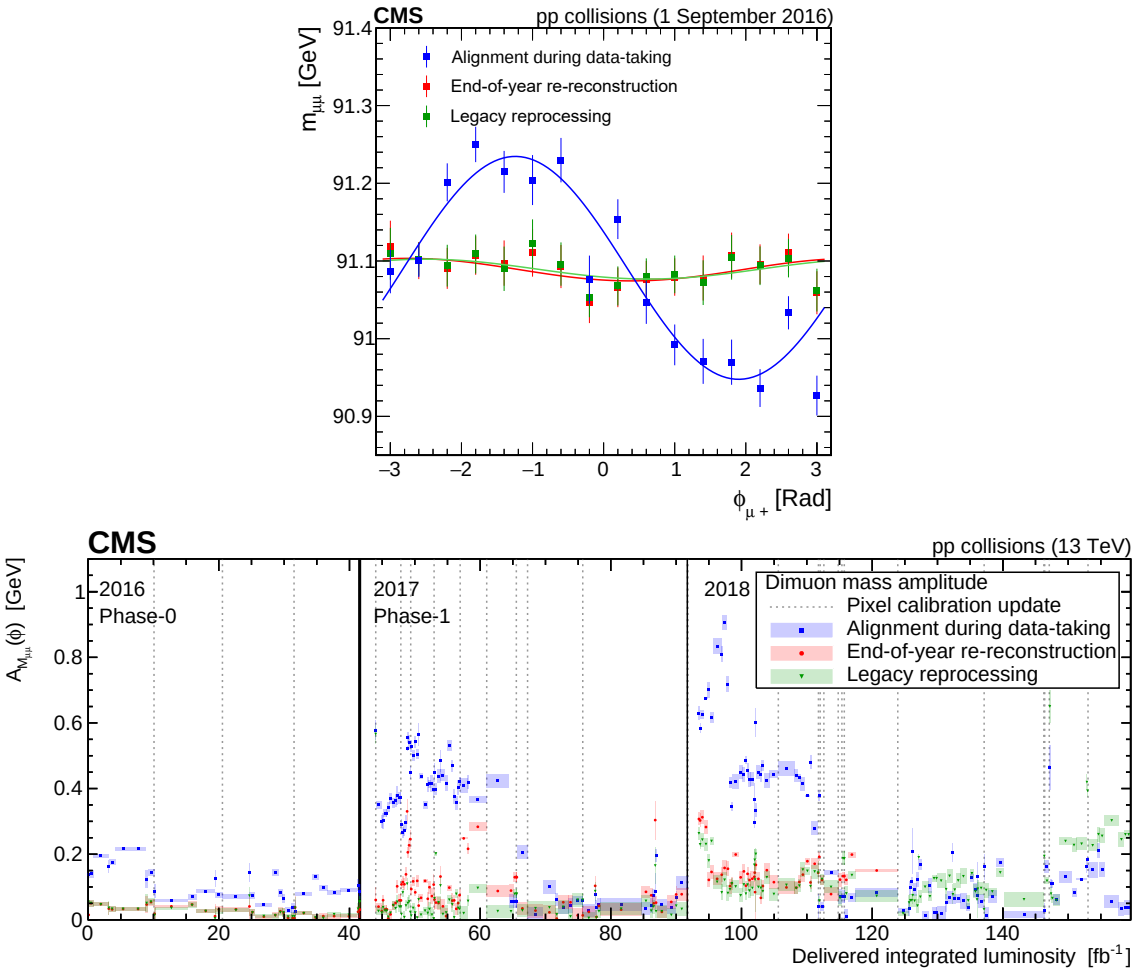

Figure 3.8: The upper figure shows the invariant mass of the dimuon system, as a function of the azimuthal angle of the positively charged track for a single IOV. The lower figure shows the amplitude A, obtained by fitting the invariant mass of the dimuon system versus ϕ_{μ_+} with a function of the form $A\cos(\phi + \phi_0) + b$ as a function of the delivered integrated luminosity. The vertical bars on the points in the upper figure show the uncertainty in the average $m_{\mu\mu}$ of a given ϕ_{μ_+} bin. The shaded bands in the lower figure show the uncertainty in the fitted parameters calculated by a χ^2 regression.

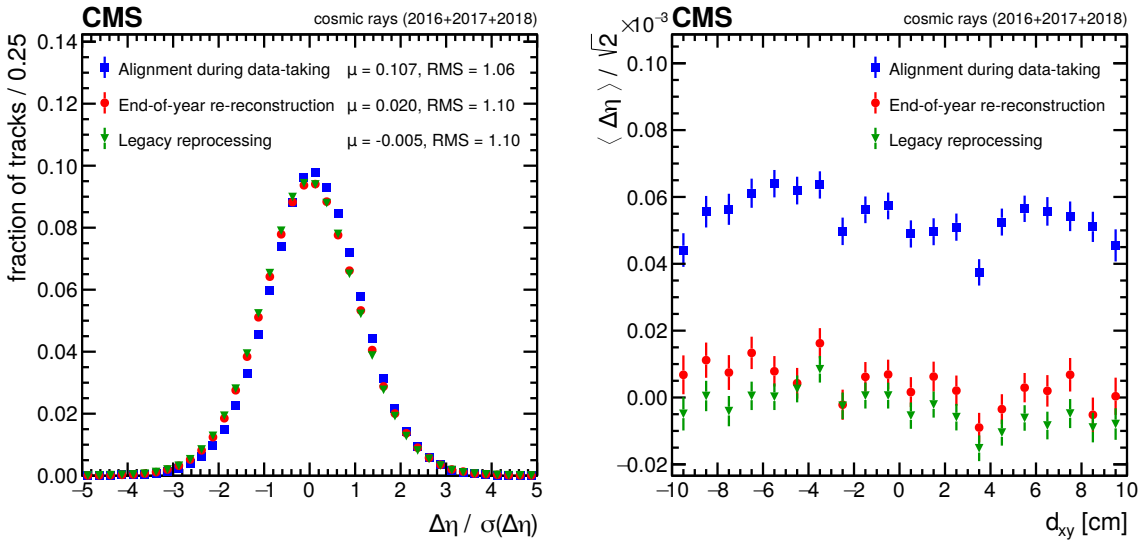

Figure 3.9: Performance results for cosmic ray muon tracks recorded during commissioning and interfill runs at 3.8T during 2016, 2017, and 2018. The top and bottom halves of the cosmic ray track are reconstructed independently and the track parameters are compared at the point of closest approach to the interaction region. The mean and RMS of the distribution of $\Delta\eta$ relative to its uncertainty are shown in the figure on the left. The mean η difference between the two tracks is presented as a function of d_{xy} on the right, scaled down by $\sqrt{2}$ to account for the two independent measurements. The error bars show the statistical uncertainty related to the limited number of tracks.

muon traversing the detector.

From this perspective, the strategy followed in the legacy alignment procedure has led to better performance. In particular, the improvement of the distribution of $\Delta\eta$ relative to its uncertainty is related to the improved statistical precision of the alignment fit. The reduction in the difference between the impact parameters is related to the reduction of systematic distortions; in particular, for the left figure, it can be interpreted as a reduction of the telescope WM.

3.4.3 Overlap validation

The overlap validation was already introduced in Section 3.3. Figure 3.10 shows the mean overlap residuals as a function of the delivered integrated luminosity. The nonzero values, even for the legacy reprocessing, illustrate the limitations of the strategy followed for the alignment fit, where the temporal changes due to the irradiation of the modules are included in the alignment parameters. The biases that were introduced by the radiation damage are artificially absorbed in the alignment constants. Correlations between shifts in the mean overlap in Fig. 3.10 and $\Delta\mu$ in DMR trends demonstrate that the mean overlap is also an effective measure of the Lorentz angle calibration bias. Alternatively, if any observed deviations are assumed to be caused purely by systematic distortions, constraints can be placed on the maximal magnitude of the distortions in the tracker. These constraints represent a worst-case misalignment scenario, where no biases are introduced by radiation damage. In the top row (bottom row) of Fig. 3.10, we observe deviations from zero in the legacy reprocessing ranging from $-21\,\mu$m to $+2\,\mu$m (from $-1.9\,\mu$m to $+5\,\mu$m), which correspond to longitudinal (radial) expansions or contractions ranging from $-105\,\mu$m to $+10\,\mu$m at $z = 26\,$cm ($-5.7\,\mu$m to $+16.5\,\mu$m at $r = 16\,$cm).

3.5 Summary and Outlook

In the above chapter, some of the strategies and the performance of the alignment of the CMS central tracker during the data-taking period from 2015 to 2018 have been described. Systematic distortions arising from the aging of the detector, from internal symmetries of the minimization problem or from external constraints, were

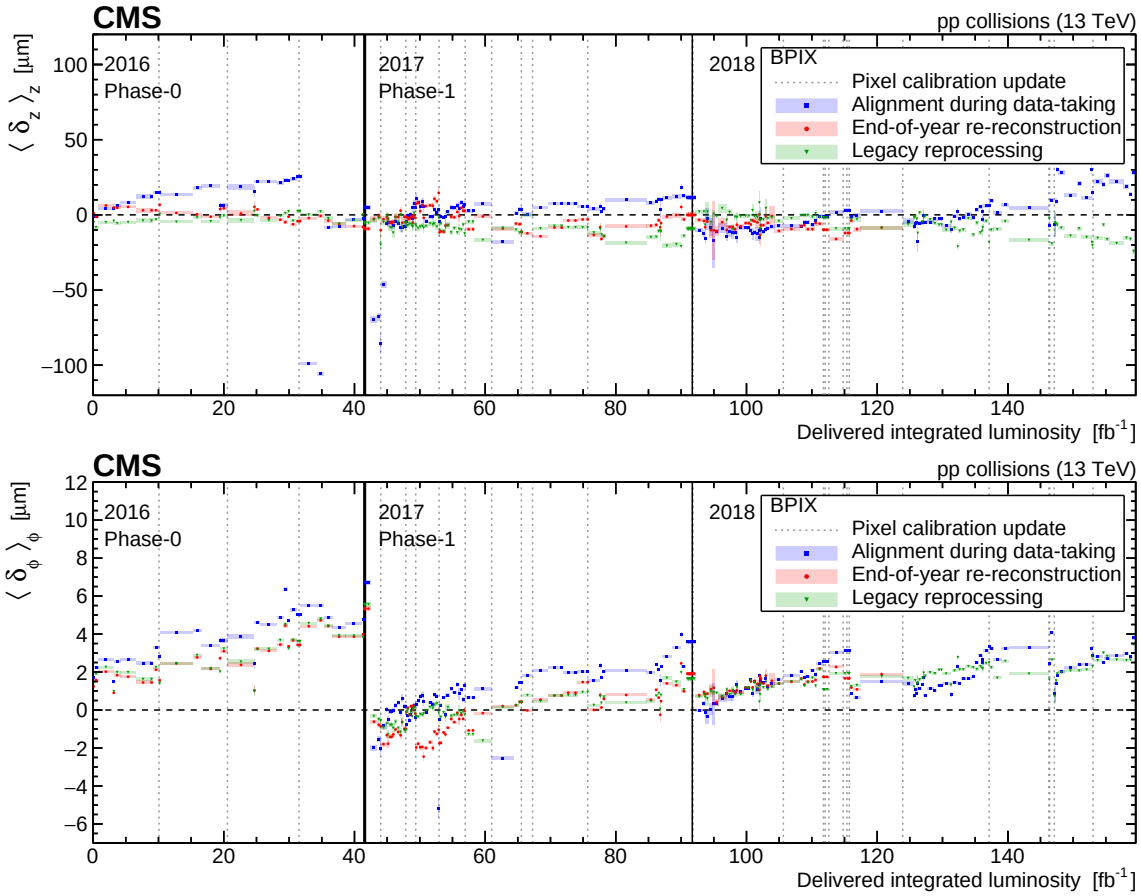

Figure 3.10: The upper (lower) figure shows the mean difference in residuals in the z (ϕ) direction for modules overlapping in the z (ϕ) direction in the BPIX, $\langle\delta_z\rangle$ ($\langle\delta_\phi\rangle$), as a function of the delivered integrated luminosity. The error bars show the statistical uncertainty in the mean of distribution of the residuals. These residuals are calculated using a sample of data recorded with the inclusive L1 trigger.

monitored using specific distributions. Examples of such distributions are the dimuon invariant mass as a function of the kinematical properties of the outgoing muons and the difference of the mean of the distribution of the median of the residuals for modules pointing in opposite directions.

The results and techniques shown here are only representative of the many different alignments and validations produced by the tracker alignment group during Run2 of the LHC. I helped to produce and validate the commissioning alignments of the tracker in the beginning of Run3. After commissioning, there was a very intense campaign to produce the alignments for Run3 which is still ongoing. The analyses that are presented in this thesis take full advantage of the excellent tracking performance resulting from these alignments.

When the High Luminosity LHC (HL-LHC) comes online in 2029, the CMS tracker will be completely replaced. This new tracker will be able to withstand the increased radiation doses expected in the HL-LHC. The new features of this tracker include increased granularity (more modules) and increased forward coverage ($\eta < 4$). The extreme environment of the HL-LHC and the more complicated tracker geometry will make producing quick and precise alignments a challenge. Even now, studies are being performed to meet the challenges of precise tracking in the HL-LHC era. It is clear that tracker alignment will continue to be extremely important for the LHC program over the next 15 years.

Chapter 4

Phenomenological approaches to LHC data

In chapters 1, 2, and 3, I describe the quantum field theory of the SM, as well as the experimental techniques used to analyze high-energy particle collisions with extreme precision using the CMS detector. However, it is not immediately obvious how to link the underlying field theory to experimental observations. Therefore, it is imperative that before performing any analysis of the LHC data, one must deeply understand the underlying theories and carefully design an analysis that is most optimal for the hypothesis being tested. This linking of the underlying theory to experimental observations is called phenomenology. In this chapter, I will present various phenomenological studies that I performed in order to prepare for the experimental measurements presented later in this thesis.

4.1 Anomalous Couplings of the Higgs Boson

The observation of a Higgs boson (H) with a mass of around 125 GeV by the ATLAS and CMS Collaborations in 2012 [53, 2, 54] was consistent with the expectations of the standard model (SM) of particle physics [55, 16, 56, 17, 57, 58, 9]. Constraints on the spin-parity properties and anomalous HVV couplings of the Higgs boson have been set by the CMS [59, 60, 61, 62, 63, 64, 65, 66, 67, 68, 69] and ATLAS [70, 71, 72, 73, 74, 75, 76, 77, 77, 78] experiments. As early as 2012, the $H \to 4\ell$ channel served as the primary mode for determining the spin-parity of the Higgs boson owing to its detailed kinematic features that are highly sensitive to spin correlations in the

decay [59]. The quantum numbers of the Higgs boson were found to be consistent with $J^{PC} = 0^{++}$ [59, 60, 61, 70] but small anomalous HVV couplings to two EW gauge bosons $\mathrm{V} = \gamma, \mathrm{Z}, \mathrm{W}$ are allowed. Due to the Nature of the Higgs sector, any small deviation from the expected couplings in the SM would indicate BSM physics. The most model independent way of parameterizing these small deviations if with Effective Field Theory (EFT), which assumes that the SM remains valid up to a high-energy scale Λ that lies beyond the direct reach of current experiments. In this scenario, new physics is assumed to be heavy and manifests only through effective modifications to the Higgs boson's couplings to vector bosons and other particles. The corresponding amplitude $A(\mathrm{HV_1V_2})$ in Eq. (4.1) takes on a specific form in this framework, as detailed in the following section.

4.2 Parameterization of anomalous interactions

We start with the HVV scattering amplitude of a spin-zero boson H and two vector bosons VV with polarization vectors and momenta ε_1^μ, q_1^μ and ε_2^μ, q_2^μ. The amplitude is parameterized by

$$A(HV_1V_2) = \frac{1}{v} \left\{ M_{V_1}^2 \left(g_1^{VV} + \frac{\kappa_1^{VV} q_1^2 + \kappa_2^{VV} q_2^2}{\left(\Lambda_1^{VV}\right)^2} + \frac{\kappa_3^{VV} (q_1+q_2)^2}{\left(\Lambda_Q^{VV}\right)^2} + \frac{2 q_1 \cdot q_2}{M_{V_1}^2} g_2^{VV} \right) (\varepsilon_1 \cdot \varepsilon_2) \right.$$
$$\left. -2 g_2^{VV} \, (\varepsilon_1 \cdot q_2)(\varepsilon_2 \cdot q_1) - 2 g_4^{VV} \, \varepsilon_{\varepsilon_1 \, \varepsilon_2 \, q_1 \, q_2} \right\}, \tag{4.1}$$

where v is the vacuum expectation value, under the conventions $\varepsilon_{0123} = +1$ and $(q^\mu) = (E, \vec{q})$. This amplitude represents the three possible tensor structures of the Higgs boson's interaction with two vector bosons, with expansion of the terms up

to q_i^2. By symmetry we have $\kappa_1^{ZZ} = \kappa_2^{ZZ}$, but we do not enforce $\kappa_1^{WW} = \kappa_2^{WW}$ for $W^\pm$ bosons. Note that $\kappa_1^{\gamma\gamma} = \kappa_2^{\gamma\gamma} = \kappa_1^{\mathrm{gg}} = \kappa_2^{\mathrm{gg}} = \kappa_1^{Z\gamma} = 0$, while $\kappa_2^{Z\gamma}/(\Lambda_1^{Z\gamma})^2$ may contribute. The coupling $\kappa_3^{VV}/(\Lambda_Q^{VV})^2$ allows for scenarios which violate the gauge symmetries of the SM.

An effective HVV interaction may be generated by loops of fermions, in which case the couplings κ_f and $\tilde{\kappa}_f$ describe the Higgs boson interactions as

$$A(Hf\bar{f}) = -\frac{m_f}{v}\bar{\psi}_f\left(\kappa_f + \mathrm{i}\,\tilde{\kappa}_f\gamma_5\right)\psi_f\,, \tag{4.2}$$

where $\bar{\psi}_f$ and ψ_f are the Dirac spinors and m_f is the fermion mass. For the SM fermions, $(\kappa_f, \tilde{\kappa}_f) = (1, 0)$.

The equivalent Lagrangian for Higgs boson interactions with gauge bosons (in the mass eigenstate parameterization) reads

$$\begin{aligned}\mathcal{L}_{\mathrm{hvv}} = \quad & \frac{h}{v}\Bigg[M_Z^2\left(1+\delta c_z\right)Z_\mu Z^\mu + \frac{M_Z^2}{v^2}c_{zz}Z_{\mu\nu}Z^{\mu\nu} + \frac{e^2}{s_w^2}c_{z\Box}Z_\mu\partial_\nu Z^{\mu\nu} + \frac{M_Z^2}{v^2}\tilde{c}_{zz}Z^{\mu\nu}\tilde{Z}_{\mu\nu} \\ & + 2M_W^2\left(1+\delta c_w\right)W_\mu^+W^{-\mu} + 2\frac{M_W^2}{v^2}c_{ww}W_{\mu\nu}^+W^{-\mu\nu} + \frac{e^2}{s_w^2}c_{w\Box}\left(W_\mu^-\partial_\nu W^{+\mu\nu} + \mathrm{h.}c.\right) \\ & + \frac{e^2}{2s_w^2}\tilde{c}_{ww}W^{+\mu\nu}\tilde{W}_{\mu\nu}^- + \frac{e^2}{2s_wc_w}c_{z\gamma}Z_{\mu\nu}A^{\mu\nu} + \frac{e^2}{2s_wc_w}\tilde{c}_{z\gamma}Z_{\mu\nu}\tilde{A}^{\mu\nu} + \frac{e^2}{s_wc_w}c_{\gamma\Box}Z_\mu\partial_\nu A^{\mu\nu} \\ & + c_{\gamma\gamma}\frac{e^2}{4}A_{\mu\nu}A^{\mu\nu} + \tilde{c}_{\gamma\gamma}\frac{e^2}{4}A^{\mu\nu}\tilde{A}_{\mu\nu} + c_{gg}\frac{g_s^2}{4}G_{\mu\nu}^aG^{a\mu\nu} + \tilde{c}_{gg}\frac{g_s^2}{4}G^{a\mu\nu}\tilde{G}_{\mu\nu}^a\Bigg]\,,\end{aligned} \tag{4.3}$$

in accordance with Eq. (II.2.20) in Ref. [79], where $e^2 = 4\pi\alpha$ and $g_s^2 = 4\pi\alpha_s$ are the squared electromagnetic and strong coupling constants, respectively, and $s_w = \sqrt{1-c_w^2}$ is the sine of the weak mixing angle. The covariant derivative used to derive this

expression is $D_\mu = \partial_\mu - \mathrm{i}\frac{e}{2s_w}\sigma^i W_\mu^i - \mathrm{i}\frac{e}{2c_w}B_\mu$ [79, 80]. We note that the convention $\varepsilon_{0123} = +1$ defines the relative sign of the CP-odd $\tilde{c}_i$ and CP-even c_i couplings [81], while the relative sign in front of the W_μ^i and B_μ terms in the covariant derivative defines the sign of the $Z\gamma$ couplings relative to the ZZ and $\gamma\gamma$. The latter could be viewed as the sign of s_w, if a different convention is adopted.[1]

The generality of our amplitude parameterization allows us to uniquely represent each EFT coefficient in Eq. (4.3) by an anomalous coupling in Eq. (4.1).

$$
\begin{aligned}
&\delta c_z = \frac{1}{2}g_1^{ZZ} - 1\,, \qquad c_{zz} = -\frac{2s_w^2c_w^2}{e^2}g_2^{ZZ}\,, \qquad c_{z\Box} = \frac{M_Z^2 s_w^2}{e^2}\frac{\kappa_1^{ZZ}}{(\Lambda_1^{ZZ})^2}\,,\\
&\tilde{c}_{zz} = -\frac{2s_w^2c_w^2}{e^2}g_4^{ZZ}\,, \qquad \delta c_w = \frac{1}{2}g_1^{WW} - 1\,, \qquad c_{ww} = -\frac{2s_w^2}{e^2}g_2^{WW}\,,\\
&c_{w\Box} = \frac{M_W^2 s_w^2}{e^2}\frac{\kappa_1^{WW}}{(\Lambda_1^{WW})^2}\,, \qquad \tilde{c}_{ww} = -\frac{2s_w^2}{e^2}g_4^{WW}\,, \qquad c_{z\gamma} = -\frac{2s_wc_w}{e^2}g_2^{Z\gamma}\,,\\
&\tilde{c}_{z\gamma} = -\frac{2s_wc_w}{e^2}g_4^{Z\gamma}\,, \qquad c_{\gamma\Box} = \frac{s_wc_w}{e^2}\frac{M_Z^2}{(\Lambda_1^{Z\gamma})^2}\kappa_2^{Z\gamma}\,, \qquad c_{\gamma\gamma} = -\frac{2}{e^2}g_2^{\gamma\gamma}\,,\\
&\tilde{c}_{\gamma\gamma} = -\frac{2}{e^2}g_4^{\gamma\gamma}\,, \qquad c_{gg} = -\frac{2}{g_s^2}g_2^{gg}\,, \qquad \tilde{c}_{gg} = -\frac{2}{g_s^2}g_4^{gg}\,.
\end{aligned}
\tag{4.4}
$$

Note that not every anomalous coupling in Eq. (4.1) has a corresponding term in the EFT Lagrangian of Eq. (4.3). For example, the term $\kappa_3^{VV}/(\Lambda_Q^{VV})^2$ is not gauge invariant and is not present in Eq. (4.3). Similarly, $\kappa_1^{WW} = \kappa_2^{WW}$ due to charge symmetry.

[1] In the actual parameterization of the JHUGen framework discussed in Section 4.3 and Refs. [82, 83, 84, 85, 81, 86], the $D_\mu = \partial_\mu - \mathrm{i}\frac{e}{2s_w}\sigma^i W_\mu^i + \mathrm{i}\frac{e}{2c_w}B_\mu$ convention was adopted for historical reasons. A transformation $g_i^{Z\gamma} \to -g_i^{Z\gamma}$ or $\kappa_i^{Z\gamma} \to -\kappa_i^{Z\gamma}$ of the input parameters in this framework would lead to the convention $D_\mu = \partial_\mu - \mathrm{i}\frac{e}{2s_w}\sigma^i W_\mu^i - \mathrm{i}\frac{e}{2c_w}B_\mu$, which is needed for consistent application of the formalism discussed in this paper.

So far we have discussed the Higgs boson interactions without considering additional symmetries. The SU(3) × SU(2) × U(1) symmetry of the standard model effective field theory (SMEFT) [87, 88, 89, 90] is a motivated framework which allows relating EFT operators. Not all of the EFT coefficients are independent when limiting the discussion to dimension-six interactions with this symmetry. The linear relations for the dependent coefficients can be found in Ref. [79] and they translate into relations amongst our anomalous couplings as follows:

$$g_1^{WW} = g_1^{ZZ} + \frac{\Delta M_W}{M_W}\,, \tag{4.5}$$

$$g_2^{WW} = c_w^2 g_2^{ZZ} + s_w^2 g_2^{\gamma\gamma} + 2 s_w c_w g_2^{Z\gamma}\,, \tag{4.6}$$

$$g_4^{WW} = c_w^2 g_4^{ZZ} + s_w^2 g_4^{\gamma\gamma} + 2 s_w c_w g_4^{Z\gamma}\,, \tag{4.7}$$

$$\frac{\kappa_1^{WW}}{(\Lambda_1^{WW})^2}(c_w^2 - s_w^2) = \frac{\kappa_1^{ZZ}}{(\Lambda_1^{ZZ})^2} + 2 s_w^2 \frac{g_2^{\gamma\gamma} - g_2^{ZZ}}{M_Z^2} + 2\frac{s_w}{c_w}(c_w^2 - s_w^2)\frac{g_2^{Z\gamma}}{M_Z^2}\,, \tag{4.8}$$

$$\frac{\kappa_2^{Z\gamma}}{(\Lambda_1^{Z\gamma})^2}(c_w^2 - s_w^2) = 2 s_w c_w \left(\frac{\kappa_1^{ZZ}}{(\Lambda_1^{ZZ})^2} + \frac{g_2^{\gamma\gamma} - g_2^{ZZ}}{M_Z^2} \right) + 2(c_w^2 - s_w^2)\frac{g_2^{Z\gamma}}{M_Z^2}\,. \tag{4.9}$$

The Lagrangian for Higgs boson interactions with gauge bosons can be written in the Warsaw basis [91] which preserves the SU(3) × SU(2) × U(1) symmetry of SMEFT. The relationship between operators in the Warsaw basis and the mass-eigenstate basis is discussed in Section 4.3.

4.3 The JHU generator framework and the EFT bases

The JHU generator framework (JHUGen) includes a Monte Carlo generator and matrix element techniques for optimal analysis of the data. It is built upon the earlier

developed framework of the JHU generator and MELA analysis package [82, 83, 84, 85, 81, 86] and extensively uses matrix elements provided by MCFM [92, 93, 94, 95, 96]. The SM processes in MCFM are extended to add the most general scalar and gauge couplings and possible additional states. This framework includes many options for production and decay of the H boson, which include the gluon fusion, vector boson fusion, and associated production with a vector boson (VH) in both on-shell H and off-shell H^* production [81]. In the off-shell case, interference with background processes or a second resonance is included. The processes with direct sensitivity to fermion $Hf\bar{f}$ couplings, such as $t\bar{t}H$, $b\bar{b}H$, tqH, tWH, or $H \to \tau^+\tau^-$, are discussed in Refs. [85, 86].

The JHUGen framework was adopted in Run-I analyses using LHC data [2, 59, 60, 97, 70, 98, 99, 61, 62, 100, 71, 63] and employed in recent Run-II measurements of the HVV anomalous couplings from the first joint analysis of on-shell production and decay [64, 66], from the first joint analysis of on-shell and off-shell Higgs boson production [65], for the first measurement of the CP structure of the Yukawa interaction between the Higgs boson and top quark [101], in the search for a second resonance in interference with the continuum background [102, 103], and in EFT approach to the HVV, Hgg, and $Hf\bar{f}$ interactions [104].

4.3.1 EFT basis considerations

The framework is based on the amplitude parameterization in Eqs. (4.1) and (4.2). In order to simplify translation between different coupling conventions and operator bases, including the Higgs and Warsaw bases, within the JHU generator framework, we

provide the JHUGenLexicon program, which includes an interface to the generator and matrix element library and can also be used for standalone or other applications [81]. The relationship of the amplitude parameterization to the mass eigenstate basis of the EFT formulations in Eq. (4.3) is performed through the simple linear relationship in Eq. (4.4). The functionality of this program is similar to Rosetta [105], but it is limited in scope to application to the Higgs boson interactions and provides additional options to introduce certain symmetries or constraints, as illustrated below.

We count five CP-even and three CP-odd independent electroweak HVV operators, as well as one CP-even and one CP-odd Hgg operators in the mass-eigenstate basis in Section 4.2. The same number of independent Higgs boson operators exists in the Warsaw basis. The relationship between the six CP-even operators is quoted explicitly in Eq. (14) of Ref. [105]. This relationship is direct, with the exception of the δv parameter defined in the Warsaw basis in Eq. (15) of Ref. [105]. One could remove an extra parameter from transformation with constraints from precision electroweak data. For example, we can set $\Delta M_W = 0$ in Eq. (4.5), because M_W is measured precisely. This allows us to express δv through the other HVV operators in the Warsaw basis. The JHUGenLexicon program provides such an option and the following studies in this paper will be presented with such a constraint.

With the above symmetries and constraints, including $\Delta M_W = 0$, the translation between the Warsaw basis and the independent amplitude coefficients is

$$\delta g_1^{ZZ} = \frac{v^2}{\Lambda^2}\left(2C_{\mathrm{H}\Box} + \frac{6e^2}{s_w^2}C_{\mathrm{H}WB} + \left(\frac{3c_w^2}{2s_w^2} - \frac{1}{2}\right)C_{\mathrm{H}D}\right),$$

$$
\begin{aligned}
\kappa_1^{ZZ} &= \frac{v^2}{\Lambda^2}\left(-\frac{2e^2}{s_w^2}C_{\mathrm{H}WB} + \left(1-\frac{1}{2s_w^2}\right)C_{\mathrm{H}D}\right), \\
g_2^{ZZ} &= -2\frac{v^2}{\Lambda^2}\left(s_w^2 C_{\mathrm{H}B} + c_w^2 C_{\mathrm{H}W} + s_w c_w C_{\mathrm{H}WB}\right), \\
g_2^{Z\gamma} &= -2\frac{v^2}{\Lambda^2}\left(s_w c_w\left(C_{\mathrm{H}W} - C_{\mathrm{H}B}\right) + \frac{1}{2}\left(s_w^2 - c_w^2\right)C_{\mathrm{H}WB}\right), \\
g_2^{\gamma\gamma} &= -2\frac{v^2}{\Lambda^2}\left(c_w^2 C_{\mathrm{H}B} + s_w^2 C_{\mathrm{H}W} - s_w c_w C_{\mathrm{H}WB}\right), \\
g_2^{\mathrm{gg}} &= -2\frac{v^2}{\Lambda^2}C_{\mathrm{H}G}, \\
g_4^{ZZ} &= -2\frac{v^2}{\Lambda^2}\left(s_w^2 C_{\mathrm{H}\widetilde{B}} + c_w^2 C_{\mathrm{H}\widetilde{W}} + s_w c_w C_{\mathrm{H}\widetilde{W}B}\right), \\
g_4^{Z\gamma} &= -2\frac{v^2}{\Lambda^2}\left(s_w c_w\left(C_{\mathrm{H}\widetilde{W}} - C_{\mathrm{H}\widetilde{B}}\right) + \frac{1}{2}\left(s_w^2 - c_w^2\right)C_{\mathrm{H}\widetilde{W}B}\right), \\
g_4^{\gamma\gamma} &= -2\frac{v^2}{\Lambda^2}\left(c_w^2 C_{\mathrm{H}\widetilde{B}} + s_w^2 C_{\mathrm{H}\widetilde{W}} - s_w c_w C_{\mathrm{H}\widetilde{W}B}\right), \\
g_4^{\mathrm{gg}} &= -2\frac{v^2}{\Lambda^2}C_{\mathrm{H}\widetilde{G}},
\end{aligned}
\tag{4.10}
$$

where Λ is the scale of new physics, which we set to $\Lambda = 1\,\mathrm{TeV}$ as a convention, and δg_1^{ZZ} is the correction to the SM value of $g_1^{ZZ} = 2$. According to Eq. (4.5), $\delta g_1^{WW} = \delta g_1^{ZZ}$, and the other dependent amplitude coefficients can be derived from Eqs. (4.6–4.9).

A numerical example of the relationship between the $C_{\mathrm{H}X} = 1$ contribution of a single operator in the Warsaw basis and the couplings in the mass-eigenstate amplitude in Eq. (4.1) is shown in Table 4.1, which corresponds to the reverse of Eq. (4.10).

4.3.2 Application to the VBF, VH, and $H \to VV$ processes

One of the new of the analyses in this thesis, compared to the earlier work, is the study of the $g_2^{Z\gamma}$, $g_2^{\gamma\gamma}$, $g_4^{Z\gamma}$, and $g_4^{\gamma\gamma}$ anomalous couplings in electroweak production of the

Table 4.1: The values of the couplings in the mass-eigenstate amplitude in Eq. (4.1) corresponding to the $C_{\mathrm{H}X} = 1$ contribution of a single operator in the Warsaw basis with $\Lambda = 1\,\mathrm{TeV}$. The relationship corresponds to the reverse of Eq. (4.10). When quoting the $\kappa_2^{Z\gamma}$ and $\kappa_1^{ZZ} = \kappa_2^{ZZ}$ values, we set $\Lambda_1^{Z\gamma} = \Lambda_1^{ZZ} = 100\,\mathrm{GeV}$ in Eq. (4.1).

	$\delta g_1^{ZZ} = \delta g_1^{WW}$	κ_1^{ZZ}	g_2^{ZZ}	$g_2^{Z\gamma}$	$g_2^{\gamma\gamma}$	g_4^{ZZ}	$g_4^{Z\gamma}$	$g_4^{\gamma\gamma}$	$\kappa_2^{Z\gamma}$	κ_1^{WW}	g_2^{WW}	g_4^{WW}
$C_{\mathrm{H}\Box}$	0.1213	0	0	0	0	0	0	0	0	0	0	0
$C_{\mathrm{H}D}$	0.2679	−0.0831	0	0	0	0	0	0	−0.1320	−0.1560	0	0
C_{HW}	0	0	−0.0929	−0.0513	−0.0283	0	0	0	0	0	−0.1212	0
$C_{\mathrm{HW}B}$	0.1529	−0.0613	−0.0513	0.0323	0.0513	0	0	0	0.1763	0.0360	0	0
$C_{\mathrm{H}B}$	0	0	−0.0283	0.0513	−0.0929	0	0	0	0	0	0	0
$C_{\mathrm{H}\widetilde{\mathrm{W}}}$	0	0	0	0	0	−0.0929	−0.0513	−0.0283	0	0	0	−0.1212
$C_{\mathrm{H}\widetilde{W}B}$	0	0	0	0	0	−0.0513	0.0323	0.0513	0	0	0	0
$C_{\mathrm{H}\widetilde{B}}$	0	0	0	0	0	−0.0283	0.0513	−0.0929	0	0	0	0

Higgs boson. Their effect in the $H \to 4\ell$ process was studied with LHC data [61] and with phenomenological tools [106, 107]. In the following, we re-examine the $H \to 4\ell$ decay and investigate the VBF and VH processes. In the case of VH production, we consider three final states $Z(\to f\bar{f})H$, $\gamma^*(\to f\bar{f})H$, and γH, and both $q\bar{q}$ or gg production channels, as all are affected by the HVV couplings of our interest. While the gluon fusion process formally appears at higher order in QCD, the large gluon parton luminosity at the LHC makes this channel interesting to examine.

In this study, we only examine the operators affecting the Higgs boson interactions in Table 4.1 and study their effect on the HVV couplings. Other operators, such as $HZff$ contact terms for example, are included in the JHUGen framework, but they are not the primary interest in this study because their existence would become evident in resonance searches and in electroweak measurements, without the need for Higgs boson production. Moreover, such contact terms are equivalent to the combination of the κ_1^{ZZ} and $\kappa_2^{Z\gamma}$ couplings if flavor universality is assumed [81]. Not only HVV interactions may be affected by the above operators in the processes under study. For

example, the $C_{\mathrm{HW}B}$ operator also affects the Zff couplings. However, these Zff couplings should be well constrained in electroweak measurements. For this reason, should one of the considered operators affect the Zff interactions, we assume some other operators not affecting the direct Higgs boson interactions must also contribute to bring the Zff couplings to the SM values.

Numerical results of the relative contributions of operators to the $H \to VV \to 4\ell$, VBF, $q\bar{q}$ or $\mathrm{gg} \to V(\to \ell^+\ell^-)H$, and γH processes are shown. The general observations from Tables 4.2–4.4 is that the relative importance of the $g_2^{Z\gamma}$, $g_2^{\gamma\gamma}$, $g_4^{Z\gamma}$, and $g_4^{\gamma\gamma}$ couplings changes between the processes. Taking the example of the $C_{\mathrm{HW}B}$ operator, these couplings lead to an overwhelming contribution in the $H \to 4\ell$ process. However, their contribution in the VBF and VH processes is not significant and is especially tiny in the case of the VH process. These features will affect our ability to use different processes to constraint anomalous couplings with photons. We note that the VH process with $V \to \ell^+\ell^-$ includes both ZH and $\gamma^* H$ production mechanisms, where γ^* leads to low-q^2 contributions in the $m_{\ell\ell}$ invariant mass, which can be observed in kinematic distributions.

The $\mathrm{gg} \to ZH$ process has been shown to have no contributions of the two anomalous HVV tensor structures appearing in Eq. (4.1) in the triangular loop diagram [81]. Therefore, only the SM-like tensor structure with the g_1 and κ_1^{ZZ} couplings contributes to this diagram, as shown in Table 4.5. The off-shell photon does not couple to the triangular fermion loop either [81], and, therefore, the $\kappa_2^{Z\gamma}$ coupling does not contribute. The box diagram is sensitive to the fermion couplings of the Higgs boson, which we do not vary in this study of anomalous HVV interactions. As the result,

Table 4.2: Relative contributions of the individual terms in the mass-eigenstate amplitude to a single operator $C_{\mathrm{H}X}$ in the Warsaw basis expressed as a fraction of the $\mathrm{gg} \to H \to 4\ell$ cross section. The SM contribution is excluded from the HVV coupling, and the cross section ratio to the SM expectation ($\sigma/\sigma_{\mathrm{SM}}$) is shown for $C_{\mathrm{H}X} = 1$ in the first column. The contributions to the $H \to 4\ell$ process are shown with the requirement $m_{\ell\ell} > 1\,\mathrm{GeV}$.

	$\sigma/\sigma_{\mathrm{SM}}$	$\delta g_1^{ZZ} = \delta g_1^{WW}$	κ_1^{ZZ}	g_2^{ZZ}	$g_2^{Z\gamma}$	$g_2^{\gamma\gamma}$	g_4^{ZZ}	$g_4^{Z\gamma}$	$g_4^{\gamma\gamma}$	$\kappa_2^{Z\gamma}$	κ_1^{WW}	g_2^{WW}	g_4^{WW}
$C_{\mathrm{H}\Box}$	0.004	1	0	0	0	0	0	0	0	0	0	0	0
$C_{\mathrm{H}D}$	0.017	1.078	0.068	0	0	0	0	0	0	0.486	0	0	0
C_{HW}	0.635	0	0	0.00117	0.685	0.238	0	0	0	0	0	0	0
$C_{\mathrm{HW}B}$	0.781	0.007	0.001	0.00029	0.268	0.632	0	0	0	0.018	0	0	0
$C_{\mathrm{H}B}$	2.215	0	0	0.00003	0.243	0.759	0	0	0	0	0	0	0
$C_{\mathrm{H}\widetilde{\mathrm{W}}}$	0.579	0	0	0	0	0	0.00052	0.713	0.286	0	0	0	0
$C_{\mathrm{H}\widetilde{W}B}$	0.749	0	0	0	0	0	0.00012	0.239	0.683	0	0	0	0
$C_{\mathrm{H}\widetilde{B}}$	2.196	0	0	0	0	0	0.00001	0.194	0.720	0	0	0	0

the $\mathrm{gg} \to ZH$ process features a rather limited set of EFT operators and we will not study this process in more detail in this paper, leaving further details to Ref. [81].

The γH production process has been largely neglected in analysis of LHC data. However, this process was used in the search for the Higgs boson with anomalous couplings in e^+e^- production prior to the Higgs boson discovery [108] and proposed in application to CP-even EFT operator constraints at the LHC [109, 110]. From Table 4.6, it is evident that only the $g_2^{Z\gamma}$, $g_2^{\gamma\gamma}$, $g_4^{Z\gamma}$, and $g_4^{\gamma\gamma}$ couplings contribute, and this channel does not receive tree-level SM contributions. Because the photon is on-shell, it does not receive contribution from $\kappa_2^{Z\gamma}$ either. This process is generated by the dimension-6 operators squared in the EFT expansion in combination with the EW loops generated by the SM particles. As an approximation to the SM production cross section, we use the calculation with the $g_2^{Z\gamma,\mathrm{SM}}$ and $g_2^{\gamma\gamma,\mathrm{SM}}$ values calculated

Table 4.3: Relative contributions, as in Table 4.2, to the cross section of the VBF process, with the requirement $q_V^2 > 1\,\text{GeV}^2$.

	$\sigma/\sigma_{\text{SM}}$	$\delta g_1^{ZZ} = \delta g_1^{WW}$	κ_1^{ZZ}	g_2^{ZZ}	$g_2^{Z\gamma}$	$g_2^{\gamma\gamma}$	g_4^{ZZ}	$g_4^{Z\gamma}$	$g_4^{\gamma\gamma}$	$\kappa_2^{Z\gamma}$	κ_1^{WW}	g_2^{WW}	g_4^{WW}
$C_{\text{H}\Box}$	0.004	1	0	0	0	0	0	0	0	0	0	0	0
$C_{\text{H}D}$	0.170	0.105	0.081	0	0	0	0	0	0	0.154	0.572	0	0
C_{HW}	0.052	0	0	0.159	0.196	0.059	0	0	0	0	0	0.839	0
$C_{\text{HW}B}$	0.086	0.067	0.086	0.030	0.046	0.115	0	0	0	0.531	0.059	0	0
$C_{\text{H}B}$	0.063	0	0	0.012	0.159	0.522	0	0	0	0	0	0	0
$C_{\text{H}\widetilde{\text{W}}}$	0.043	0	0	0	0	0	0.153	0.207	0.066	0	0	0	0.811
$C_{\text{H}\widetilde{W}B}$	0.012	0	0	0	0	0	0.170	0.304	0.831	0	0	0	0
$C_{\text{H}\widetilde{B}}$	0.059	0	0	0	0	0	0.010	0.156	0.520	0	0	0	0

in Section 4.7. These point-like couplings reproduce the SM decay width of the processes $\text{H} \to Z\gamma$ and $\gamma\gamma$, respectively. Due to the off-shell $V = Z/\gamma^*$ in the process $q\bar{q} \to V \to \gamma H$, these point-like couplings are not expected to reproduce the full EW loop calculation in the SM, but they are expected to provide a good estimate, which we use as $\sigma_{\text{SM}}^{\gamma\text{H}}$ in Table 4.6. The γH process may be of particular interest in isolating the CP-odd couplings $g_4^{Z\gamma}$ and $g_4^{\gamma\gamma}$ in combination with CP-even couplings $g_2^{Z\gamma}$ and $g_2^{\gamma\gamma}$, which is complementary to the $\text{H} \to Z\gamma$ and $\gamma\gamma$ decays.

Table 4.4: Relative contributions, as in Table 4.2, to the cross section of the $q\bar{q} \to V(\to \ell^+\ell^-)H$ process, with the requirement $m_{\ell\ell} > 1\,\text{GeV}$.

	$\sigma/\sigma_{\text{SM}}$	$\delta g_1^{ZZ} = \delta g_1^{WW}$	κ_1^{ZZ}	g_2^{ZZ}	$g_2^{Z\gamma}$	$g_2^{\gamma\gamma}$	g_4^{ZZ}	$g_4^{Z\gamma}$	$g_4^{\gamma\gamma}$	$\kappa_2^{Z\gamma}$	κ_1^{WW}	g_2^{WW}	g_4^{WW}
$C_{\text{H}\Box}$	0.004	1	0	0	0	0	0	0	0	0	0	0	0
$C_{\text{H}D}$	0.949	0.019	0.655	0	0	0	0	0	0	1.026	0	0	0
C_{HW}	0.154	0	0	1.087	0.294	0.017	0	0	0	0	0	0	0
$C_{\text{HW}B}$	2.265	0.003	0.151	0.022	0.008	0.004	0	0	0	0.774	0	0	0
$C_{\text{H}B}$	0.125	0	0	0.125	0.366	0.232	0	0	0	0	0	0	0
$C_{\text{H}\widetilde{\text{W}}}$	0.097	0	0	0	0	0	1.044	0.330	0.023	0	0	0	0
$C_{\text{H}\widetilde{W}B}$	0.057	0	0	0	0	0	0.536	0.218	0.125	0	0	0	0
$C_{\text{H}\widetilde{B}}$	0.090	0	0	0	0	0	0.106	0.353	0.263	0	0	0	0

Table 4.5: Relative contributions, as in Table 4.2, to the cross section of the $gg \to Z(\to \ell^+\ell^-)H$ process, with the requirement $m_{\ell\ell} > 1\,\text{GeV}$.

	$\sigma/\sigma_{\text{SM}}$	$\delta g_1^{ZZ} = \delta g_1^{WW}$	κ_1^{ZZ}	g_2^{ZZ}	$g_2^{Z\gamma}$	$g_2^{\gamma\gamma}$	g_4^{ZZ}	$g_4^{Z\gamma}$	$g_4^{\gamma\gamma}$	$\kappa_2^{Z\gamma}$	κ_1^{WW}	g_2^{WW}	g_4^{WW}
$C_{\text{H}\Box}$	0.009	1	0	0	0	0	0	0	0	0	0	0	0
$C_{\text{H}D}$	8.055	0.006	1.100	0	0	0	0	0	0	0	0	0	0
C_{HW}	0	0	0	0	0	0	0	0	0	0	0	0	0
$C_{\text{HW}B}$	4.495	0.003	1.066	0	0	0	0	0	0	0	0	0	0
$C_{\text{H}B}$	0	0	0	0	0	0	0	0	0	0	0	0	0
$C_{\text{H}\widetilde{\text{W}}}$	0	0	0	0	0	0	0	0	0	0	0	0	0
$C_{\text{H}\widetilde{W}B}$	0	0	0	0	0	0	0	0	0	0	0	0	0
$C_{\text{H}\widetilde{B}}$	0	0	0	0	0	0	0	0	0	0	0	0	0

Table 4.6: Relative contributions, as in Table 4.2, to the cross section of the $q\bar{q} \to \gamma H$ process.

	$\sigma/\sigma_{\text{SM}}^{\gamma\text{H}}$	$\delta g_1^{ZZ} = \delta g_1^{WW}$	κ_1^{ZZ}	g_2^{ZZ}	$g_2^{Z\gamma}$	$g_2^{\gamma\gamma}$	g_4^{ZZ}	$g_4^{Z\gamma}$	$g_4^{\gamma\gamma}$	$\kappa_2^{Z\gamma}$	κ_1^{WW}	g_2^{WW}	g_4^{WW}
$C_{\text{H}\Box}$	0	0	0	0	0	0	0	0	0	0	0	0	0
$C_{\text{H}D}$	0	0	0	0	0	0	0	0	0	0	0	0	0
C_{HW}	60.3	0	0	0	1.190	0.197	0	0	0	0	0	0	0
$C_{\text{HW}B}$	41.1	0	0	0	0.688	0.956	0	0	0	0	0	0	0
$C_{\text{H}B}$	271.3	0	0	0	0.260	0.472	0	0	0	0	0	0	0
$C_{\text{H}\widetilde{\text{W}}}$	60.1	0	0	0	0	0	0	1.182	0.198	0	0	0	0
$C_{\text{H}\widetilde{W}B}$	41.7	0	0	0	0	0	0	0.677	0.930	0	0	0	0
$C_{\text{H}\widetilde{B}}$	273.9	0	0	0	0	0	0	0.263	0.472	0	0	0	0

4.4 Parameterization of Cross Sections

In this Section, we discuss the relationship between the coupling constants and the cross section of a process involving the Higgs boson. In Ref. [81], we calculated the scaling factors for the partial decay widths in the nine dominant Higgs boson decay modes as a function of anomalous couplings a_i, including the $H \to$ gg, $\gamma\gamma$, and $Z\gamma$ decays, by resolving the loop contributions. However, we omitted point-like contributions such as $g_{2,4}^{\gamma\gamma}$ and $g_{2,4}^{Z\gamma}$ due to their relatively lower importance in the VBF, VH, and $H \to 4f$ processes. Such couplings could be generated by a heavy quark $\mathcal{Q}$ with mass $m_{\mathcal{Q}} \gg M_H$. We assume that its couplings to the Higgs boson are $\kappa_{\mathcal{Q}}$ and $\tilde{\kappa}_{\mathcal{Q}}$, the number of colors N_c, the electric charge Q, and the weak isospin projection $T^{3\mathrm{L}}$. This special model allows us to derive the point-like interactions and relate those to the partial decay widths. While derivation applies to this special case, the final expression in terms of the $g_{2,4}^{\mathrm{gg}}$, $g_{2,4}^{\gamma\gamma}$, and $g_{2,4}^{Z\gamma}$ couplings becomes generic and remains valid for any new physics in the loop, generated by any combination of heavy fermions or bosons. Therefore, the resulting expressions are applicable to the general treatment of these loops in the EFT approach.

First, we recall that in the narrow-width approximation for on-shell Higgs boson production and decay, the cross section can be expressed as

$$\sigma(i \to H \to f) \propto \frac{\left(\sum \alpha_{jk}^{(i)} a_j a_k\right)\left(\sum \alpha_{lm}^{(f)} a_l a_m\right)}{\Gamma_{\mathrm{tot}}}\,, \tag{4.11}$$

where the total width $\Gamma_{\mathrm{tot}} = \Gamma_{\mathrm{known}} + \Gamma_{\mathrm{other}}$ representing decays to known particles and other unknown final states, either invisible or undetected in experiment. In the

following we will focus on decay to the known SM particles which can be expressed as a sum of all partial decay widths as

$$\Gamma_{\text{known}} = \Gamma_{\text{tot}}^{\text{SM}} \times \sum_f \left(\frac{\Gamma_f^{\text{SM}}}{\Gamma_{\text{tot}}^{\text{SM}}} \times \frac{\Gamma_f}{\Gamma_f^{\text{SM}}} \right) = \sum_f \Gamma_f^{\text{SM}} R_f \,, \tag{4.12}$$

where R_f is the scaling factor as function of the coupling constants a_i, and Γ_f^{SM} is the SM value of the partial decay width in the final state f.

In the following, we rely on JHUGen framework implementation, discussed in Section 4.3 and Ref. [81], to derive the loop contributions of the SM particles and the heavy quark $\mathcal{Q}$ to the scaling factor R_{gg}, for both CP-even and CP-odd couplings. The CP-even coupling contributions of the quarks and W boson to $R_{\gamma\gamma}$ and $R_{\text{Z}\gamma}$ are derived with HDECAY [111]. The CP-odd contributions to $R_{\gamma\gamma}$ are calculated with the JHUGen framework in a manner analogous to R_{gg}. The CP-odd contributions to $R_{Z\gamma}$ are calculated using cHDECAY [112].

The ratio of the decay width to the SM expectation in the $H \to$ gg process [81] is found to be

$$\begin{aligned} R_{\text{gg}} = \quad & 1.1068\,\kappa_t^2 + 0.0082\,\kappa_b^2 - 0.1150\,\kappa_t\kappa_b + 2.5717\,\tilde{\kappa}_t^2 + 0.0091\,\tilde{\kappa}_b^2 - 0.1982\,\tilde{\kappa}_t\tilde{\kappa}_b \\ & + 1.0298\,(N_c/3)^2\kappa_{\mathcal{Q}}^2 + 2.1357\,(N_c/3)\kappa_{\mathcal{Q}}\kappa_t - 0.1109\,(N_c/3)\kappa_{\mathcal{Q}}\kappa_b \\ & + 2.3170\,(N_c/3)^2\tilde{\kappa}_{\mathcal{Q}}^2 + 4.8821\,(N_c/3)\tilde{\kappa}_{\mathcal{Q}}\tilde{\kappa}_t - 0.1880\,(N_c/3)\tilde{\kappa}_{\mathcal{Q}}\tilde{\kappa}_b \,. \end{aligned} \tag{4.13}$$

The $\kappa_{\mathcal{Q}}$ and $\tilde{\kappa}_{\mathcal{Q}}$ couplings are connected to the g_2^{gg} and g_4^{gg} point-like interactions

introduced in Eq. (4.1) through

$$g_2^{\mathrm{gg},\mathcal{Q}} = -\alpha_s N_c \kappa_{\mathcal{Q}}/(18\pi)\,, \qquad g_4^{\mathrm{gg},\mathcal{Q}} = -\alpha_s N_c \tilde{\kappa}_{\mathcal{Q}}/(12\pi)\,. \tag{4.14}$$

One can rewrite Eq. (4.13) in terms of the g_2^{gg} and g_4^{gg} couplings in place of $N_c\kappa_{\mathcal{Q}}$ and $N_c\tilde{\kappa}_{\mathcal{Q}}$ by substituting Eq. (4.14). Even though Eq. (4.14) is derived in the special case of a heavy quark, the resulting expression of R_{gg} as a function of g_2^{gg} and g_4^{gg} and other terms is valid for any heavy particles in the loop that generate these point-like interactions.

The latter observation allows us to obtain the value of the effective g_2^{gg} coupling which leads to the SM cross section in the gluons fusion process. By setting all couplings, other than g_2^{gg}, to zero and $R_{\mathrm{gg}} = 1$ in Eq. (4.13), we obtain

$$g_2^{\mathrm{gg,SM}} = -0.00621\,. \tag{4.15}$$

The $g_2^{\mathrm{gg,SM}}$ value differs by only 1.5% from the value that one would obtain in the heavy top mass limit by setting $\kappa_{\mathcal{Q}} = 1$ and $N_c = 3$ in Eq. (4.14), and the sign follows the prediction in this limit.

An approximate way to express Eq. (4.13) with the point-like interactions only in the case of SM couplings of fermions $\kappa_t = \kappa_b = 1$ and $\tilde{\kappa}_t = \tilde{\kappa}_b = 0$ would be to substitute the top and bottom quark contributions with an effective coupling $g_2^{\mathrm{gg,SM}}$

from Eq. (4.15), substitute $\kappa_{\mathcal{Q}}$ and $\tilde{\kappa}_{\mathcal{Q}}$ for $g_2^{\rm gg}$ and $g_4^{\rm gg}$, and obtain

$$R_{\rm gg} \simeq \frac{1}{\left(g_2^{\rm gg,SM}\right)^2}\left[\left(g_2^{\rm gg,SM}+g_2^{\rm gg}\right)^2+\left(g_4^{\rm gg}\right)^2\right]. \tag{4.16}$$

For the $H\to\gamma\gamma$ final states, we include the W boson in addition to the top, bottom, and heavy $\mathcal{Q}$ quarks in the loop and obtain[2]

$$\begin{aligned} R_{\gamma\gamma} = \quad & 1.60932\left(\frac{g_1^{WW}}{2}\right)^2 - 0.69064\left(\frac{g_1^{WW}}{2}\right)\kappa_t + 0.00912\left(\frac{g_1^{WW}}{2}\right)\kappa_b \\ & -0.49725\left(\frac{g_1^{WW}}{2}\right)\left(N_c\,Q^2\,\kappa_{\mathcal{Q}}\right) + 0.07404\,\kappa_t^2 + 0.00002\,\kappa_b^2 - 0.00186\,\kappa_t\kappa_b \\ & +0.03841\left(N_c\,Q^2\,\kappa_{\mathcal{Q}}\right)^2 + 0.10666\,\kappa_t\left(N_c\,Q^2\,\kappa_{\mathcal{Q}}\right) - 0.00136\,\kappa_b\left(N_c\,Q^2\,\kappa_{\mathcal{Q}}\right) \\ & +0.20533\,\tilde{\kappa}_t^2 + 0.00006\,\tilde{\kappa}_b^2 - 0.00300\,\tilde{\kappa}_t\tilde{\kappa}_b + 0.10252\left(N_c\,Q^2\,\tilde{\kappa}_{Q}\right)^2 \\ & +0.29018\,\tilde{\kappa}_t\left(N_c\,Q^2\,\tilde{\kappa}_{\mathcal{Q}}\right) - 0.00202\,\tilde{\kappa}_b\left(N_c\,Q^2\,\tilde{\kappa}_{\mathcal{Q}}\right). \end{aligned} \tag{4.17}$$

For the contribution of a heavy quark in the loop we find

$$g_2^{\gamma\gamma,\mathcal{Q}} = -\frac{\alpha}{3\pi}N_c\,Q^2\,\kappa_{\mathcal{Q}}\,, \qquad g_4^{\gamma\gamma,\mathcal{Q}} = -\frac{\alpha}{2\pi}N_c\,Q^2\,\tilde{\kappa}_{\mathcal{Q}}. \tag{4.18}$$

Following the idea described above for $R_{\rm gg}$, one can rewrite Eq. (4.17) in terms of the $g_2^{\gamma\gamma}$ and $g_4^{\gamma\gamma}$ couplings in place of $N_cQ^2\kappa_{\mathcal{Q}}$ and $N_cQ^2\tilde{\kappa}_{\mathcal{Q}}$ by substituting Eq. (4.18). The final expression of $R_{\gamma\gamma}$ as a function of $g_2^{\gamma\gamma}$ and $g_4^{\gamma\gamma}$ and other terms is again valid for any heavy particles in the loop, fermions or bosons, that generate these point-like

[2]Due to updated EW parameters, there is a small change in the numerical values of coefficients in Eqs. (4.17) and (4.26) that are in common with Ref. [81].

interactions. By setting all couplings other than $g_2^{\gamma\gamma}$ to zero and $R_{\gamma\gamma} = 1$ in Eq. (4.17), we obtain the effective coupling which leads to the SM cross section

$$g_2^{\gamma\gamma,\mathrm{SM}} = 0.00423\,. \tag{4.19}$$

The $g_2^{\gamma\gamma,\mathrm{SM}}$ value differs slightly from 0.00400 obtained from the general expression of the SM loops derived from Refs. [113, 114] and shown in Eq. (4.20). The difference could be explained by the higher-order effects incorporated in Eq. (4.17) and the fact that in our approach we match the SM rate $R_{\gamma\gamma} = 1$. The sign in Eq. (4.19) follows Eq. (4.20).

$$\begin{aligned} g_2^{\gamma\gamma} &= \left(-\frac{\alpha}{4\pi}\right)\left[\left(\frac{g_1^{WW}}{2}\right) \times A_1^{\gamma\gamma}(\tau_W) + \kappa_t N_c Q_t^2 \times A_{1/2}^{\gamma\gamma}(\tau_t)\right] \\ &= 0.00516\left(\frac{g_1^{WW}}{2}\right) - 0.00116\kappa_t, \end{aligned} \tag{4.20}$$

where the one-loop functions are given by

$$A_1^{\gamma\gamma}(\tau_W) = \begin{cases} -8.32 & \text{for} \quad \tau_W = M_W^2/M_H^2 \\ -7 & \text{for} \quad \tau_W \to \infty \end{cases} \tag{4.21}$$

and

$$A_{1/2}^{\gamma\gamma}(\tau_t) = \begin{cases} +1.38 & \text{for} \quad \tau_t = m_t^2/M_H^2 \\ +4/3 & \text{for} \quad \tau_t \to \infty \end{cases}. \tag{4.22}$$

An approximate way to express Eq. (4.17) with point-like interactions only would be to follow the idea used to create Eq. (4.16) and substitute the SM couplings with $g_2^{\gamma\gamma,\mathrm{SM}}$ from Eq. (4.19), substitute $\kappa_{\mathcal{Q}}$ and $\tilde{\kappa}_{\mathcal{Q}}$ for $g_2^{\gamma\gamma}$ and $g_4^{\gamma\gamma}$, and obtain

$$R_{\gamma\gamma} \simeq \frac{1}{\left(g_2^{\gamma\gamma,\mathrm{SM}}\right)^2}\left[\left(g_2^{\gamma\gamma,\mathrm{SM}}+g_2^{\gamma\gamma}\right)^2+\left(g_4^{\gamma\gamma}\right)^2\right]. \tag{4.23}$$

For the $H\to Z\gamma$ final states, for the coupling of the heavy $\mathcal{Q}$ quark to the Z boson, we introduce the following parameter

$$\mathcal{R}_{\mathcal{Q}} = Q\,\frac{T_{\mathcal{Q}}^{3\mathrm{L}} - 2s_w^2\,Q}{s_w c_w}\,, \tag{4.24}$$

which corresponds to the following values for the SM parameters of the top ($T_t^{3\mathrm{L}} = +1/2$, $Q_t = +2/3$) and bottom ($T_b^{3\mathrm{L}} = -1/2$, $Q_b = -1/3$) quarks

$$\mathcal{R}_t = 0.3032\,, \qquad \mathcal{R}_b = 0.2735\,. \tag{4.25}$$

We obtain

$$\begin{aligned} R_{Z\gamma} = \quad & 1.11965\left(\frac{g_1^{WW}}{2}\right)^2 - 0.12652\left(\frac{g_1^{WW}}{2}\right)\kappa_t + 0.00348\left(\frac{g_1^{WW}}{2}\right)\kappa_b \\ & -0.13021\left(\frac{g_1^{WW}}{2}\right)\left(N_c\,\mathcal{R}_{\mathcal{Q}}\kappa_{\mathcal{Q}}\right) + 0.00357\,\kappa_t^2 + 0.000003\,\kappa_b^2 - 0.00018\,\kappa_t\kappa_b \\ & +0.00377\,\left(N_c\,\mathcal{R}_{\mathcal{Q}}\kappa_{\mathcal{Q}}\right)^2 + 0.00734\,\kappa_t\left(N_c\,\mathcal{R}_{\mathcal{Q}}\kappa_{\mathcal{Q}}\right) - 0.00019\,\kappa_b\left(N_c\,\mathcal{R}_{\mathcal{Q}}\kappa_{\mathcal{Q}}\right) \\ & +0.00849\,\tilde{\kappa}_t^2 + 0.000004\,\tilde{\kappa}_b^2 - 0.00025\,\tilde{\kappa}_t\tilde{\kappa}_b + 0.00883\,\left(N_c\,\mathcal{R}_{\mathcal{Q}}\tilde{\kappa}_{\mathcal{Q}}\right)^2 \\ & +0.01723\,\tilde{\kappa}_t\left(N_c\,\mathcal{R}_{\mathcal{Q}}\tilde{\kappa}_{\mathcal{Q}}\right) - 0.00024\,\tilde{\kappa}_b\left(N_c\,\mathcal{R}_{\mathcal{Q}}\tilde{\kappa}_{\mathcal{Q}}\right)\,. \end{aligned} \tag{4.26}$$

For the contribution of a heavy forth generation quarks in the loop we find

$$g_2^{Z\gamma,\mathcal{Q}} = -\frac{\alpha}{6\pi} N_c \, \mathcal{R}_{\mathcal{Q}} \, \kappa_{\mathcal{Q}} \,, \qquad g_4^{Z\gamma,\mathcal{Q}} = -\frac{\alpha}{4\pi} N_c \, \mathcal{R}_{\mathcal{Q}} \, \tilde{\kappa}_{\mathcal{Q}} \,. \tag{4.27}$$

We note that the effective value of $g_2^{Z\gamma}$ for a heavy quark $\mathcal{Q}$ which reproduces the SM partial width, is

$$g_2^{Z\gamma,\mathrm{SM}} = 0.00675. \tag{4.28}$$

The $g_2^{Z\gamma,\mathrm{SM}}$ value differs slightly from 0.00724 obtained from the general expression of the SM loops derived from Refs. [113, 114][3] and shown in Eq. (4.29). As before, the difference could be explained by the higher-order effects incorporated in Eq. (4.26) and the fact that in our approach we match the SM rate $R_{Z\gamma} = 1$. The sign in Eq. (4.28) follows Eq. (4.29).

$$\begin{aligned} g_2^{Z\gamma} &= \frac{\alpha}{4\pi}\left[\left(\frac{g_1^{WW}}{2}\right)\frac{c_w}{s_w} \times A_1^{Z\gamma}(\tau_W) + \kappa_t N_c \mathcal{R}_t \times A_{1/2}^{Z\gamma}(\tau_t)\right] \\ &= 0.00747\left(\frac{g_1^{WW}}{2}\right) - 0.00023\kappa_t, \end{aligned} \tag{4.29}$$

where the one-loop functions are given by $A_1^{Z\gamma}\left(M_W^2/M_H^2\right) = 6.58$ and $A_{1/2}^{Z\gamma}\left(m_t^2/M_H^2\right) = -0.35$.

An approximate way to express Eq. (4.26) with point-like interactions only would be to substitute the SM contributions with an effective coupling $g_2^{Z\gamma,\mathrm{SM}}$ from Eq. (4.28),

[3]We thank Ian Low for updating the results in Eq. (7) of Ref. [113].

substitute $\kappa_{\mathcal{Q}}$ and $\tilde{\kappa}_{\mathcal{Q}}$ for $g_2^{Z\gamma}$ and $g_4^{Z\gamma}$, and obtain

$$R_{Z\gamma} \simeq \frac{1}{\left(g_2^{Z\gamma,\mathrm{SM}}\right)^2}\left[\left(g_2^{Z\gamma,\mathrm{SM}}+g_2^{Z\gamma}\right)^2+\left(g_4^{Z\gamma}\right)^2\right]. \tag{4.30}$$

In the above calculation, the $H \to \gamma^*\gamma$ process is not included, for which the full loop calculation with anomalous couplings is not available. For the $H \to ZZ/Z\gamma^*/\gamma^*\gamma^* \to$ four-fermion final state, the full one-loop calculation with anomalous couplings is not available either. For the leading tree-level contributions, we derived the $R_{ZZ/Z\gamma^*/\gamma^*\gamma^*}$ parameterization in Ref. [81], in which case we set $g_2^{Z\gamma} = g_4^{Z\gamma} = g_2^{\gamma\gamma} = g_4^{\gamma\gamma} = 0$ to avoid collinear singularities. In the following, we introduce these four couplings and avoid singularities in the $\gamma^* \to 2f$ transition with the finite fermion mass threshold $q^2 > (2m_f)^2$. We set $\Lambda_1^{Z\gamma} = \Lambda_1^{ZZ} = 100\,\mathrm{GeV}$ in Eq. (4.1) and rely on the $\kappa_2^{Z\gamma}$ and $\kappa_1^{ZZ} = \kappa_2^{ZZ}$ parameters to express the scaling factor as[4]

$$\begin{aligned}
R_{ZZ/Z\gamma^*/\gamma^*\gamma^*} = \quad & \left(\frac{g_1^{ZZ}}{2}\right)^2 + 0.17\left(\kappa_1^{ZZ}\right)^2 + 0.09\left(g_2^{ZZ}\right)^2 + 0.04\left(g_4^{ZZ}\right)^2 + 0.10\left(\kappa_2^{Z\gamma}\right)^2 \\
& + 79.95\left(g_2^{Z\gamma}\right)^2 + 75.23\left(g_4^{Z\gamma}\right)^2 + 29.00\left(g_2^{\gamma\gamma}\right)^2 + 29.47\left(g_4^{\gamma\gamma}\right)^2 \\
& + 0.81\frac{g_1^{ZZ}}{2}\kappa_1^{ZZ} + 0.50\frac{g_1^{ZZ}}{2}g_2^{ZZ} + 0\times\frac{g_1^{ZZ}}{2}g_4^{ZZ} - 0.19\frac{g_1^{ZZ}}{2}\kappa_2^{Z\gamma} \\
& - 1.56\frac{g_1^{ZZ}}{2}g_2^{Z\gamma} + 0\times\frac{g_1^{ZZ}}{2}g_4^{Z\gamma} + 0.06\frac{g_1^{ZZ}}{2}g_2^{\gamma\gamma} + 0\times\frac{g_1^{ZZ}}{2}g_4^{\gamma\gamma} \\
& + 0.21\kappa_1^{ZZ}g_2^{ZZ} + 0\times\kappa_1^{ZZ}g_4^{ZZ} - 0.07\kappa_1^{ZZ}\kappa_2^{Z\gamma} - 0.64\kappa_1^{ZZ}g_2^{Z\gamma} \\
& + 0\times\kappa_1^{ZZ}g_4^{Z\gamma} + 0.00\kappa_1^{ZZ}g_2^{\gamma\gamma} + 0\times\kappa_1^{ZZ}g_4^{\gamma\gamma} + 0\times g_2^{ZZ}g_4^{ZZ} \\
& - 0.05g_2^{ZZ}\kappa_2^{Z\gamma} - 0.51g_2^{ZZ}g_2^{Z\gamma} + 0\times g_2^{ZZ}g_4^{Z\gamma} - 0.02g_2^{ZZ}g_2^{\gamma\gamma}
\end{aligned}$$

[4]There is a sign change of the $\kappa_2^{Z\gamma}$ coupling when compared to coefficients in common with Ref. [81], because here we use the convention $D_\mu = \partial_\mu - \mathrm{i}\frac{e}{2s_w}\sigma^i W_\mu^i - \mathrm{i}\frac{e}{2c_w}B_\mu$, as discussed in Section 4.2.

$$
\begin{aligned}
&+0\times g_2^{ZZ}g_4^{\gamma\gamma}+0\times g_4^{ZZ}\kappa_2^{Z\gamma}+0\times g_4^{ZZ}g_2^{Z\gamma}+0.36 g_4^{ZZ}g_4^{Z\gamma}\\
&+0\times g_4^{ZZ}g_2^{\gamma\gamma}-0.57 g_4^{ZZ}g_4^{\gamma\gamma}+1.80\kappa_2^{Z\gamma}g_2^{Z\gamma}+0\times\kappa_2^{Z\gamma}g_4^{Z\gamma}\\
&-0.05\kappa_2^{Z\gamma}g_2^{\gamma\gamma}+0\times\kappa_2^{Z\gamma}g_4^{\gamma\gamma}+0\times g_2^{Z\gamma}g_4^{Z\gamma}-1.84 g_2^{Z\gamma}g_2^{\gamma\gamma}\\
&+0\times g_2^{Z\gamma}g_4^{\gamma\gamma}+0\times g_4^{Z\gamma}g_2^{\gamma\gamma}-2.09 g_4^{Z\gamma}g_4^{\gamma\gamma}+0\times g_2^{\gamma\gamma}g_4^{\gamma\gamma}
\end{aligned}
\tag{4.31}
$$

Equation (4.31) covers all final states with $Z/\gamma^* \to q\bar{q}$ and $\ell^+\ell^-$ with quarks and charged leptons, while neutrinos are included with $Z \to \nu\bar{\nu}$. The interference between the CP-odd and CP-even contribution integrates out to zero, as reflected in the zero terms in Eq. (4.31).

Let us conclude this Section by discussing the cross section of the $q\bar{q} \to \gamma H$ process as a function of the anomalous couplings summarized in Table 4.6. Detecting or setting limits on this process will be of interest for constraining the following couplings, as discussed in Section 4.3:

$$
\begin{aligned}
\frac{\sigma(q\bar{q}\to\gamma H)}{\sigma_{\rm ref}^{\gamma\rm H}} = \left(g_2^{Z\gamma}\right)^2+\left(g_4^{Z\gamma}\right)^2 \quad & +0.553\,(g_2^{\gamma\gamma})^2\\
& +0.553\,(g_4^{\gamma\gamma})^2-0.578\,g_2^{Z\gamma}g_2^{\gamma\gamma}-0.578\,g_4^{Z\gamma}g_4^{\gamma\gamma}
\end{aligned}
\tag{4.32}
$$

where the reference cross section is $\sigma_{\rm ref}^{\gamma\rm H} = 1.33\times10^4$ fb.

4.5 SMEFT effects in Higgs Production and Decay

The kinematic effects in the $H \to VV$, VBF, and VH processes can typically be described with five angular observables and two invariant masses, or q_i^2 of the two

vector bosons, as illustrated in Fig. 5.16 [82, 84, 81]. The distributions of two of these angles, θ^* and Φ_1, are random for a spin-zero Higgs boson, but are less trivial for a higher-spin resonance or non-resonant production. In the following, we disentangle the relative contributions of the ZZ, WW, $Z\gamma$, and $\gamma\gamma$ intermediate vector-boson states to simulation with a given operator in the Warsaw basis. Such a decomposition reveals interesting kinematic effects and also allows us to validate the tools used for simulation of EFT effects and match their conventions.

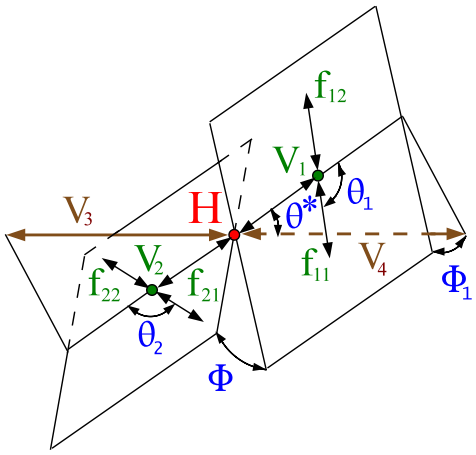

Figure 4.1: Three kinematic topologies of the Higgs boson production and decay [81]: vector boson fusion $q_{12}q_{22} \to q_{11}q_{21}(V_1V_2 \to H \to V_3V_4)$, VH production $q_{11}q_{12} \to V_1 \to V_2(H \to V_3V_4)$, and four-fermion decay $V_3V_4 \to H \to V_1V_2 \to 4f$.

We use the JHUGen program to generate several models which allow us to visualize the relative contributions of the mass eigenstates of the vector bosons. We also model the inclusive kinematic distributions with the SMEFTsim program [115] using MadGraph5 simulation [116]. Once the sign conventions are matched, as discussed in Section 4.2, we find good agreement. A similar comparison with SM couplings using the Prophecy4f [117] and HAWK [118] generators is shown in Section 4.7. Throughout this paper and unless otherwise noted, the calculations are performed

at LO in QCD and EW, with the $\overline{\text{MS}}$-mass for the top quark $m_t = 162.7\,\text{GeV}$, the on-shell mass for the bottom quark $m_b = 4.18\,\text{GeV}$, QCD scale $\mu = M_H/2$, $\alpha_s = 0.1188$, $\alpha = 1/128$, $s_w^2 = 0.23119$, $G_F = 1.16639 \times 10^{-5}$ GeV^{-2} [119], and the NNPDF 3.0 parton distribution functions [120].

In the $H \to 4\ell$ and VH processes, we require $m_{\ell\ell} > 1\,\text{GeV}$. In the VBF process, we apply the selection requirements $m_{jj} > 300\,\text{GeV}$, $p_T^{\text{jet}} > 1\,\text{GeV}$, $|\eta^{\text{jet}}| < 5$, $\Delta\eta_{jj} > 1$, $\Delta R_{jj} > 0.3$, $\sqrt{q_V^2} > 15\,\text{GeV}$. In the $H \to 4\ell$ decay, we model the $C_{HWB} = 1$ contribution to the SM, as shown in Fig. 4.2 with cross section decomposition presented in Table 4.2. In VBF or VH, we model the $C_{\text{H}\widetilde{W}B} = 10$ or $C_{HB} = 100$ contribution to the SM, as shown in Fig. 4.3 or Fig. 4.4, with the cross section decomposition presented in Table 4.3 or Table 4.4. The size of anomalous contributions is chosen to be large compared to SM for visibility of their contributions.

In the $H \to 4\ell$ process, the larger and the smaller invariant masses of the dilepton pairs m_1 and m_2 are the two observables representing q_1^2 and q_2^2. In Fig. 4.2, there are clear peaks towards $m_2 \to 0$ in the case of couplings with photons, $HZ\gamma$ and $H\gamma\gamma$.In the case of $H\gamma\gamma$, this extends to $m_1 \to 0$ as well. Modeling such contributions becomes essential, and we will discuss extensions of such modeling to $m_{\ell\ell} < 1\,\text{GeV}$ later. Moreover, in analysis of experimental data, detector effects change significantly for either γ^* or Z intermediate states, and dedicated simulation of such effects with the full detector modeling becomes important. In Fig. 4.2, the m_1 and m_2 distributions are shown separately in the $H \to 4e/4\mu$ and $H \to 2e2\mu$ decays. The interference of two diagrams with permutation of identical leptons in the case of $H \to 4e/4\mu$ leads to suppression of the peaks at $m_1 \to 0$ and $m_2 \to 0$ in the case of $H\gamma\gamma$. This feature

becomes important in analysis of the $H\gamma\gamma$ couplings.

Since Zff couplings have been constrained with precision EW data, we do not allow their change in these studies and assume that modification of other operators, not contributing to the Higgs boson couplings, can compensate any possible shift of the Zff couplings due to $C_{\mathrm{H}WB}$. However, in Fig. 4.2 we also show distributions with modification of the Zff couplings, indicated with δg^{Zff}. Corrections to the multidimensional angular distributions are expected due to non-zero values of the R_i and A_f parameters discussed in Refs. [82, 83, 84]. These corrections are visible in the projection on the Φ observable in Fig. 4.2, but are very small for any practical purpose with the typical values of $C_{\mathrm{H}WB}$ in the present studies. These corrections become sizable with larger values of $C_{\mathrm{H}WB}$.

In the VBF process, we can calculate the $q_{1,2}^{\mathrm{VBF}} = \sqrt{-q_{1,2}^2}$ values using the momenta of the fully reconstructed Higgs boson and two jets and using the direction of incoming partons along the proton beams. In Fig. 4.3, there is a clear preference of lower $q_{1,2}^{\mathrm{VBF}}$ values in the case of couplings with photons. There is a strong correlation between the $q_{1,2}^{\mathrm{VBF}}$ values and the transverse momentum p_T of the jets, which leads to different detector effects. We note the asymmetric distribution of the Φ^{VBF} angle in Fig. 4.3, which is most visible in the HZZ process but can also be seen in the combined distribution. This happens due to interference of the CP-even SM amplitude and CP-odd $C_{\mathrm{H}\widetilde{W}B} = 10$ contributions.

In the VH process, q_1^2 and q_2^2 represent the VH and the $V \to \ell^+\ell^-$ invariant masses, respectively. There are particularly dramatic effects in the $m_{\ell\ell}$ distribution, shown in

Fig. 4.4, where the virtual photon γ^* results in the low-mass enhancement, as opposed to the peak at m_Z. A dedicated analysis of the small invariant masses in the $\gamma^* H$ production may be needed for effective EFT analysis of the process.

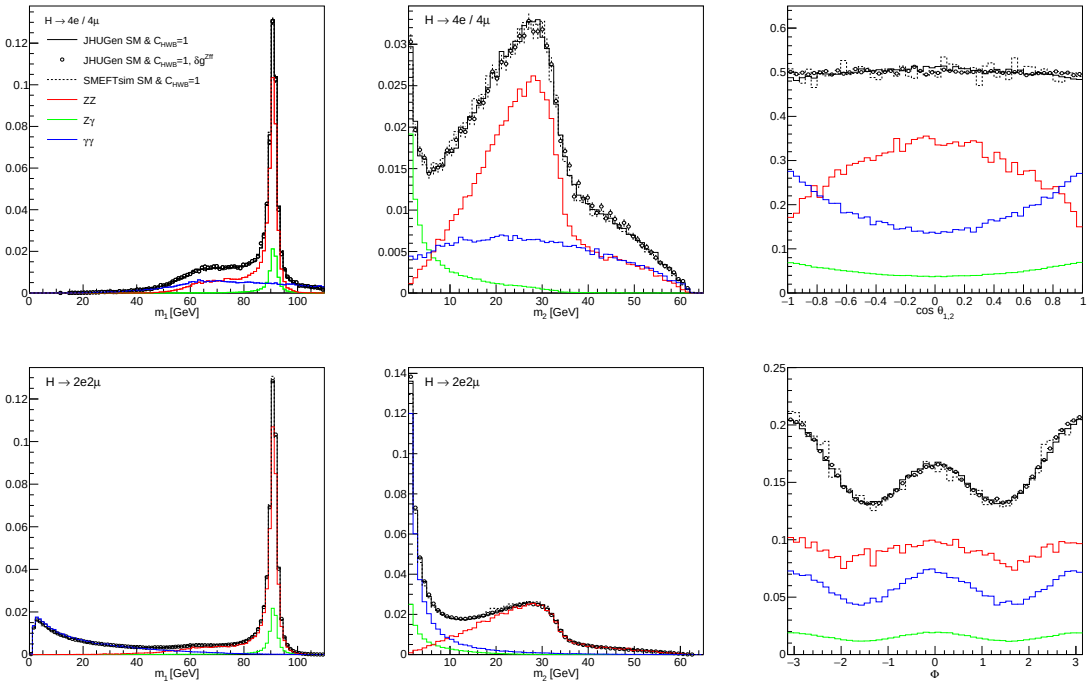

Figure 4.2: Distribution of the larger (left) and smaller (middle) dilepton invariant mass in the $H \to 4e/4\mu$ (top) and $H \to 2e2\mu$ (bottom) decay. Also shown are the $\cos\theta_{1,2}$ (top right) and Φ (bottom right) distributions in the $H \to 2e2\mu$ decay. Distributions are generated with JHUGen for $C_{HWB} = 1$, with the three contributions due to the HZZ (red), $HZ\gamma$ (green), and $H\gamma\gamma$ (blue) couplings shown separately. The JHUGen distributions are shown without (solid) and with (points) corrections to the Zff couplings, indicated with δg^{Zff}. The comparison to SMEFTsim modeling (dashed) is also shown.

4.6 Higgs production in association with a photon

Another approach to study anomalous Higgs boson couplings involving photons is analysis of the γH process, which distinguishing feature is a high-momentum on-shell

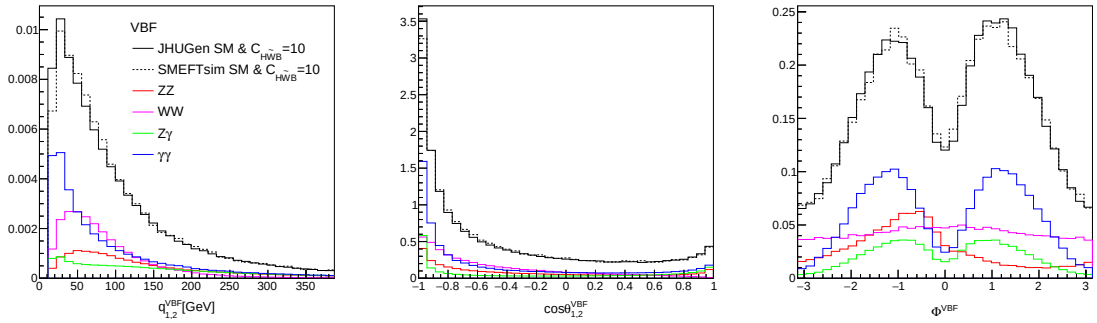

Figure 4.3: Distribution of $\sqrt{-q^2_{1,2}}$ (left), $\cos\theta^{\rm VBF}_{1,2}$ (middle), and $\Phi^{\rm VBF}$ (right) for the intermediate vector boson in the VBF process generated with JHUGEN for the $C_{\rm H\widetilde{W}B} = 10$ with three contributions due to the HZZ (red), HWW (magenta), $HZ\gamma$ (green), and $H\gamma\gamma$ (blue) couplings shown separately. The comparison to SMEFTSIM modeling (dashed) is also shown.

photon associated with the Higgs boson. In the LO topology, where the γH system has no transverse boost, the transverse momentum of either photon γ or the Higgs boson is a dependent observable and the three primary measurements are the rapidity y and the invariant mass $m_{\gamma H}$ of the $m_{\gamma H}$ system, and the angle θ_1 formed by the outgoing photon with respect to the direction of incoming quark in the γH rest frame. This angle is also defined in Fig. 5.16, where $V_2 = \gamma$ and which does not have a subsequent decay. While it is not possible to distinguish the incoming quark and antiquark on event-by-event basis, on average the boost direction of the γH provides the preferred direction of the quark, and we use this to define θ_1. However, determination of the $\cos\theta_1$ sign becomes important only in the special case of the forward-backward asymmetry discussed below. The ability to determine the $\cos\theta_1$ sign is a function of y and has been discussed earlier [121, 81].

In Fig. 4.5, the $m_{\gamma H}$ and $\cos\theta_1^{VH}$ distributions are shown for the $g_2^{Z\gamma}$, $g_2^{\gamma\gamma}$, $g_4^{Z\gamma}$, or

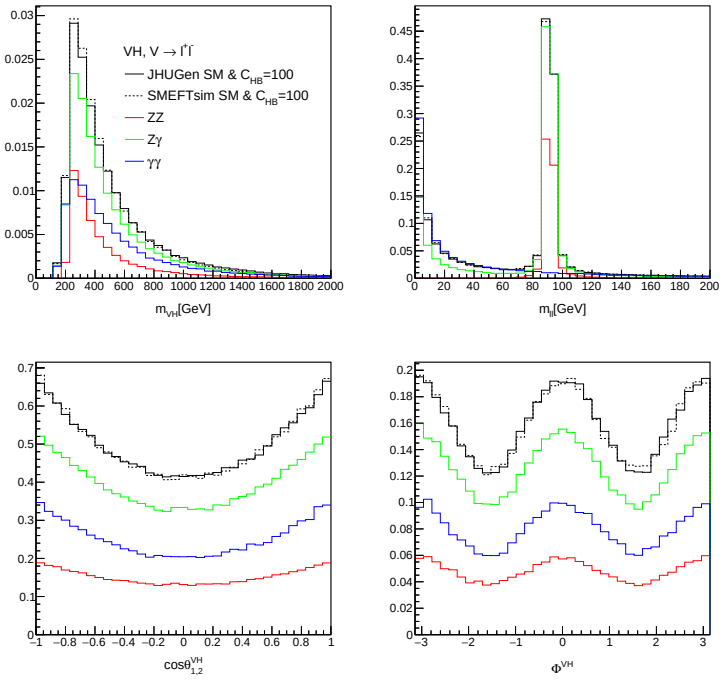

Figure 4.4: Distribution of the m_{VH} (top left) and $m_{\ell\ell}$ (top right) invariant masses, $\cos\theta_{1,2}^{VH}$ (bottom left), and Φ^{VH} (bottom right) in the $q\bar{q} \to VH \to \ell\ell H$ process generated with JHUGen for the $C_{HB} = 100$ with three contributions due to the HZZ (red), $HZ\gamma$ (green), and $H\gamma\gamma$ (blue) couplings shown separately. The comparison to SMEFTsim modeling (dashed) is also shown.

$g_4^{\gamma\gamma}$ anomalous couplings, and for the mixture of $g_2^{Z\gamma}$ and $g_4^{Z\gamma}$ contributions with a complex phase of $g_4^{Z\gamma}$. The $m_{\gamma H}$ distributions differ somewhat between the $HZ\gamma$ and $H\gamma\gamma$ couplings, due to the difference between the intermediate Z^* and γ^*. The $\cos\theta_1^{VH}$ distributions follow the $\left(1 + \cos^2\theta_1\right)$ expectation for all real couplings. This expectation can be traced back to Eq. (A2) in Ref. [84], where $A_{00} = 0$, which must be averaged over Φ and $\cos\theta_2$. The situation becomes similar to the angular distribution in the $H \to Z\gamma$ decay, described with the same angular parameterization, as shown in Fig. 15 of Ref. [84], and where the forward-backward asymmetry may be generated with the mixture of CP-odd and CP-even couplings and in the presence of a complex

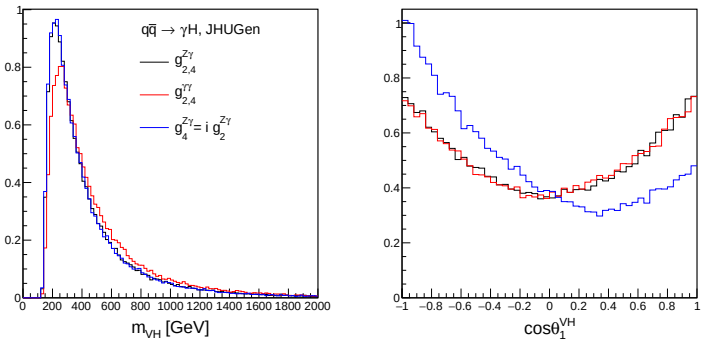

Figure 4.5: Distribution of $m_{\gamma H}$ (left) and $\cos\theta_1^{VH}$ (right) in the $q\bar{q} \to \gamma H$ process generated with JHUGen with the $g_2^{Z\gamma}$, $g_2^{\gamma\gamma}$, $g_4^{Z\gamma}$, or $g_4^{\gamma\gamma}$ anomalous couplings. Distributions for individual couplings are shown in black ($HZ\gamma$) and red ($H\gamma\gamma$), and the mixture of $g_2^{Z\gamma}$ and $g_4^{Z\gamma}$ couplings with the complex ratio is shown in blue.

phase.

The size of the forward-backward asymmetry is proportional to the A_f parameter defined in Ref. [84] for Zff couplings, which is 0.15 for the lepton couplings, but is as large as 0.67 and 0.94 for the up and down type quarks. Therefore, despite the sizable dilution in the measurement of the $\cos\theta_1$ sign, the forward-backward asymmetry is strongly pronounced in Fig. 4.5 and could be measured in experiment once γH production is observed. The A_f parameter is zero for the photon couplings γff, and such an effect is not possible in the mixture of couplings involving $g_2^{\gamma\gamma}$ and $g_4^{\gamma\gamma}$. Since non-trivial forward-backward asymmetry appears only in the special case of complex couplings, we do not consider this asymmetry further in this work, but we point out that such a study is in principle possible.

4.7 Loop-induced standard model contributions

The NLO EW corrections from the PROPHECY4F and HAWK generators have been widely used in calculations of the Higgs boson production and decay cross sections at the LHC and included in the LHC Higgs Working Group recommendations [79]. The corrections are generally positive in the $H \to 4\ell$ process [122] and negative in the VBF and VH processes [123]. Differential distributions also show growth of these effects at higher energy, such as at high transverse momentum p_T^H of the Higgs boson in the case of VBF and VH production, as expected for the well-known EW Sudakov enhancement. Our goal here is to reexamine some of these effects, focus on certain kinematic distributions, and compare the NLO EW effects to those generated by the EFT operators. In particular, we also produce kinematic distributions with JHUGEN at LO, and introduce effective $g_2^{\gamma\gamma,\mathrm{SM}}$ and $g_2^{Z\gamma,\mathrm{SM}}$ couplings to model what one can call pseudo-EW corrections. Both PROPHECY4F and HAWK include the interference of the loop-induced contributions with the Born process as dictated at NLO accuracy, but do not include squared contributions, which are formally of higher order. Nonetheless, these squared terms may be comparable to or larger than the interference contributions, and we examine this with the effective $g_2^{\gamma\gamma,\mathrm{SM}}$ and $g_2^{Z\gamma,\mathrm{SM}}$ couplings by keeping or excluding their squared contributions.

The effective point-like couplings, such as $g_2^{\mathrm{gg,SM}}$, $g_2^{\gamma\gamma,\mathrm{SM}}$, and $g_2^{Z\gamma,\mathrm{SM}}$, can model SM loop effects only in decay (or production) with on-shell particles, such as $H \to \mathrm{gg}, \gamma\gamma, Z\gamma$. The numerical values of these couplings from Eq. (4.1) can be found in Eqs. (4.15), (4.19), and (4.28), respectively. As we illustrate below, these couplings are inadequate for modeling loop effects in decays to virtual vector bosons, such as $H \to \gamma^*\gamma/Z\gamma \to$

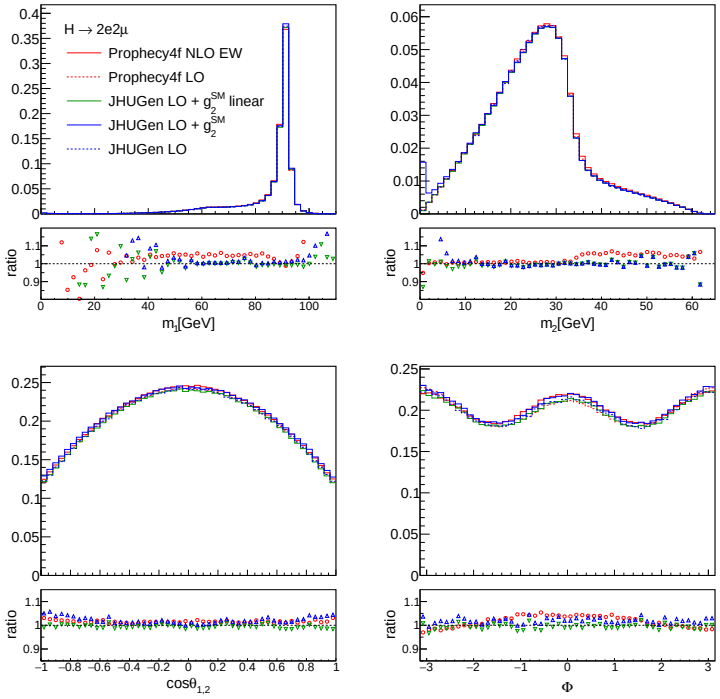

Figure 4.6: Distributions of kinematic observables in the $H \to 2e2\mu$ decay: m_1, m_2, $\cos\theta_{1,2}$, Φ. Five distributions are shown in each case: LO simulation (dashed red), NLO EW (solid red) with PROPHECY4F, LO (dashed blue) and ad-hoc loop correction with $g_2^{\gamma\gamma,\mathrm{SM}}$ and $g_2^{Z\gamma,\mathrm{SM}}$ with (solid blue) and without (solid green) quadratic terms with JHUGEN. Ratio of distributions with and without corrections are also shown.

$f\bar{f}\gamma$ or $H \to \gamma^*\gamma^*/Z\gamma^*/ZZ \to f\bar{f}f'\bar{f}'$. The non-trivial q^2 dependence of the effective HVV vertex cannot be described this way and the g_2^{ZZ} and other tensor structures appearing in Eq. (4.1) are not represented. Similar considerations apply to the VBF and VH production, and also to the γH production, as discussed in Section 4.3. To make these statements in a quantitative way, we compare a simluation of these effective couplings to a complete modeling of the NLO EW effects.

In order to model the SM loop corrections in the $H \to f\bar{f}f'\bar{f}'$ process, we employ the PROPHECY4F generator, and in VBF and ZH production we use HAWK. In both

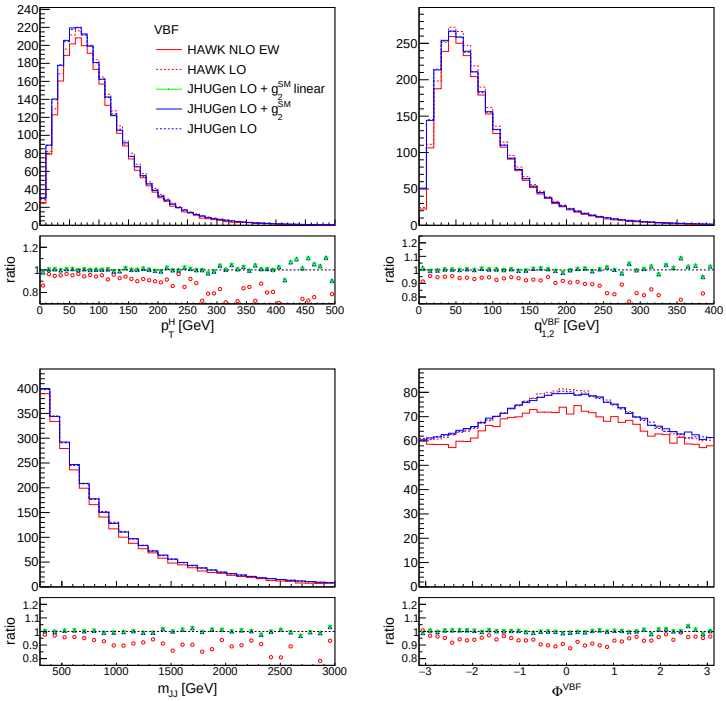

Figure 4.7: Distributions of kinematic observables in the VBF production: $p_T(H)$, $\sqrt{-q^2_{1,2}}$, m_{jj}, and Φ^{VBF}. Five distributions are shown in each case: LO simulation (dashed red), NLO EW (solid red) with HAWK, LO (dashed blue) and ad-hoc loop correction with $g_2^{\gamma\gamma,\text{SM}}$ and $g_2^{Z\gamma,\text{SM}}$ with (solid blue) and without (solid green) quadratic terms with JHUGen. Ratio of distributions with and without corrections are also shown.

cases, the NLO EW corrections can be applied to the process of interest and compared to the LO simulation. We note that HAWK provides all results in the form of binned distributions, since unweighted events are not available and events are not stored in LHE format [124]. This may complicate analysis and comparison of generated events, since different code would have to be employed in calculating the observables. Therefore, we have introduced a software interface which writes weighted events from HAWK simulation in the LHE format, and all further analysis is performed in a unified way. Moreover, photon bremsstrahlung leads to smearing of kinematic

]

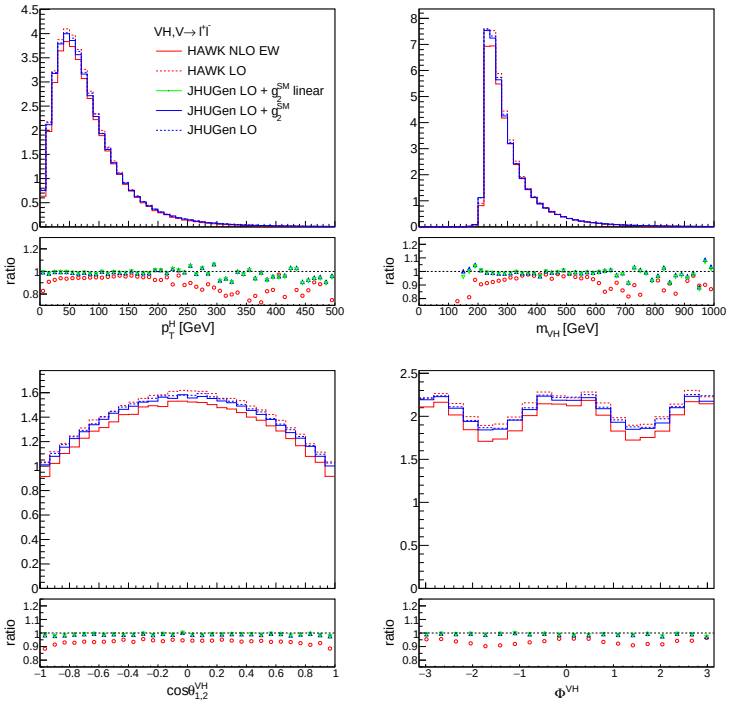

Figure 4.8: Distributions of kinematic observables in VH production: $p_T(H)$, m_{VH}, $\cos\theta_{1,2}^{VH}$, and Φ^{VH}. Five distributions are shown in each case: LO simulation (dashed red), NLO EW (solid red) with HAWK, LO (dashed blue) and ad-hoc loop correction with $g_2^{\gamma\gamma,\mathrm{SM}}$ and $g_2^{Z\gamma,\mathrm{SM}}$ with (solid blue) and without (solid green) quadratic terms with JHUGen. Ratio of distributions with and without corrections are also shown.

distributions. In order to disentangle photon radiation from purely EW effects in kinematic distributions in both the $H \to 4\ell$ and VH with $V \to \ell^+\ell^-$ processes, we have introduced a recombination algorithm in analysis of events written in LHE format. The four-momentum of the associated photon is added to the nearest lepton in this algorithm. We note that NLO QCD+EW predictions for ZH production have been recently implemented in the POWHEG framework [125], but are not included in this study.

We start with the study of NLO EW corrections in the $H \to 2e2\mu$ decay process. In Fig. 4.6, the LO and NLO EW modeling of the process is shown, as generated with the PROPHECY4F generator, and compared to ad-hoc loop correction with $g_2^{\gamma\gamma,\mathrm{SM}}$ and $g_2^{Z\gamma,\mathrm{SM}}$ with JHUGEN. The overall correction to the decay width is +1.5%, as shown in Table 4.7. The size of the effect with the pseudo-EW correction of −0.6% is similar, but does not reproduce the sign. However, including the quadratic terms with the pseudo-EW corrections appears important, as there is a growing importance of these effects at $q^2 \to 0$, which increases the correction by +2.6%. The effect of linear terms appearing with the proper NLO EW corrections is most pronounced in the intermediate m_1 and m_2 ranges, away from the pole of on-shell Z. This is where the effect of interference is most pronounced. Overall, we conclude that the pseudo-EW corrections only roughly model the effect in the $H \to 2e2\mu$ process of an order of magnitude, but are not adequate to describe the proper EW corrections. Nonetheless, they also indicate that the quadratic terms may become sizable and more important than the linear terms at the values of m_2 of a few GeV or below.

]

Table 4.7: The effect of NLO EW corrections calculated with the PROPHECY4F and HAWK programs in the three processes with the selection requirements discussed in Section 4.3. Also shown are the effects of the $g_2^{\gamma\gamma,\mathrm{SM}}$ and $g_2^{Z\gamma,\mathrm{SM}}$ couplings with and without (linear) using their squared contributions calculated with the JHUGEN program.

	EW NLO/LO	(LO + g_2^{SM})/LO	(LO + g_2^{SM} linear)/LO
$H \to 4\ell$	+1.5%	+2.0%	−0.6%
VBF	−6.7%	+0.2%	+0.1%
$Z(\to \ell^+\ell^-)H$	−6.4%	−1.2%	−1.2%

The study of NLO EW corrections in the VBF process is shown in Fig. 4.7 and in the VH process in Fig. 4.8, where the LO and NLO EW modeling of the process is shown with the HAWK generator, and compared to ad-hoc loop correction with $g_2^{\gamma\gamma,\mathrm{SM}}$ and $g_2^{Z\gamma,\mathrm{SM}}$ with JHUGen. The selection requirements are similar to those in Section 4.3, except that in VBF we do not place a requirement on q_V^2 and in VH we apply a looser requirement $m_{\ell\ell} > 0.1$ GeV and a tighter requirement $p_T^{\ell} > 5$ GeV. The overall NLO EW correction is negative in the range of $6-7\%$, as shown in Table 4.7, and grows in size with energy represented by transverse momentum p_T^H in both cases. In the case of VBF, the momentum of the intermediate vector bosons $\sqrt{-q_{1,2}^2}$ also shows this feature. The pseudo-EW corrections show about -1.2% correction in the VH process and small growth of the effect with p_T^H, but no sizable effect in the VBF process. In both VBF and VH, there is no evidence of importance of the quadratic terms with the g_2^{SM} expansion. We conclude that the pseudo-EW corrections are not adequate in the VBF and VH processes, even if in the VH process cross section modifications appear in the same direction.

Given the inadequacy of the pseudo-EW corrections, we have investigated an approximate approach of re-weighting the LO EW simulation with a dynamic k factor, which is a ratio of the NLO and LO EW kinematic distributions. This approach can capture the main features of the correction, such as its growth with p_T^H, if this quantity is used as the kinematic distribution in re-weighting. However, this approach does not guarantee adequate modeling of the other kinematic distributions simultaneously, if those are not also used in re-weighting. For example, we found that re-weighting based on p_T^H does not bring angular distributions to an agreement.

The importance of the NLO EW corrections will become evident in the actual analysis of LHC data. The precision of existing LHC constraints [59, 70, 60, 61, 62, 71, 72, 63, 64, 73, 74, 75, 65, 66, 126, 104] is not sufficient for reaching the NLO EW effects appearing in the SM. Therefore, accurate modeling of such effects may not appear as critical at present. However, with growing precision of experimental measurements a careful investigation of NLO EW effects on kinematic distributions will become important.

4.8 Spin Correlations and implications relating to Quantum Entanglement at the LHC

Here I will breifly discuss alternative interpretations of the $H \to 4\ell$ decay kinematics. This alternative interpretation has consequences for CP-violation and tests of Belles inequality at the LHC. A more detailed treatment of the formalism described in this section is presented in Section 5.6. For now I will present the formalism of polarization fractions and how they relate directly to terms of the ρ matrix.

4.8.1 Polarization density matrix

The polarizations of the Z bosons in the $H \to ZZ$ decay are closely related to the tensor structure of the HZZ interaction described in Eq. (4.1). To characterize their polarization states, we define the quantum mechanical amplitudes $A_{\lambda_1\lambda_2}$, which correspond to the spin projections λ_1 and λ_2 along the directions of Z_1 and Z_2, respectively, in the rest frame of the Higgs boson. The quantum states λ_1 and λ_2 cannot be directly measured in experiments. Instead, the amplitudes $A_{\lambda_1\lambda_2}$ can be inferred by

analyzing the angular distributions of the decay products $H \to Z_1 Z_2 \to (e^+e^-)(\mu^+\mu^-)$.

Final states with identical leptons, such as $e^+e^-e^+e^-$ and $\mu^+\mu^-\mu^+\mu^-$, introduce additional complexity due to possible permutations of identical particles, as will be discussed below. In these cases, interference between amplitudes corresponding to different lepton pairings makes the assignment of Z_1 and Z_2 ambiguous, thereby complicating the interpretation of the Z boson polarization. Nonetheless, Eq. (4.1) predicts unique angular distributions in each final state and allows us to relate the measurements in all final states [82, 83]. Therefore, while the polarization notation is defined in the $(e^+e^-)(\mu^+\mu^-)$ final state, all four-lepton final states are included in the polarization measurements.

It is convenient to express the transverse polarization amplitudes in terms of the CP-even component $A_\parallel$ and the CP-odd component $A_\perp$, and to relate these, along with the longitudinal polarization amplitude A_{00}, to Eq. (4.1) as follows [83]:

$$A_{00} = -\frac{\sqrt{1+x}\, m_H^2}{v}\, a_1(m_1, m_2) - \frac{x m_1 m_2}{v}\, a_2(m_1, m_2)\,, \tag{4.33}$$

$$A_\parallel = \frac{A_{++} + A_{--}}{\sqrt{2}} = \frac{\sqrt{2} m_H^2}{v} a_1(m_1, m_2)\,, \tag{4.34}$$

$$A_\perp = \frac{A_{++} - A_{--}}{\sqrt{2}} = i\frac{\sqrt{2x}\, m_1 m_2}{v} a_3(m_1, m_2)\,, \tag{4.35}$$

$$\text{where} \quad x = \left(\frac{m_H^2 - m_1^2 - m_2^2}{2 m_1 m_2}\right)^2 - 1\,.$$

The six remaining $A_{\lambda_1\lambda_2}$ are equal to zero due to the conservation of angular momentum in the decay of a spin-zero Higgs boson.

The determination of the amplitudes $A_{\lambda_1\lambda_2}$ has traditionally been an important aspect of studying the decay of spin-zero particles into two vector particles, for instance, in analyses of B meson decays into spin-one or tensor mesons [127, 128]. However, polarization analysis of the Higgs boson decays has attracted limited attention, primarily because the amplitudes $A_{\lambda_1\lambda_2}$ do not have fixed values: they depend on the varying masses of the off-shell Z_1 and Z_2 bosons. In the decay $H \to ZZ$, at least one of the Z bosons must be significantly off-shell, leading to considerable variation in the decay amplitudes. Nevertheless, examining the average polarization states and their interference offers valuable insight into the underlying interactions, with potential BSM effects manifesting as deviations from SM predictions.

As shown in Eqs. (4.33–4.35), each of the three amplitudes exhibits a distinct dependence on the masses, which complicates the description of the overall ZZ quantum state. The coherence between different ZZ spin polarization states is encoded in the polarization density matrix $\rho_{\lambda_1\lambda_2,\lambda_3\lambda_4}$, which is a 9×9 matrix. However, only 9 of its elements are non-zero for the spin-zero Higgs boson decay. The diagonal elements describe probabilities of the ZZ system being in each spin polarization state, while the off-diagonal elements describe quantum interference between different spin polarization states. The mass dependence is averaged over the probability density $\mathcal{P}(m_1, m_2)$ in the $H \to Z_1Z_2 \to (e^+e^-)(\mu^+\mu^-)$ decay, leading to evaluation of the polarization density

matrix as

$$\rho = \int \frac{dm_1 dm_2\, \mathcal{P}(m_1, m_2)}{|A_{++}|^2 + |A_{00}|^2 + |A_{--}|^2} \begin{pmatrix} 0 & 0 & 0 & 0 & 0 & 0 & 0 & 0 & 0 \\ 0 & 0 & 0 & 0 & 0 & 0 & 0 & 0 & 0 \\ 0 & 0 & A_{++}A_{++}^* & 0 & A_{++}A_{00}^* & 0 & A_{++}A_{--}^* & 0 & 0 \\ 0 & 0 & 0 & 0 & 0 & 0 & 0 & 0 & 0 \\ 0 & 0 & A_{00}A_{++}^* & 0 & A_{00}A_{00}^* & 0 & A_{00}A_{--}^* & 0 & 0 \\ 0 & 0 & 0 & 0 & 0 & 0 & 0 & 0 & 0 \\ 0 & 0 & A_{--}A_{++}^* & 0 & A_{--}A_{00}^* & 0 & A_{--}A_{--}^* & 0 & 0 \\ 0 & 0 & 0 & 0 & 0 & 0 & 0 & 0 & 0 \\ 0 & 0 & 0 & 0 & 0 & 0 & 0 & 0 & 0 \end{pmatrix} \tag{4.36}$$

The central element of the ρ matrix represents the average fraction of the longitudinal polarization state

$$f_L \;=\; \int dm_1 dm_2\, \mathcal{P}(m_1, m_2)\, \frac{|A_{00}|^2}{|A_{++}|^2 + |A_{--}|^2 + |A_{00}|^2}\,. \tag{4.37}$$

It is also convenient to define the average fractions of CP-odd and CP-even transverse polarization states as $f_\perp$ and $f_\parallel$, similarly to Eq. (4.37), but with $A_\perp$ and $A_\parallel$ appearing in the numerator instead of A_{00}. Given that $(f_L + f_\perp + f_\parallel) = 1$, it is sufficient to

define

$$f_\perp \;=\; \int dm_1 dm_2\, \mathcal{P}(m_1, m_2)\, \frac{|A_\perp|^2}{|A_{++}|^2 + |A_{--}|^2 + |A_{00}|^2}\,, \tag{4.38}$$

which can also be evaluated from the elements of the ρ matrix

4.8.2 Quantum entanglement at the LHC

The polarization density matrix in H $\to$ ZZ decays has recently attracted significant attention, owing to its relevance to the quantum entanglement between the spin states of the two particles, see Refs. [129, 130] and references therein. It has even been suggested that a test of locality via Bell-type inequalities or a test of entanglement versus non-entanglement could be performed in such a system. However, as is clear from the reasoning behind Eq. (5.11), which forms the basis for deriving the polarization density matrix, (Relativistic) Quantum Mechanics (QM) was assumed. The spin polarization states are not measured directly, they are inferred from the momenta of the final-state particles, which give rise to the angular distributions in Eq. (5.11). As a result, it is not possible to definitively rule out non-entanglement or test locality through a Bell-type inequality [131, 132, 133].

Nonetheless, it remains possible to test the consistency of the observed states with quantum entanglement and potential violation of the Bell-type inequality, or its extensions, providing a means to scrutinise the predictions of the SM. Entanglement is a phenomenon in which the state of one particle cannot be described independently of the state of another. It is a fundamental feature of QM. While assuming the validity of QM to test its own validity may not yield fundamentally new information, unless

violation is observed, entanglement remains a fascinating phenomenon that can be experimentally investigated.

Let us picture someone throwing two stones in opposite directions, and as they travel, each stone splits into two fragments. With four fragments in the air, we can clearly trace each one back to its original stone, an illustration of the classical physics view of the world, where objects have well-defined origins and trajectories. This is roughly analogous to the decay $H \to Z_1 Z_2 \to (e^+e^-)(\mu^+\mu^-)$, where we know that the electron pair originated from one Z_1 boson and the muon pair from the other Z_2. However, when we consider the decay $H \to Z_1 Z_2 \to (\mu_1^+\mu_2^-)(\mu_3^+\mu_4^-)$, we can no longer definitively determine which muons originated from which Z boson. The other possibility is equally plausible $H \to Z_1' Z_2' \to (\mu_1^+\mu_4^-)(\mu_3^+\mu_2^-)$. We can certainly assign labels to the muons $(1, 2, 3, 4)$, as we detect them with high precision, but we cannot unambiguously identify which pair originated from which Z boson, this ambiguity is reflected in the two possible pairings: $Z_1 Z_2$ or $Z_1' Z_2'$.

This effect is known as the permutation of identical leptons and applies to both the $H \to 4e$ and $H \to 4\mu$ decay channels. This phenomenon is a manifestation of the entanglement when the state of one Z boson cannot be described independently of the state of another. This observation stands in stark contrast to the classical example of two stones breaking into fragments, as it entirely defies the classical understanding of the world. However, we can actually demonstrate the existence of this effect using our data. While we have accounted for this effect in all results derived from the data since the observation of the Higgs boson, we have not formally shown its presence.

The permutation of identical leptons causes significant distortions in the observed distributions, such as m_1, m_2, $\cos\theta_1$, $\cos\theta_2$, and Φ. These distortions become evident when comparing the $H \to 2e2\mu$ decay to the 4e or 4μ decays, as well as in the relative event yields, which are affected by the constructive interference between the two amplitudes in the SM. In order to test the data for the presence of this entanglement effect, we can create a model alternative to the SM, where there is no permutation of identical leptons and no interference of the two amplitudes occurs. Ruling out such a model in the data would offer a clear demonstration of entanglement.

Building on the example of someone throwing two stones in opposite directions, with two other people, Alice and Bob, checking the spin of those stones, classical physics would allow the spins to be predicted in advance based on how the stones were thrown. No such prediction can be made in the $H \to Z_1Z_2 \to (e^+e^-)(\mu^+\mu^-)$ decay; the outcome is random, with only three possible quantum states. However, once the spin of one Z boson is determined, the spin of the other is known with 100% certainty. The two Z bosons are in an entangled state with respect to their spin projections. At first glance, this fact may not seem particularly fascinating, as a similar effect is also known in classical physics. Due to the conservation of angular momentum, a fundamental law following from the rotational symmetry of space, the spins of the two stones could be correlated, depending on how they were thrown. However, the combination of random spins on one hand and the correlation between the two non-locally on the other hand is something that defies the classical view, where it would be impossible for them to be both random and correlated at the same time.

However, a hidden variable theory was introduced [134, 135], which suggested that the

randomness is only apparent. It suggested there are hidden variables that predetermine the outcomes. Let us picture Alice and Bob making the spin projections measurements, each yielding three possible outcomes. If local hidden variables govern the correlations of measurements by Alice and Bob, instead of QM, there is a mathematical upper bound on a certain expression involving the joint probabilities of outcomes. The GCLMP inequality [136] - named for Gisin, Collins, Linden, Massar, and Popescu - is a generalization of Bell's inequality [137] for qubits to qutrits (and above), which sets such bounds. The ZZ state in the Higgs boson decay can violate this inequality demonstrating non-locality for entangled systems with qutrits. A quantity I_3 can be calculated as a linear combination of the polarization density matrix elements defined in Eq. (5.10) under assumption of no CP violation [129]. It has been shown that the ZZ system violates the GCLMP inequality when $I_3 > 2$.

The preceding discussion relies on a key assumption: that all three quantum states, A_{00}, A_{++}, and A_{--}, are allowed, implying that the Z bosons are entangled and behave as a qutrits with three possible spin projections. In the context of our angular analysis, it is sufficient to demonstrate that $f_L \neq 0$ and $f_L \neq 1$. Given the assumption $f_\perp = 0$, or its approximate validity, this implies that all three quantum states must be present. Although this would not constitute a definitive test distinguishing entanglement from non-entanglement, since direct measurement of the Z boson spin projections is not possible in our experiment, it would nevertheless confirm the presence of an entangled state, inferred from the angular distributions of the final-state particles, assuming the validity of QM. Similarly, we cannot directly demonstrate non-locality in our experiment, however demonstrating $I_3 > 2$ would indicate that the conditions for

observing non-locality are present. Since in the SM $f_L^{\mathrm{SM}} = 0.61$ and $I_3^{\mathrm{SM}} = 2.60$, we need to measure the consistency of our data with these values with sufficient precision to confidently establish the conditions mentioned above.

Chapter 5
Physics Analysis

In this chapter, I will detail the various experimental results that I have produced using CMS data using the four lepton final state. These results originate from two main analysis, the first of which targets the γH process, performed in combination with the boosted H $\rightarrow$ b$\bar{\text{b}}$ channel using the full Run2 dataset. This analysis placed the first constraints on the γH production cross section in the EFT framework at the LHC, and placed constraints on the light Yukawa couplings using the $H \rightarrow 4\ell$ channel only. The second analysis places constraints on anomalous couplings and polarization fractions from the decay kinematics of H $\rightarrow 4\ell$ using the complete Run2 and partial Run3 (2022+2023) datasets. These two analyses share a lot in common, including simulation tools, observables, event selection and systematic uncertainties. Due to these shared characteristics, I will first describe the main details of the analyses, and then individually describe the motivations, observations, and results of each analysis separately.

5.1 General steps of a physics analysis

5.1.1 Signal and Background Modeling

To simulate the anomalous interactions described in Eq. (4.1) in the γH production mode, and the H $\rightarrow$ ZZ, Zγ^*, and $\gamma^*\gamma^* \rightarrow 4\ell$ decay, the Monte Carlo (MC) program JHUGen 7.5.5 [82, 83, 84, 85, 138] is used. The MELA [82, 83, 84, 85, 138] package

provides a library of matrix elements, incorporating those from JHUGEN for signal processes and from MCFM [139] for background processes. It is used to apply event weights to any MC sample in order to model alternative sets of anomalous or SM couplings.

The production of the Higgs boson via gluon fusion, vector boson fusion (VBF), or in association with a Z or W boson or a $t\bar{t}$ pair is simulated using POWHEG 2 [140, 141, 142, 143, 144] at next-to-leading order (NLO) in QCD, with decays handled by JHUGEN. These simulated samples are subsequently reweighted to represent any desired coupling hypothesis in decay using MELA.

The main background in this analysis, $q\bar{q} \to ZZ/Z\gamma^* \to 4\ell$, is estimated from simulation with POWHEG. A fully differential cross-section has been computed at NNLO in QCD [145], but it is not yet available in a partonic level event generator. Therefore, the NNLO/NLO QCD correction is applied as a function of $m_{4\ell}$. Additional NLO EW corrections are also applied to this background process in the region $m_{4\ell} > 2m_Z$ [146, 147]. The $gg \to ZZ/Z\gamma^* \to 4\ell$ background process is simulated with MCFM 7.0.1 [139, 93, 94, 95]. The small remaining electroweak (EW) background, including processes such as VVV and $t\bar{t}V$, is modeled using MG5_aMC@NLO [116, 148].

The parton distribution functions (PDFs) used in this paper belong to the NNPDF 3.1 PDF sets [149]. All MC samples are interfaced to PYTHIA 8 [150] for parton showering, using version 8.306 for the Run2 data period. Simulated events include the contribution from additional pp interactions within the same or adjacent bunch crossings (pileup),

and are weighted to reproduce the observed pileup distribution. The MC samples are further processed through a dedicated simulation of the CMS detector based on GEANT4 [151].

An additional background to the Higgs boson signal, referred to as Z+X, arises from Z+jets events where jets are misidentified as leptons, including those from heavy-flavor hadron decays and in-flight meson decays. This contribution is estimated using control regions in data, defined by events with a Z_1 candidate and two extra opposite-sign leptons passing looser identification criteria. These events must also satisfy the ZZ candidate selection. The expected yield in the signal region is obtained by weighting these events with the lepton misidentification probability, the rate at which non-prompt leptons pass the analysis selection. Further details are provided in Ref. [152].

5.1.2 Event reconstruction and candidate selection

The selection of 4ℓ events and associated particles closely follows the methods used in the analyses of the Run 1 [60, 61] and Run 2 [152, 64, 65, 153] data sets. The main triggers for the Run 2 analysis select either a pair of electrons or muons, or an electron and a muon. The minimal transverse momentum of the leading electron (muon) is 23 (17) GeV, while that of the subleading lepton is 12 (8) GeV. To maximize the signal acceptance, triggers requiring three leptons with lower p_T thresholds and no isolation requirement are also used, as are isolated single-electron and single-muon triggers with thresholds of 27 and 22 GeV in 2016, or 35 and 27 GeV in 2017, respectively. The overall trigger efficiency for simulated signal events that pass the full selection chain of this analysis is larger than 99%.

Event reconstruction is based on the particle-flow (PF) algorithm [41], which exploits information from all the CMS subdetectors to identify and reconstruct individual particles in the event. The PF candidates are classified as charged hadrons, neutral hadrons, photons, electrons, or muons, and they are then used to build higher-level objects such as jets and lepton isolation quantities. Electrons (muons) are reconstructed within the geometrical acceptance defined by a requirement on the pseudorapidity $|\eta| < 2.5\,(2.4)$ for transverse momentum $p_{\mathrm{T}} > 7\,(5)\,\mathrm{GeV}$ with an algorithm that combines information from the ECAL (muon system) and the tracker. A dedicated algorithm is used to collect the final-state radiation (FSR) of leptons [152].

The reconstructed vertex with the largest value of summed physics-object p_{T}^2 is taken to be the primary pp interaction vertex. The physics objects are the jets and the associated missing transverse momentum, taken as the negative vector sum of the p_{T} of those jets. The jets are clustered using the anti-k_{T} jet finding algorithm [42, 43] with a distance parameter of 0.4 and the associated tracks assigned to the vertex as inputs. Jets must satisfy $p_{\mathrm{T}} > 30\,\mathrm{GeV}$ and $|\eta| < 4.7$ and must be separated from all selected lepton candidates and any selected FSR photons with a requirement on the distance parameter $\Delta R(\ell/\gamma, \mathrm{jet}) > 0.4$, where $(\Delta R)^2 = (\Delta\phi)^2 + (\Delta\eta)^2$.

In order to ensure that the leptons are all consistent with a common primary vertex, each lepton track is required to have the ratio of the impact parameter in three dimensions, which is computed with respect to the chosen primary vertex position, and its associated uncertainty to be less than 4. This significance of the impact parameter (SIP) is defined as $\mathrm{SIP} = \frac{\mathrm{IP}}{\sigma_{\mathrm{IP}}}$ where IP is the lepton impact parameter and σ_{IP} is the associated uncertainty. The requirement for a primary lepton is then

$|\mathrm{SIP}| < 4$.

To discriminate between leptons from prompt Z boson decays and those arising from hadron decays within jets, an isolation requirement for leptons is imposed in the analysis of the data [152]. Electrons are identified and isolated utilizing a Boosted Decision Tree algorithm implemented with the eXtreme Gradient Boosting (XGBoost) optimized distributed gradient boosting library, trained on Drell-Yan with jets MC samples. This library implements machine learning algorithms and exploits observables from the electromagnetic cluster, the matching between the cluster and the electron track, observables based exclusively on tracking measurements as well as particle flow isolation sums.

We consider three mutually exclusive channels: H $\to$ 4e, 4μ, and 2e2μ. At least two leptons are required to have $p_{\mathrm{T}} > 10\,\mathrm{GeV}$, and at least one is required to have $p_{\mathrm{T}} > 20\,\mathrm{GeV}$. All four pairs of oppositely charged leptons that can be built with the four leptons are required to satisfy $m_{\ell^+\ell'^-} > 4\,\mathrm{GeV}$ regardless of lepton flavor. The

Table 5.1: The observed event yields within the mass range $105 < m_{4\ell} < 140$ GeV, along with the expected signal and background (bkg) yields, are presented for each of the three individual final states and their combination in the H $\to 4\ell$ analysis.

Production mode	2e2μ	4e	4μ	Total
Signal expected	159.3	59.6	133.0	351.9
$q\bar{q} \to 4\ell$ bkg	144.5	47.3	133.8	325.6
gg $\to 4\ell$ bkg	11.9	6.0	14.6	32.5
EW bkg	5.8	2.1	3.3	11.2
Z+X bkg	70.4	16.3	61.3	148.0
Total expected	391.9	131.3	346.0	869.2
Total observed	423	141	333	897

Z candidates are required to satisfy the condition $12 < m_{\ell^+\ell^-} < 120\,\text{GeV}$, where the invariant mass of at least one of the Z candidates must be larger than 40 GeV. The region between 105 and 140 GeV in the four-lepton invariant mass $m_{4\ell}$ is considered in this analysis. The expected signal and background yields are presented in Table 5.1.

5.1.3 Kinematic Discriminants

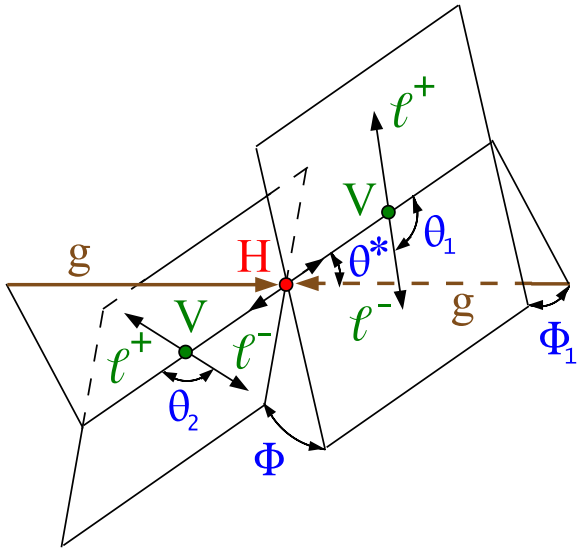

Figure 5.1: The diagram depicting the decay of the Higgs boson $gg \to H \to VV \to 4\ell$. The incoming particles are represented in brown, the intermediate vector bosons and their fermion decay products in green, the Higgs boson in red, and the angles in blue. The angles are defined in the respective rest frames of the particles [82, 83].

With the eight observables, $\vec{x}$, sensitive to both the Higgs boson anomalous interactions and signal-to-background discrimination, performing an optimal analysis in this multidimensional observable space is challenging. This difficulty is especially pronounced in the EFT analysis, where both mass and angular information need to be preserved. The MELA approach is designed to reduce the number of observables to the minimum while retaining all essential information. Two types of discriminants

were defined for the decay and production processes. Conversely, in the polarization analysis, only angular information is used directly, along with a single observable optimized for signal-to-background separation, as discussed below.

The kinematic information optimal for a given analysis can be extracted using discriminants derived from matrix element calculations. These discriminants employ a complete set of mass and angular observables, $\vec{x}$ [82, 84, 85], to describe the leading-order kinematic distributions. In this study, the kinematic discriminants are computed using the MELA package. The signal includes the four-lepton decay kinematic distributions in the processes $H \to ZZ$, $Z\gamma^*$, and $\gamma^*\gamma^* \to 4\ell$. The irreducible background includes $q\bar{q}$ and $gg \to ZZ$, $Z\gamma^*$, $\gamma^*\gamma^*$ processes, for which matrix elements are also utilized.

Two types of discriminants are defined:

$$\mathcal{D}_{\text{alt}}(\vec{x}) = \frac{\mathcal{P}_{\text{sig}}(\vec{x})}{\mathcal{P}_{\text{sig}}(\vec{x}) + c_{\text{alt}} \cdot \mathcal{P}_{\text{alt}}(\vec{x})} \tag{5.1}$$

$$\mathcal{D}_{\text{int}}(\vec{x}) = \frac{\mathcal{P}_{\text{int}}(\vec{x})}{\mathcal{P}_{\text{sig}}(\vec{x}) + c_{\text{int}} \cdot \mathcal{P}_{\text{alt}}(\vec{x})} \tag{5.2}$$

where the probability of a certain process $\mathcal{P}$ is calculated using the full kinematics characterized by $\vec{x}$ for the processes denoted as "sig" for a signal model and "alt" for an alternative model, which could be an alternative Higgs boson coupling model, to differentiate models, or background, to isolate signal. The "int" label represents the interference between the two model contributions. The probabilities $\mathcal{P}$ are calculated from the matrix elements provided by the MELA package and are normalized to give

the same integrated cross sections in the relevant phase space of each process.

By setting $c_{\text{alt}} = 1$ in Eq. (5.1), the normalization produces a balanced event distribution for the $\mathcal{D}_{\text{alt}}$ discriminants within the range from 0 to 1. Setting $c_{\text{int}} = 1$ in Eq. (5.2) yields optimal performance of the $\mathcal{D}_{\text{int}}$ discriminant in the regime of small couplings within the EFT framework. While this discriminant is unbounded and cannot be normalized, using variable-width binning effectively mitigates any related issues.

A common observable used across all analyses in this paper is $\mathcal{D}_{\text{bkg}}$, which is computed using Eq. (5.1) based on all eight observables discussed above. It is designed to distinguish the signal from the dominant four-lepton background. The alternative probability density, $\mathcal{P}_{\text{alt}}$, corresponds to the $q\bar{q} \to 4\ell$ background process. Both signal and background probabilities combine the matrix element likelihoods from MELA, derived from the four-lepton kinematic information, with the empirical $m_{4\ell}$ probability density illustrated in Fig. 5.18, which accounts for detector effects and is obtained from simulation. Distributions of $\mathcal{D}_{\text{bkg}}$ are shown in Fig. 5.2.

5.1.4 Statistical Analysis

We perform an extended maximum likelihood fit [154] in which the probability density is normalized to the total event yield in each category k (which reflects either the final state lepton flavors, or data-taking period) as a sum over all background processes i according to

$$\mathcal{P}_k(\vec{x}) = \mu_{\text{sig}} \mathcal{P}_k^{\text{sig}}\left(\vec{x}; \vec{\xi}_k, \vec{f}\right) + \sum_i \mathcal{P}_{ik}^{\text{bkg}}\left(\vec{x}; \vec{\xi}_{ik}\right), \tag{5.3}$$

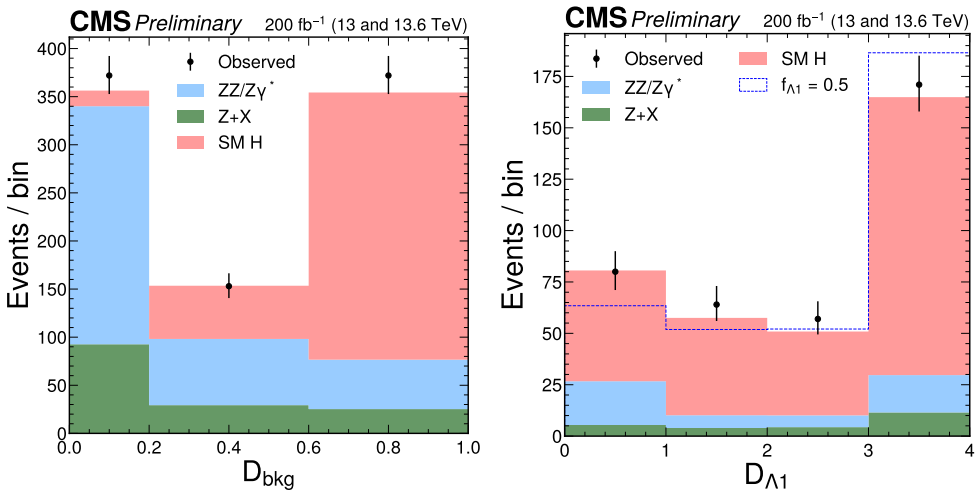

Figure 5.2: Distributions of $\mathcal{D}_{\text{bkg}}$ (left) and $\mathcal{D}_{\Lambda 1}$ (right), following the notation used in Fig. 5.18. Alternative EFT hypothesis is shown for $\mathcal{D}_{\Lambda 1}$, following the notation used in Fig. 5.11.

where μ_{sig} is the ratio of the observed cross section to the SM expectation for signal, $\vec{f}$ is the set of unconstrained parameters describing kinematic distributions in the signal process, and $\vec{\xi}_{ik}$ are the constrained nuisance parameters reflecting the uncertainties in the above parameterization.

The background processes i in Eq. (5.3) include the $q\bar{q} \to 4\ell$, $gg \to 4\ell$, EW, and Z+X processes. The first three backgrounds are estimated with simulation, but receive additional constraints from sidebands in data. The EW background includes vector boson scattering and VVV processes, which are the background counterparts of the VBF and VH processes. We also include the $t\bar{t}VV$ and $t\bar{t}V$ processes in this background contribution. Interference of the signal and background processes is negligible in the analysis of the on-shell Higgs boson production. The Z+X background contribution models Z+jets and other related processes with lepton misidentification and is estimated from the control regions in the data.

The signal and background probability distributions $\mathcal{P}_k^{\text{sig}}$ and $\mathcal{P}_{ik}^{\text{bkg}}$ appearing in Eq. (5.3) are binned multidimensional histograms (templates) of observables. The binning of these templates has been optimized for memory and speed of computer calculations, expected population of events across those bins, and retaining kinematic information. In all cases, we have one discriminant for background suppression $\mathcal{D}_{\text{bkg}}$.

The $\mathcal{P}_k^{\text{sig}}$ and $\mathcal{P}_{ik}^{\text{bkg}}$ probabilities depend on the parameters $\vec{\xi}_{jk}$ and $\vec{f}$ and are therefore interpolated between various templates as a function of these parameters. The $\vec{\xi}_{jk}$ reflect systematic uncertainties either in the normalization or shape of both signal and background templates and an analytical linear interpolation is adopted. The $\vec{f}$ parameters require nontrivial analytical interpolation of the signal templates, which is discussed in more detail below.

The final constraints on parameters μ_{sig} and $\vec{f}$ are placed using the profile likelihood method implemented in the CMS Combine tool [155] within the RooFit [156] and the ROOT [157] framework. The extended likelihood function is constructed using the probability densities in Eq. (5.3), with each event characterized by the discrete category k and observables $\vec{x}$. The likelihood $\mathcal{L}$ is maximized with respect to the nuisance parameters $\vec{\xi}_k$ describing the systematic uncertainties discussed below, and μ_{sig} and $\vec{f}$ parameters of interest. The allowed 68 and 95% confidence level (CL) intervals are defined using the profile likelihood function in the asymptotic approximation, $-2\Delta \ln \mathcal{L} = 1.00$ and 3.84 for one-dimensional likelihood scans, while for two-dimensional scans they correspond to $-2\Delta \ln \mathcal{L} = 2.30$ and 5.99, respectively, for which exact coverage is expected in the asymptotic limit [158].

5.1.5 Systematic Uncertainties

The results are limited by the statistical uncertainties. The impact of each systematic uncertainty, experimental or theoretical, on the final signal strength is less than 5%, and propagate similarly to spin correlation results. Systematic uncertainties that affect the shapes and the yields of the signals and backgrounds are incorporated in the likelihood as nuisance parameters.

Theoretical uncertainties arise primarily from the QCD renormalization and factorization scales used in the cross-section calculations. Additional contributions include uncertainties from electroweak (EW) corrections, PDFs, and parton shower modeling. QCD scale and PDF uncertainties are applied to the MC simulations, while EW uncertainties are specifically applied to the $q\bar{q} \to 4\ell$ background process. Theoretical sources are the leading systematic uncertainties affecting the signal strength. However, these uncertainties tend to cancel out in ratios used for polarization and EFT fractional measurements.

A systematic uncertainty of 1.6% (1.4%) is assigned to the integrated luminosity measurement in Run 2 (Run 3), as determined by the CMS luminosity calibration. Uncertainties in the lepton energy scale and resolution primarily impact the $m_{4\ell}$ resolution, which in turn affects the parameterization of $\mathcal{D}_{\text{bkg}}$. In estimating the $\text{Z} + \text{X}$ background, the composition of reducible background processes generally differs between the signal region and the control region. This difference in composition is the primary source of uncertainty in the $\text{Z} + \text{X}$ background estimation. Combined with the statistical uncertainty in the $\text{Z} + 2\ell$ control region, the total uncertainty leads to an approximate $\pm 30\%$ variation in the $\text{Z} + \text{X}$ background prediction. The $\text{Z} + \text{X}$

background uncertainty tends to be the dominant uncertainty for polarization and EFT fractional measurements.

5.2 γH cross section measurement

The HVV coupling measurements at the LHC have been performed using vector boson fusion (VBF), ZH, and WH production, and H $\rightarrow$ VV decays [59, 60, 61, 62, 63, 64, 65, 66, 67, 68, 69, 70, 71, 72, 73, 74, 75, 76, 77, 77, 78, 159]. However, the production of γH with an energetic photon recoiling against the Higgs boson, similar to ZH production as shown in Fig. 5.3 (left), has not been directly studied at the LHC. A recent search for WWγ production [160] was interpreted as a search for γH, where a relatively soft photon is produced as a radiative correction to quark-antiquark annihilation $q\bar{q} \rightarrow$ H, as shown in Fig. 5.3 (right). Searches for heavy resonances decaying into a photon and a hadronically decaying Higgs boson have been performed at the LHC [161, 162, 163]. Although the final state topology in these searches is similar to the processes of interest here, a direct interpretation in the EFT framework is not possible because the γH final state is modelled by the decay of a heavy spin-1 resonance.

The SM cross section of the associated photon and Higgs boson production, $\sigma_{\gamma\mathrm{H}}$, is expected to be less than 5fb at the LHC [164] and is beyond the current experimental reach. However, new anomalous interactions may enhance such production, as discussed in Refs. [109, 110, 138]. The main production mechanisms are shown in Fig. 5.3 and the corresponding transverse momentum (p_{T}) spectra of the associated photons are shown in Fig. 5.4 [138, 115, 165, 166]. The latter are important for assessing the

feasibility of detecting such final states.

The primary production mechanism targeted in this analysis is generated by the effective HZγ and H$\gamma\gamma$ vertices, as shown in Fig. 5.3 (left). The hard p_{T} spectrum resulting from anomalous H$\gamma\gamma$ or HZγ interactions makes it possible to distinguish such final states. These interactions could be generated by heavy particles in the loops leading to both *CP*-even and *CP*-odd EFT operators, with Wilson coefficients $c_{\gamma\gamma}$, $c_{z\gamma}$, $\widetilde{c}_{\gamma\gamma}$, and $\widetilde{c}_{z\gamma}$ when expressed in the mass-eigenstate basis [79]. Each of these operators can be represented as a combination of three operators in the weak-eigenstate basis [79]. Overall, there are six operators to consider in the weak-eigenstate basis, with the Wilson coefficients $C^{\varphi W}$, $C^{\varphi \mathrm{B}}$, $C^{\varphi \mathrm{WB}}$, $C^{\varphi \widetilde{\mathrm{W}}}$, $C^{\varphi \widetilde{\mathrm{B}}}$, and $C^{\varphi \widetilde{\mathrm{WB}}}$. Because of the smaller number of operators, the mass-eigenstate basis is chosen for this result, which can then be translated into the weak-eigenstate basis. In this case, the photon p_{T} distribution peaks above 50 GeV and extends up to several hundred GeV, as shown in Fig. 5.4 [138].

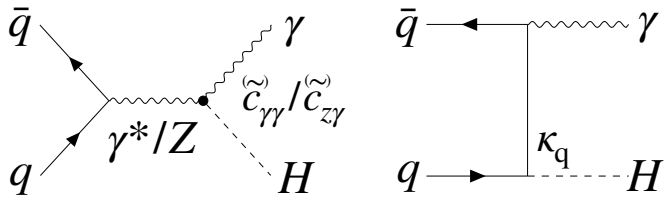

Figure 5.3: Examples of Feynman diagrams describing γH production at the LHC via a loop-generated H$\gamma\gamma$ or HZγ interaction (left), with the dot representing an effective point-like coupling, and through *Higgsboson* production in $q\bar{q}$ annihilation with photon radiation (right). The diagrams highlight the couplings of interest.

The qqHγ point interaction, shown in Fig. 5.5 (left), with the linear combination of Wilson coefficients C^{qB} and C^{qW}, equivalent to one coefficient $c_{\mathrm{q}\gamma}$ in the mass

eigenstate notation, can generate γH production in $q\bar{q}$ annihilation with a photon p_{T} spectrum even harder than that produced by anomalous HVγ couplings, as shown in Fig. 5.4 [115, 165, 166]. The point interaction appears in the Feynman rules of SMEFT [90]. However, the same beyond-the-SM (BSM) operators also contribute to the $q\bar{q}\gamma$ interaction, shown in Fig. 5.5 (right), and $q\bar{q}$Z interaction in the Feynman rules [90]. These operators are expected to be much better constrained by the more abundant processes without the presence of the *Higgsboson*, such as Drell–Yan. Although a fully optimized analysis of the Drell–Yan process to target various Wilson coefficients has not yet been performed at the LHC, current theoretical interpretations of published pp $\rightarrow \ell\nu$ and pp $\rightarrow \ell\ell$ results at the LHC indicate that the current constraints on the C^{qB} and C^{qW} Wilson coefficients from Drell–Yan are significantly stronger than those from processes involving the Higgs boson [167]. For these reasons, we do not consider this production diagram in this analysis.

5.2.1 Event Categorization

Two mutually exclusive selection requirements are used in the H $\rightarrow 4\ell$ and $\mathrm{b\bar{b}}$ channels. In both channels, two categories of events are selected. In one case, an Higgs boson candidate is selected to be associated with a high-energy photon, and the category is called γ-tagged. The other selected events are assigned to the Untagged category.

The γ-tagged category requires the presence of a photon passing loose cut-based identification requirements [168] and $p_{\mathrm{T}} > 150\,\mathrm{GeV}$. All 4ℓ events that pass the selection requirements but do not include a photon that passes the requirements for the γ-tagged category enter the Untagged category. We consider three mutually

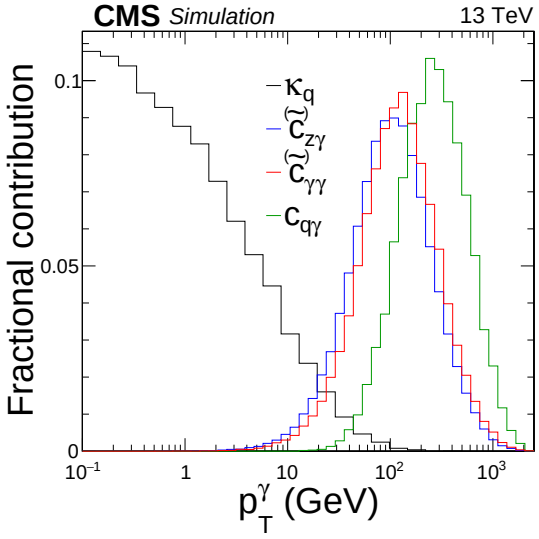

Figure 5.4: The spectrum of the photon transverse momentum in γH production, as generated by the leading-order diagrams shown in Figs. 5.3 and 5.5. The four distributions correspond to production resulting from couplings κ_q, $c_{z\gamma}$ ($\tilde{c}_{z\gamma}$), $c_{\gamma\gamma}$ ($\tilde{c}_{\gamma\gamma}$), and $c_{q\gamma}$.

exclusive channels: H $\to$ 4e, 4μ, and 2e2μ. At least two leptons are required to have $p_T > 10\,\text{GeV}$, and at least one is required to have $p_T > 20\,\text{GeV}$. All four pairs of oppositely charged leptons that can be built with the four leptons are required to satisfy $m_{\ell^+\ell^-} > 4\,\text{GeV}$ regardless of lepton flavor. The Z boson candidates are required to satisfy the condition $12 < m_{\ell^+\ell^-} < 120\,\text{GeV}$, where the invariant mass of at least one of the Z boson candidates must be larger than 40 GeV. The region between 105 and 140 GeV in the four-lepton invariant mass $m_{4\ell}$ is considered in this analysis.

5.2.2 Observables

Each event in the H $\to 4\ell$ channel is characterized by an optimal discriminant to separate signal from background $\mathcal{D}_{\text{bkg}}$ separated into 10 equal sized bins. The

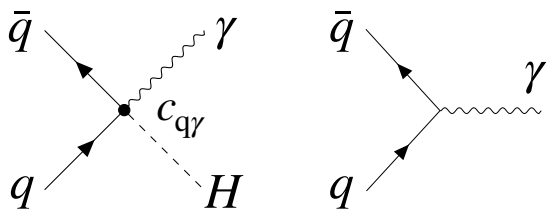

Figure 5.5: Feynman diagrams describing the $q\bar{q}$ annihilation with production of γH through a point-like EFT operator (left) and with photon production (right).

distributions of the $\mathcal{D}_{\text{bkg}}$ discriminant in the two categories of events are shown in Fig. 5.6.

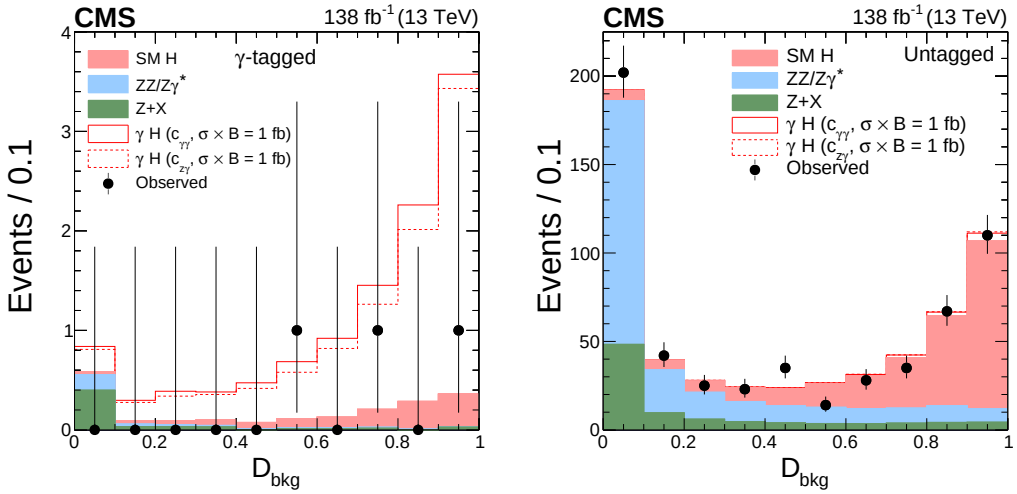

Figure 5.6: Distributions of events for the $\mathcal{D}_{\text{bkg}}$ observable in the γ-tagged (left) and Untagged (right) categories of the H $\to 4\ell$ candidate events. Observed events (black markers) and expected background estimates (solid histograms) from MC simulation (ZZ/Zγ^*) or control samples in data (Z + X) are shown. The γH signal contribution, stacked on top of background, is shown with an open histogram for an assumed cross section of $\sigma_{\gamma\text{H}}\,\mathcal{B}_{4\ell} = 1fb$ for either the $c_{\gamma\gamma}$ (solid) and $c_{z\gamma}$ (dashed) coupling hypothesis.

5.2.3 Statisitcal Analysis

The cross section of the γH process, $\sigma_{\gamma\mathrm{H}}$, is constrained in the $\mathrm{H} \to \mathrm{b\bar{b}}$ and 4ℓ channels. In both cases, a joint fit of the γH-tagged events and Untagged events is performed. The distribution of the $\mathcal{D}_{\mathrm{bkg}}$ observable in the 4ℓ channel is shown in Fig. 5.6. No significant excess of γH events is visible in either channel.

The extended likelihood function is constructed using the probability densities describing the signal and background events as functions of the M_{PNet} and $\mathcal{D}_{\mathrm{bkg}}$ observables in the $\mathrm{H} \to \mathrm{b\bar{b}}$ and 4ℓ channels, respectively. Simulation or control samples in data estimation are used to describe probability densities. The $\sigma_{\gamma\mathrm{H}}$ is parameterized as a function of the couplings $c_{\gamma\gamma}$, $c_{z\gamma}$, $\tilde{c}_{\gamma\gamma}$, and $\tilde{c}_{z\gamma}$ [138], where the total width Γ_{H} of the Higgs boson is assumed to have the SM value. It has been checked that Γ_{H} does not change significantly with variation of c_i within constraints obtained in this analysis, nor do kinematic distributions in the $\mathrm{H} \to 4\ell$ decay, which can be assumed to be dominated by the SM tree-level coupling.

The likelihood $\mathcal{L}$ is maximized with respect to the nuisance parameters, describing the systematic uncertainties, and the parameters of interest. There are four parameters of interest, which can either be the four anomalous couplings $c_{\gamma\gamma}$, $c_{z\gamma}$, $\tilde{c}_{\gamma\gamma}$, and $\tilde{c}_{z\gamma}$, or the cross-section $\sigma_{\gamma\mathrm{H}}$ and three of the anomalous couplings, with the option to eliminate one of the couplings of choice. Likelihood maximization is done using the Higgs Combine tool [155]. The allowed 68 and 95% confidence level (CL) intervals are defined using the profile likelihood function, $-2\Delta\mathcal{L} = 1.00$ and 3.84, for which exact coverage is expected in the asymptotic limit [169]. The 95% CL upper limits on $\sigma_{\gamma\mathrm{H}}$ are determined with the requirement that cross sections must be positive. They

are calculated using the CL_s criterion [170, 171] with the modified profiled likelihood ratio [169] as the test statistics.

5.2.4 Results γH cross section

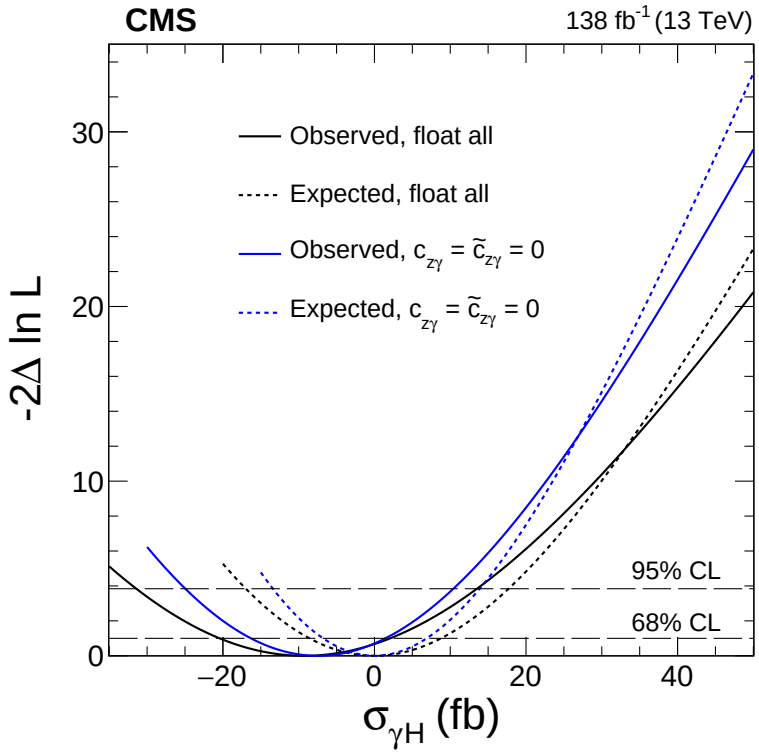

Figure 5.7: Constraints on $\sigma_{\gamma H}$ from the combination of the $H \to b\bar{b}$ and 4ℓ channels. The results are shown with only $c_{\gamma\gamma}$ and $\tilde{c}_{\gamma\gamma}$ floating in the fit (blue) and with all four couplings allowed to float (black). Observed (solid) and expected (dashed) likelihood scans are shown. The dashed horizontal lines show the 68 and 95% CL intervals.

Figure 5.7 shows the one-dimensional likelihood scan on $\sigma_{\gamma H}$ using the combination of the $H \to b\bar{b}$ and 4ℓ channels. Due to the much larger branching fraction of the $H \to b\bar{b}$ channel, the combined results are dominated by these decays. Table 5.2 shows a summary of the 68 and 95% CL intervals on $\sigma_{\gamma H}$, either with no constraints on the couplings or allowing only the $c_{\gamma\gamma}$ and $\tilde{c}_{\gamma\gamma}$ couplings. The results for the $H \to 4\ell$

Table 5.2: Observed and expected constraints on the γH cross section $\sigma_{\gamma H}$ and on the $c_{\gamma\gamma}$, $c_{z\gamma}$, $\widetilde{c}_{\gamma\gamma}$, and $\widetilde{c}_{z\gamma}$ couplings using the $H \to b\overline{b}$ and 4ℓ channels combined. The third and fourth rows show constraints on cross section multiplied by the branching fraction using the $H \to b\overline{b}$ and $H \to 4\ell$ channels only, respectively. The 68% (central value with uncertainties) and 95% (upper limit or allowed intervals) CL intervals are shown.

Parameter	Scenario	Observed		Expected	
		68% CL	95% CL	68% CL	95% CL
$\sigma_{\gamma H}$ (fb)	$c_{z\gamma} = \widetilde{c}_{z\gamma} = 0$	$-7.5^{+8.9}_{-8.8}$	<11.8	$0.0^{+6.3}_{-6.3}$	<16.1
$\sigma_{\gamma H}$ (fb)	float all	$-9.3^{+11.3}_{-11.2}$	<16.4	$0.0^{+8.0}_{-8.0}$	<21.5
$\sigma_{\gamma H}\,\mathcal{B}_{b\overline{b}}$ (fb)	float all	$-5.4^{+6.5}_{-6.5}$	<9.5	$0.0^{+4.6}_{-4.6}$	<12.4
$\sigma_{\gamma H}\,\mathcal{B}_{4\ell}$ (fb)	float all	$0.09^{+0.32}_{-0.10}$	<0.52	$0.00^{+0.18}_{-0.00}$	<0.38
$c_{\gamma\gamma}$	float all	0.00 ± 0.50	$[-0.84, 0.84]$	0.00 ± 0.63	$[-0.90, 0.90]$
$c_{\gamma\gamma}$	fix others	0.00 ± 0.46	$[-0.77, 0.77]$	0.00 ± 0.58	$[-0.83, 0.83]$
$c_{z\gamma}$	float all	0.00 ± 0.18	$[-0.30, 0.30]$	0.00 ± 0.22	$[-0.32, 0.32]$
$c_{z\gamma}$	fix others	0.00 ± 0.16	$[-0.27, 0.27]$	0.00 ± 0.21	$[-0.29, 0.29]$
$\widetilde{c}_{\gamma\gamma}$	float all	0.00 ± 0.50	$[-0.84, 0.84]$	0.00 ± 0.63	$[-0.90, 0.90]$
$\widetilde{c}_{\gamma\gamma}$	fix others	0.00 ± 0.46	$[-0.77, 0.77]$	0.00 ± 0.58	$[-0.83, 0.83]$
$\widetilde{c}_{z\gamma}$	float all	0.00 ± 0.18	$[-0.30, 0.30]$	0.00 ± 0.22	$[-0.32, 0.32]$
$\widetilde{c}_{z\gamma}$	fix others	0.00 ± 0.16	$[-0.27, 0.27]$	0.00 ± 0.21	$[-0.29, 0.29]$

and $H \to b\overline{b}$ channels are presented separately with the cross section multiplied by the respective branching fraction. This highlights that, when the branching fraction is considered, the $H \to 4\ell$ channel is not competitive with the $H \to b\overline{b}$ channel. Negative

cross sections are allowed, as indicated by the central values and 68% uncertainty ranges, except when setting the 95% CL upper limits on $\sigma_{\gamma H}$. In Fig. 5.7, the likelihood scan terminates for certain negative values of $\sigma_{\gamma H}$. This represents the case where some bins in the observables yield a negative number of events, so the total probability density function becomes negative for this extreme case.

Figure 5.8 shows the constraints on the squared couplings $c^2_{\gamma\gamma}$, $c^2_{z\gamma}$, $\tilde{c}^{\,2}_{\gamma\gamma}$, and $\tilde{c}^{\,2}_{z\gamma}$. Due to symmetry between the *CP*-even ($c^2_{\gamma\gamma}$ or $c^2_{z\gamma}$) and *CP*-odd ($\tilde{c}^{\,2}_{\gamma\gamma}$ or $\tilde{c}^{\,2}_{z\gamma}$) couplings, the likelihood scans projected on one dimension are indistinguishable, which is why only two graphs are displayed. We present constraints on the squared values because they are directly related to the event yields and most closely follow the Gaussian probability distributions. Table 5.2 shows a summary of the 68 and 95% CL intervals on four couplings, either with no constraints on the couplings or with certain couplings constrained to the null SM expectation.

5.3 Analysis of the light-quark Yukawa couplings

The emission of the Higgs boson and a photon from a quark in the $q\bar{q}$ annihilation, depicted in Fig. 5.3 (right), is the dominant γH production channel in the SM [164]. However, this production mechanism would result in a photon with very low p_T, of less than 1 GeV on average, as determined from a dedicated simulation shown in Fig. 5.4 [115, 165, 166]. Differentiating this production mechanism from others, such as gluon fusion (ggH), becomes exceedingly challenging because of the presence of soft photons, whether genuine or spurious, throughout the rest of the proton-proton (pp) collision event. Nevertheless, an increased Yukawa coupling of light quarks could

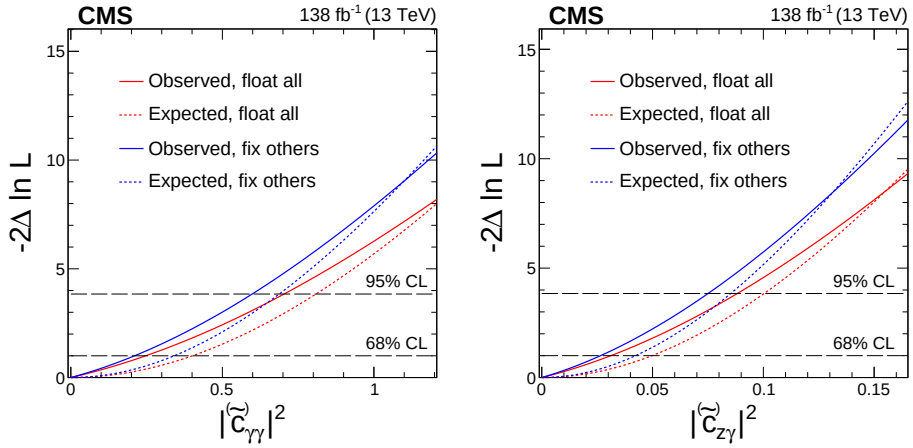

Figure 5.8: Constraints on the square of $|c_{\gamma\gamma}|$ (or $|\tilde{c}_{\gamma\gamma}|$) and $|c_{z\gamma}|$ (or $|\tilde{c}_{z\gamma}|$) from the combination of the $H \to b\bar{b}$ and 4ℓ channels. The other couplings are either fixed to the null SM expectation (blue) or are left floating in the fit (red). Observed (solid) and expected (dashed) likelihood scans are shown. The dashed horizontal lines show the 68 and 95% CL intervals.

change the production rate associated with this mechanism.

This motivated an approach to constrain the Yukawa coupling of light quarks by imposing constraints on the γH production rate [172]. However, the presence of an associated photon in this context does not effectively aid such an analysis due to the soft p_{T} spectrum. This photon merely represents a radiative correction to the direct $q\bar{q}$ annihilation illustrated in Fig. 5.9 (left). Therefore, we investigate the inclusive production of the Higgs boson to explore the potential enhancement of the Hqq coupling. This enhancement would also change the rate of the gluon fusion process depicted in Fig. 5.9 (right), necessitating its consideration in this analysis as well. The concept for this analysis was initially introduced in Refs. [173, 174] and has been revisited more recently in Ref. [175].

Other strategies have been proposed to constrain the Yukawa couplings of bottom and

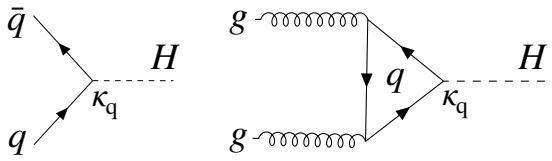

Figure 5.9: Feynman diagrams describing the Higgs boson production at LHC through direct $q\bar{q}$ annihilation (left) and gluon fusion production (right).

charm quarks. Measurements of transverse momentum distributions in Higgs boson production [176] have been used to derive experimental constraints, as outlined in Refs. [161, 177, 178]. Radiative decays of the Higgs boson to mesons could also be used to constrain the quark couplings [179]. Constraints on the Hcc coupling have been directly derived from searches for Higgs boson decays into charm quarks [180, 181]. However, there are currently no stringent constraints on the couplings involving the s, d, and u quarks.

The limits on γH production could be used to constrain the Yukawa couplings of light quarks, as proposed in Ref. [172]. However, the photon involved in this process is considerably softer than the one in diagram Fig. 5.3 (left). This motivates a reoptimization of the photon selection criteria introduced in Section 5.2.1. Upon testing, we find that the expected constraints remain unchanged, regardless of the selection requirement on p_{T}^{γ}. This effect is observed because a soft photon can easily be associated with an Higgs boson produced via gluon fusion, for instance. Therefore, the distinction between the Untagged and γ-tagged categories is unnecessary. Instead, we must constrain light-quark Yukawa couplings by examining changes in the Higgs boson production rate, regardless of the production mode.

This leads us to perform an inclusive analysis of $\mathrm{H} \to 4\ell$ production, similar to the

methods proposed in Refs. [173, 174], but with a more detailed focus on both the reconstruction and computational aspects. The four-lepton final state is especially suitable for this analysis because the decay is largely unaffected by the Higgs boson couplings to quarks at the relevant scale. Additionally, the inclusive $H \to 4\ell$ reconstruction maintains high signal purity and is almost entirely independent of the production mechanism. Consequently, only the effects on production couplings and total width Γ_H of the Higgs boson need to be taken into account. In this interpretation, we combine the Untagged and γ-tagged categories into one, while keeping the 4ℓ selection criteria unchanged.

5.3.1 Cross section dependence on the light-quark Yukawa couplings

The SM $b\bar{b}H$ process serves as a reference for Higgs boson production driven by light quarks at the tree level, $q\bar{q}H$, where the rates are adjusted according to κ_u, κ_d, κ_s, κ_c, and κ_b. The rate of the gluon fusion process is also expressed as a function of κ_q, while all other production mechanisms of the Higgs boson considered remain unchanged. The couplings κ_b and κ_t are well constrained by the analysis of the on-shell Higgs boson data [182, 183], including the $H \to b\bar{b}$ decay, and $t\bar{t}H$ and ggH production, and thus are fixed to $\kappa_b = \kappa_t = 1$ in this analysis. However, they are sometimes allowed to vary for studies and validation of the techniques presented in Section 5.3.3.

The total width of the Higgs boson is parameterized, as shown below:

$$\Gamma_{\mathrm{H}} = R_{\mathrm{gg}}(\kappa_{\mathrm{u,d,s,c,b}})\,\Gamma^{\mathrm{SM}}_{\mathrm{H}\to\mathrm{gg}} + \sum_{\mathrm{q=u,d,s,c,b}} \kappa^2_{\mathrm{q}}\,\Gamma^{\mathrm{SM}}_{\mathrm{H}\to\mathrm{q\overline{q}}} + \sum_{\mathrm{VV'}} \kappa^2_{\mathrm{VV'}}\,\Gamma^{\mathrm{SM}}_{\mathrm{H}\to\mathrm{VV'}} + \sum_{\ell} \Gamma^{\mathrm{SM}}_{\mathrm{H}\to\ell\ell} + \Gamma^{\mathrm{BSM}}_{\mathrm{H}}, \tag{5.4}$$

where the partial widths $\Gamma^{\mathrm{SM}}_{\mathrm{H}\to f}$ are calculated using the SM values for all couplings, while the partial width for decays to BSM particles is generally unknown and is constrained only by $\Gamma^{\mathrm{BSM}}_{\mathrm{H}} \geq 0$. In the partial width for the decay $\mathrm{H}\to\mathrm{VV'}$, V or V′ can be W, Z, or γ. Since this decay is primarily governed by the tree-level couplings HZZ and HWW, the influence of light-quark Yukawa couplings is highly suppressed and negligible compared to the direct $\mathrm{H}\to\mathrm{q\overline{q}}$ partial width with enhanced couplings. The coupling strength modifiers $\kappa_{\mathrm{VV'}}$ are introduced to account for potential BSM effects and will be elaborated on below. In the SM, their values are $\kappa_{\mathrm{VV'}} = 1$. The partial width for the decay $\mathrm{H}\to\ell\ell$, where ℓ denotes leptons e, μ, or τ, and neutrinos are neglected, is independent of κ_{q}. Thus, the dependence on κ_{q} is present only in the $\mathrm{H}\to\mathrm{q\overline{q}}$ and $\mathrm{H}\to\mathrm{gg}$ processes.

The cross section of the on-shell Higgs boson production at the LHC, $\mathrm{pp}\to\mathrm{H}\to 4\ell$, is inversely proportional to the total width of the Higgs boson and is parameterized as shown below:

$$\sigma_{\mathrm{H}\to 4\ell} = \frac{\Gamma^{\mathrm{SM}}_{\mathrm{H}\to 4\ell}\,\kappa^2_{\mathrm{ZZ}}}{\Gamma_{\mathrm{H}}(\kappa_{\mathrm{u,d,s,c,b}})} \left(R_{\mathrm{gg}}(\kappa_{\mathrm{u,d,s,c,b}})\,\sigma^{\mathrm{SM}}_{\mathrm{ggH}} + \sum_{\mathrm{q}} \kappa^2_{\mathrm{q}}\,\sigma^{\mathrm{SM}}_{\mathrm{q\overline{q}H}} + \sigma^{\mathrm{SM}}_{\mathrm{t\overline{t}H}} + \sigma^{\mathrm{SM}}_{\mathrm{tH}} + \sum_{\mathrm{VV}} \kappa^2_{\mathrm{VV}}\,\sigma^{\mathrm{SM}}_{\mathrm{VVH}} \right), \tag{5.5}$$

where the partial width for the decay $H \to ZZ \to 4\ell$, which is a subprocess of $H \to ZZ$, is scaled by the coupling strength modifier κ_{ZZ} introduced earlier, and all cross sections σ_i^{SM} are computed for the inclusive on-shell Higgs boson production using the SM values for all couplings. The production in association with top quarks ($t\bar{t}H$, tH) and VH or VBF production (VVH) are independent of κ_q. The latter arises for reasons similar to those discussed for the $H \to VV'$ decay, with some exceptions, such as the box diagram in the $gg \to ZH$ production. However, this contribution is minor in the $gg \to ZH$ process and is negligible compared to the $gg \to H$ process for any values of the quark Yukawa couplings. The VBF, ZH, and WH production processes are scaled by either κ_{ZZ}^2 or κ_{WW}^2, with the interference between the two contributions in the VBF process being negligible.

Table 5.3: Central values of the input and derived parameters used in calculations involving Eqs. (5.4) and (5.5). The list of partons (p) comprises gluons (g) and five quark flavors (q). All cross sections σ_i are computed for the inclusive on-shell Higgs boson production using the SM values for all couplings, except for the specific coupling κ_q that is explicitly mentioned.

p	$\Gamma^{SM}_{H\to p\bar{p}}/\Gamma^{SM}_{H}$	$\sigma^{SM}_{p\bar{p}H}$ (pb)	$\frac{\sigma_{ggH}(\kappa_q=0)}{\sigma^{SM}_{ggH}} - 1$	$\frac{\sigma_{ggH}(\kappa_q \gg 1)}{\sigma^{SM}_{ggH}}$	$\frac{\sigma_{q\bar{q}H}(\kappa_q \gg 1)}{\sigma^{SM}_{ggH}}$
g	8.187×10^{-2}	4.858×10	—	—	—
b	5.824×10^{-1}	4.880×10^{-1}	1.595	1.422×10^{-2}	1.723×10^{-2}
c	2.891×10^{-2}	7.735×10^{-2}	4.254×10^{-2}	2.794×10^{-3}	5.506×10^{-2}
s	2.152×10^{-4}	1.854×10^{-3}	5.040×10^{-4}	1.518×10^{-4}	1.774×10^{-1}
d	5.552×10^{-7}	1.381×10^{-5}	2.087×10^{-6}	1.459×10^{-6}	5.120×10^{-1}
u	1.183×10^{-7}	4.155×10^{-6}	5.050×10^{-7}	4.189×10^{-7}	7.234×10^{-1}

The rates of the gluon fusion process in Eq. (5.5) and of the decay to gluons in Eq. (5.4) are both scaled by the same factor R_{gg}, which depends on the couplings of all quarks involved in the Hgg loop. The calculation of $R_{gg}(\kappa_{u,d,s,c,b})$ is carried out using MCFM code within the JHUGEN package, extending the computation in Ref. [138] to include light quarks. Since R_{gg} is used as a scaling factor in front of σ^{SM}_{ggH} calculated at next-to-NNLO in QCD [79], the ggH cross section in Eq. (5.5) corresponds to the same order under the assumption that the K factor for matching the LO ggH cross section is independent of the quark flavor.

The partial decay width $\Gamma^{SM}_{H\to q\bar{q}}$ in Eq. (5.4) is calculated using Ref. [184] for $q = u, d, s, c$, while the $H \to b\bar{b}$ value is obtained from Ref. [79]. The decay width of the Higgs boson to two quarks is well understood under the assumption that the quark masses are small compared to the Higgs boson mass $m_H = 125\,\text{GeV}$, which is a valid approximation for the light quarks considered in this analysis. Calculations use the running mass of the light quarks at m_H [185]. A uniform K factor is applied to match the $H \to c\bar{c}$ partial decay width to the most accurate value in Ref. [79].

The cross section of the $q\bar{q}H$ process as a function of the light-quark Yukawa coupling for each flavor of q in Eq. (5.5) is calculated at NNLO in QCD with SusHi [186]. As such, this process involves light quarks coupled to the Higgs boson in either the initial or final states. Reference [187] demonstrated that the calculation for $b\bar{b}H$ at NNLO in QCD is analogous to the calculation for $q\bar{q}H$ production with light quarks. The main differences stem from the distinct quark Yukawa couplings and variations in the flavor composition of the PDFs. The central values for the QCD factorization and renormalization scales are set to $m_H/4$ and m_H, respectively, with systematic

variations by a factor of 2, leading to cross section uncertainties between 3 and 5%, depending on the quark flavor. Similarly, PDF variations lead to uncertainties between 3 and 9%. For the $\mathrm{b\bar{b}H}$ and $\mathrm{c\bar{c}H}$ processes, the cross sections from Ref. [79] are reproduced with good accuracy. The typical K factor relative to the LO in the QCD calculation of the process $\mathrm{q\bar{q}} \to \mathrm{H}$ is 1.2. The effect of the interference between the $\mathrm{q\bar{q}H}$ process and gluon fusion at higher orders in QCD is found to be negligible compared to the individual contributions.

Table 5.3 illustrates the numerical values of the parameters used in calculations involving Eqs. (5.4) and (5.5), as well as their asymptotic behavior. The concept of this analysis can be grasped by examining how the calculation in Eq. (5.5) varies with κ_q for a specific quark flavor q. Cross sections for all processes that do not explicitly depend on κ_q will decrease as κ_q increases above 1, due to the rise in $\Gamma_\mathrm{H}(\kappa_\mathrm{q})$ in the denominator, as indicated by Eq. (5.4). The cross section for the gluon fusion process will also decrease, but at a slower rate due to the interplay between the quadratic dependence on κ_q in both the total width and R_gg. This cross section will ultimately reach a plateau at $\kappa_\mathrm{q} \gg 1$ when the κ_q^2 term becomes dominant in $R_\mathrm{gg}(\kappa_\mathrm{q})$. In contrast, the cross section for the $\mathrm{q\bar{q}H}$ process will increase with rising κ_q because the numerator in Eq. (5.5) grows faster than the denominator. However, this increase will eventually level off, reaching an asymptotic value at $\kappa_\mathrm{q} \gg 1$, where the terms proportional to κ_q^2 become dominant in both the numerator and the denominator.

5.3.2 Statistical Analysis

The fit to the data closely follows the approach outlined in Section 5.2.3. The extended likelihood function is built using probability densities that characterize both signal and background events as functions of the $\mathcal{D}_{\text{bkg}}$ observable in the 4ℓ channel. The $\mathcal{D}_{\text{bkg}}$ parameterizations for all $\text{q}\overline{\text{q}}\text{H}$ processes are modeled based on the $\text{b}\overline{\text{b}}\text{H}$ simulation, with the yields of all processes rescaled according to Eq. (5.5). The fit is conducted in two scenarios. In the first scenario, κ_{q} for a specific quark flavor q is left unconstrained, while all other coupling modifiers are fixed at their SM values: $\kappa_{\text{q}'} = 1$ for $\text{q}' \neq \text{q}$, $\kappa_{\text{ZZ}} = 1$, and $\Gamma_{\text{H}}^{\text{BSM}} = 0$. In the second scenario, $\kappa_{\text{b}} = \kappa_{\text{t}} = 1$ is set, while the Yukawa couplings of all other quarks remain unconstrained, with $\kappa_{\text{ZZ}}^2 \leq 1$ and $\Gamma_{\text{H}}^{\text{BSM}} \geq 0$. Figure 5.10 illustrates the constraints on each κ_{q}, and Table 5.4 presents the 68 and 95% CL intervals for κ_{q} in both scenarios. The results are quite similar in both scenarios, as previously discussed, but the results from the simultaneous fitting of all light-quark Yukawa couplings are more general.

5.3.3 Results light Yukawa couplings

The results of the fit, represented by the $\overline{\kappa}_{\text{q}}$ parameters, provide a means to compare the hierarchy of Yukawa couplings of light quarks relative to the b and t quarks. These results are presented in Table 5.5. They are based on the assumption that both third-generation quarks, b and t, couple to the Higgs boson with strengths consistent with the SM. Under this assumption, the hypothesis that $y_{\text{u}} = y_{\text{t}}^{\text{SM}}$, $y_{\text{c}} = y_{\text{t}}^{\text{SM}}$, $y_{\text{d}} = y_{\text{b}}^{\text{SM}}$, or $y_{\text{s}} = y_{\text{b}}^{\text{SM}}$, that is up-type (u or c) or down-type (d or s) quarks in the first or second generation, have the same couplings as those in the third generation (t or b, respectively), is excluded with a CL greater than 95%. It is not surprising that the

limits on $\overline{\kappa}_{\mathrm{q}}$ for the four light quarks are of a similar magnitude to the SM value for the b quark, as it is the Yukawa couplings that make a significant contribution to the Higgs boson decay width.

When $\Gamma_{\mathrm{H}}^{\mathrm{BSM}}$ is allowed to vary in the fit, the resulting constraints are: $\Gamma_{\mathrm{H}}^{\mathrm{BSM}} = 0.0^{+0.9}_{-0.0}$ MeV with an upper limit of 1.6 MeV at 95% CL. The constraints are expected to be $\Gamma_{\mathrm{H}}^{\mathrm{BSM}} = 0.0^{+0.7}_{-0.0}$ MeV (< 1.4 MeV). This constraint is possible due to the assumptions made about other couplings, such as $\kappa_{\mathrm{ZZ}}^2 < 1$. Bounds on $\Gamma_{\mathrm{H}}^{\mathrm{BSM}}$ can be obtained from existing off-shell Higgs boson data [68, 188, 189] without needing constraints on other couplings. However, these bounds, along with those obtained from the combined analysis of Higgs boson data at the LHC [182, 183] are valid only under the assumption of small Yukawa couplings for the light quarks. This assumption is not applicable to the results presented in this paper.

In all of the fits mentioned above, the third-generation quark couplings are held fixed at their SM values, $\kappa_{\mathrm{t}} = 1$ and $\kappa_{\mathrm{b}} = 1$. If these constraints are relaxed to Gaussian constraints with 11 and 17% uncertainties, respectively, representing recent constraints from combined CMS data [183], the achieved bounds at 68% CL on κ_{c}, κ_{s}, κ_{d}, κ_{u}, and $\Gamma_{\mathrm{H}}^{\mathrm{BSM}}$ vary by no more than 47, 37, 33, 33, and 95%, respectively. Alternatively, one can constrain only the top quark coupling, such as setting $\kappa_{\mathrm{t}} = 1$, while allowing κ_{b} to vary freely, and still obtain bounds on the light-quark Yukawa couplings that are only somewhat less stringent than those shown in Table 5.4. For instance, a fit where κ_{b} and κ_{c} are allowed to vary would be analogous to the results presented in Eq. (12) and Fig. 27 (left) of Ref. [178] using the same $\mathrm{H} \to 4\ell$ data, where only minor approximations were made compared to the methodology used in this paper.

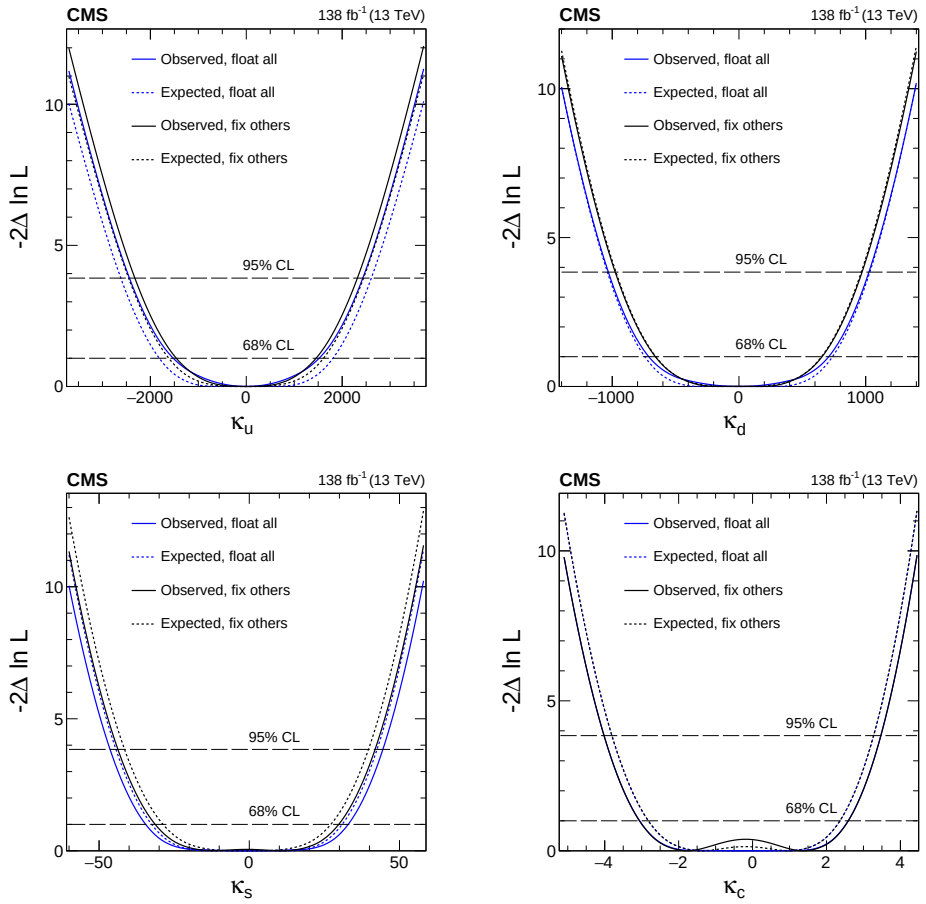

Figure 5.10: Constraints on κ_u, κ_d, κ_s, and κ_c are shown using the $H \to 4\ell$ channel. In scenario one (black), all couplings except the one being shown are fixed at their SM values. In scenario two (blue), the Yukawa couplings for the three other light quarks are left unconstrained, and BSM contributions are allowed: $\kappa^2_{ZZ} \leq 1$ and $\Gamma_H^{BSM} \geq 0$. Both observed (solid) and expected (dashed) constraints are presented. The crossings of dashed horizontal lines and the likelihood curves indicate the 68 and 95% CL intervals.

5.4 SMEFT interpretation of spin-correlation measurements

As described earlier in Section 4.1, both the CMS and ATLAS experiments have consistently shown that the quantum numbers of the Higgs boson are consistent with

Table 5.4: Observed and expected constraints on the κ_u, κ_d, κ_s, and κ_c couplings are shown using the $H \to 4\ell$ channel. In one scenario, all couplings except the one being shown are fixed at their SM values. In the other scenario, the Yukawa couplings for the three other light quarks are left unconstrained, and BSM contributions are allowed. The 68% (central value with error bars) and 95% (bracketed range or upper limit) CL intervals are displayed.

Parameter	Scenario	Observed		Expected	
		68% CL	95% CL	68% CL	95% CL
κ_u	float all	$(0.0 \pm 1.5) \times 10^3$	$[-2.4, 2.4] \times 10^3$	$(0.0 \pm 1.8) \times 10^3$	$[-2.6, 2.6] \times 10^3$
κ_u	fix others	$(0.0 \pm 1.4) \times 10^3$	$[-2.3, 2.3] \times 10^3$	$(0.0 \pm 1.6) \times 10^3$	$[-2.5, 2.5] \times 10^3$
κ_d	float all	$(0.0 \pm 7.1) \times 10^2$	$[-1.0, 1.0] \times 10^3$	$(0.0 \pm 7.4) \times 10^2$	$[-1.0, 1.0] \times 10^3$
κ_d	fix others	$(1.5^{+5.0}_{-8.0}) \times 10^2$	$[-9.7, 9.7] \times 10^2$	$(0.0 \pm 6.5) \times 10^2$	$[-9.7, 9.7] \times 10^2$
κ_s	float all	0^{+33}_{-34}	$[-46, 44]$	1^{+32}_{-31}	$[-44, 42]$
κ_s	fix others	11^{+19}_{-42}	$[-44, 42]$	1^{+26}_{-30}	$[-41, 40]$
κ_c	float all	$0.0^{+2.7}_{-3.0}$	$[-4.0, 3.4]$	$1.0^{+1.4}_{-3.8}$	$[-3.8, 3.2]$
κ_c	fix others	$1.4^{+1.2}_{-4.4}$	$[-4.0, 3.5]$	$1.0^{+1.3}_{-3.8}$	$[-3.8, 3.2]$
Γ_H^{BSM} (MeV)	float all	$0.0^{+0.9}_{-0.0}$	<1.6	$0.0^{+0.7}_{-0.0}$	<1.4

the SM prediction of $J^{PC} = 0^{++}$, but small anomalous HVV couplings to two EW gauge bosons $V = \gamma, Z, W$ are still allowed. Constraints on these couplings have also been set in the framework of EFT in multiple analysis on CMS and ATLAS.

However, these analyses were subject to several simplifications: they either relied on differential distributions extracted from data under SM assumptions, resulting in potentially biased results and some loss of information; or they included only a limited set of EFT operators, given the complexity of performing a full EFT analysis with full detector simulations [67, 68, 69]; and they almost always heavily relied on the q^2

Table 5.5: Observed and expected constraints on the $\overline{\kappa}_{\mathrm{u}}$, $\overline{\kappa}_{\mathrm{d}}$, $\overline{\kappa}_{\mathrm{s}}$, and $\overline{\kappa}_{\mathrm{c}}$ defined as $\overline{\kappa}_{\mathrm{q}} = y_{\mathrm{q}} v / m_{\mathrm{b}}$, following the same conventions as outlined in Table 5.4.

Parameter	Scenario	Observed		Expected	
		68% CL	95% CL	68% CL	95% CL
$\overline{\kappa}_{\mathrm{u}}$	float all	0.00 ± 0.66	$[-1.06, 1.05]$	$0.00^{+0.78}_{-0.79}$	$[-1.13, 1.13]$
$\overline{\kappa}_{\mathrm{u}}$	fix others	$0.00^{+0.63}_{-0.64}$	$[-1.00, 1.00]$	0.00 ± 0.70	$[-1.06, 1.06]$
$\overline{\kappa}_{\mathrm{d}}$	float all	0.00 ± 0.67	$[-0.97, 0.97]$	0.00 ± 0.70	$[-0.98, 0.97]$
$\overline{\kappa}_{\mathrm{d}}$	fix others	$0.14^{+0.46}_{-0.77}$	$[-0.92, 0.92]$	$0.00^{+0.61}_{-0.62}$	$[-0.91, 0.91]$
$\overline{\kappa}_{\mathrm{s}}$	float all	$0.00^{+0.63}_{-0.65}$	$[-0.89, 0.85]$	$0.02^{+0.57}_{-0.64}$	$[-0.85, 0.81]$
$\overline{\kappa}_{\mathrm{s}}$	fix others	$0.21^{+0.36}_{-0.81}$	$[-0.84, 0.80]$	$0.02^{+0.5}_{-0.57}$	$[-0.79, 0.76]$
$\overline{\kappa}_{\mathrm{c}}$	float all	$-0.01^{+0.58}_{-0.66}$	$[-0.88, 0.76]$	$0.22^{+0.30}_{-0.84}$	$[-0.83, 0.72]$
$\overline{\kappa}_{\mathrm{c}}$	fix others	$0.30^{+0.27}_{-0.97}$	$[-0.88, 0.76]$	$0.22^{+0.30}_{-0.84}$	$[-0.83, 0.72]$

growth of EFT contributions without accounting for the validity of the EFT and the need to truncate the energy range accordingly [190]. For example, several previous EFT analyses operated under the assumption that the anomalous HZγ and H$\gamma\gamma$ couplings were already stringently constrained. Relaxing these assumptions would be preferable within a more general EFT framework, ensuring consistency with EFT interpretations across other Higgs boson channels.

The H $\rightarrow 4\ell$ decay channel provides an excellent framework for addressing the above issues. It is sensitive to a number of EFT operators and its clean final state allows precise kinematic reconstruction. This provides a clean yet precise channel

for conducting a dedicated analysis capable of simultaneously probing a broad set of EFT operators. In particular, it has been demonstrated that the H $\to 4\ell$ decay channel offers superior sensitivity to separate CP-odd and CP-even HZγ and H$\gamma\gamma$ couplings compared to production processes such as VBF and VH [138]. Moreover, the H $\to$ VV $\to 4\ell$ channel inherently constrains the momentum transfer q^2 to values below m_{H}^2. While this may be seen as a limitation compared to VBF and VH production channels assuming an EFT framework valid at arbitrarily high energies, it becomes a significant advantage when applying an energy cutoff, as the results from this channel remain valid for any cutoff above m_H.

In a single decay channel of the Higgs boson, it is not possible to directly constrain all contribution EFT couplings without making additional assumptions, because the total width of the Higgs boson Γ_{tot} and production cross sections depend on a larger number of couplings than there are available experimental constraints in analysis of the decay H $\to 4\ell$. As a consequence, the constraints on individual couplings become degenerate. However, by redefining the couplings c_m in Eq. (4.4) as c'_m, we can factor out all degenerate couplings (enclosed in square brackets), while the remaining terms (in round brackets) describe the differential distribution of a decay:

$$\frac{d\sigma(\vec{x})}{d\vec{x}} = \left[\frac{\sum \gamma_{jk}^{\mathrm{prod}} b_j b_k}{\Gamma_{\mathrm{tot}}(\vec{c})}(1+\delta c_z)^2\right]\left(\gamma_{00}^{\mathrm{dec}}(\vec{x}) + \sum_{1\le m} \gamma_{0m}^{\mathrm{dec}}(\vec{x}) c'_m + \sum_{1\le m\le l} \gamma_{lm}^{\mathrm{dec}}(\vec{x}) c'_l c'_m\right), \tag{5.6}$$

where $\gamma_{00}^{\mathrm{dec}}(\vec{x})$ describes the SM decay process as function of the observables $\vec{x}$, and the production process is described by the couplings b_j and the corresponding factors $\gamma_{jk}^{\mathrm{prod}}$. The parameters c'_m are expressed as ratios of the couplings to the combination $(\delta c_z + 1)$, which controls the SM-like tensor structure of the interactions as evident

from Eq. (4.3):

$$c'_m = c_m/(\delta c_z + 1)\,. \tag{5.7}$$

Constraining the coupling ratios in Eq. (5.7) is equivalent to placing bounds on the parameters f_{ai} (see, e.g., Eq. (43) in Ref. [138]). We observe that $c'_m \simeq c_m$ when $|\delta c_z| \ll 1$.

Equation (5.6) allows us to analyze the $\mathrm{H} \to 4\ell$ decay as a function of kinematic observables $\vec{x}$ with seven coupling ratios defined in Eq. (5.7) constructed from the first eight couplings listed in Eq. (4.4), or equivalently with seven f_{ai} values, and one overall strength parameter which incorporated the term in the square brackets.

5.4.1 Kinematic discriminants for EFT

Since we target seven anomalous HVV coupling ratios appearing in Eq. (5.7), optimal analysis of the $\mathrm{H} \to \mathrm{VV} \to 4\ell$ decay requires seven discriminants of the type given by Eq. (5.1) and seven discriminants of the type given by Eq. (5.2). However, since the focus is on small coupling values within the validity range of the EFT, we consider only seven observables of the latter type, noting that the analysis remains optimal only in the vicinity of the SM. The $\mathcal{D}_{\Lambda 1}$ discriminant is shown in Fig. 5.2, while the remaining six discriminants $\mathcal{D}_{CP}$, $\mathcal{D}_{\mathrm{int}}$, $\mathcal{D}_{CP}^{\mathrm{Z}\gamma}$, $\mathcal{D}_{\mathrm{int}}^{\mathrm{Z}\gamma}$, $\mathcal{D}_{CP}^{\gamma\gamma}$, and $\mathcal{D}_{\mathrm{int}}^{\gamma\gamma}$ are shown in Fig. 5.11.

Although Figs. 5.2 and 5.11 display one-dimensional projections of the seven observables, they do not reveal the correlations between them, correlations that are nonetheless important. The full probability distribution is parameterized in seven dimensions, with each dimension divided into four to six bins, except for $\mathcal{D}_{CP}^{\gamma\gamma}$, which

is divided into two bins. Due to correlations between observables, some bins are either entirely empty or contain redundant information, and those bins are merged. The full parameterization also includes the $\mathcal{D}_{\text{bkg}}$ observable, and all bins of the EFT discriminants are merged into a single bin for $\mathcal{D}_{\text{bkg}} < 0.2$, which is dominated by background. The seven-dimensional distribution retains substantial kinematic information that is nearly optimal for all anomalous couplings targeted in this analysis. This has been validated against a dedicated analysis targeting one anomalous coupling at a time with a much larger number of bins in each dimension for a smaller number of discriminants. This nearly optimal performance is realized in large respect due to the optimal population of events across the range of discriminant values by construction of the MELA approach.

5.4.2 Statistical Analysis in the EFT Framework

In the case of HVV anomalous couplings, we have $L = 8$ couplings, which we can parameterize with seven components of $\vec{f}$, defined above, and $f_{a1} = (1 - |f_{a2}| - |f_{a3}| - |f_{\Lambda 1}| - |f_{a2}^{Z\gamma}| - |f_{a2}^{\gamma\gamma}| - |f_{a3}^{Z\gamma}| - |f_{a3}^{\gamma\gamma}|)$. Let us denote these as f_l with $l = 1, 2, 3, 4, 5, 6, 7, 8$. When developing the expression in Eq. (5.6), one gets a polynomial in the couplings $a_l \propto \sqrt{|f_l|}\, sign(f_l)$, which is quadratic ($C = 2$). Parameterization of the anomalous coupling dependence of the $\mathcal{P}_k^{\text{sig}}$ probability density in Eq. (5.3) can be expressed as

$$\mathcal{P}_k^{\text{sig}}\left(\vec{x};\vec{\xi}_k,\vec{f}\right) \propto \sum_{l\leq m=1}^{L} \mathcal{P}_{k,lm}^{\text{sig}}\left(\vec{x};\vec{\xi}_k\right) \sqrt{|f_l\, f_m|}\; sign(f_l\, f_m)\,. \tag{5.8}$$

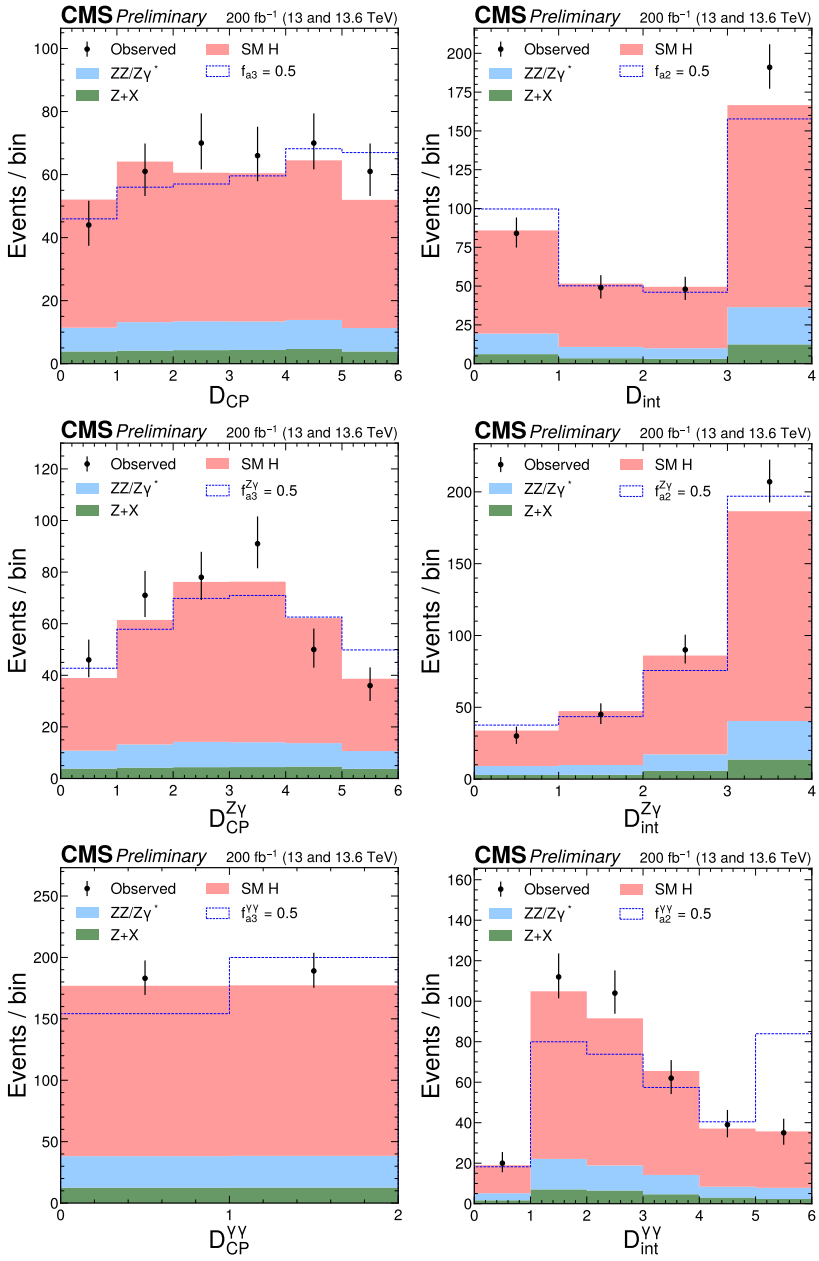

Figure 5.11: Distributions of $\mathcal{D}_{CP}$, $\mathcal{D}_{\text{int}}$, $\mathcal{D}_{CP}^{\text{Z}\gamma}$, $\mathcal{D}_{\text{int}}^{\text{Z}\gamma}$, $\mathcal{D}_{CP}^{\gamma\gamma}$, and $\mathcal{D}_{\text{int}}^{\gamma\gamma}$, compared with the expected distributions from the SM, shown as red histograms, and those from an alternative model, shown as blue lines. The alternative model includes an exaggerated enhancement of a BSM effect, corresponding to a coupling with $f_{ai} = 0.5$. To enhance the signal-to-background ratio, a selection $\mathcal{D}_{\text{bkg}} > 0.6$ is applied.

In Eq. (5.8), only the kinematic dependence on $\vec{f}_j$ is expressed, while the overall normalization can be absorbed into μ_j.

In the general case, there are $(C + L - 1)!/(C!(L - 1)!)$ terms in Eq. (5.8). This leads to 36 terms in Eq. (5.8) when we measure eight anomalous HVV couplings in decay ($L = 8$, $C = 2$). However, the majority of the 36 terms correspond to interference between different BSM contributions and can be neglected within the EFT approximation. As a result, only 15 terms are retained: one SM coupling, seven interference terms between BSM and SM contributions, and seven pure quadratic terms corresponding to individual BSM couplings. This selection ensures the stability of the fit and allows for tests of its validity.

The $\mathcal{P}^{\text{sig}}_{k,lm}$ templates are extracted from simulation, typically using a dozen of samples generated with various $\vec{f}$ values chosen to map different points of phase-space well and re-weighted with the MELA package to cover all possibilities with $(C+L-1)!/(C!(L-1)!)$ combinations of couplings. In parameterizing the signal templates $\mathcal{P}^{\text{sig}}_{jk,lm}$, it is important to ensure that the expected number of events in every bin of the probability densities, defined in Eq. (5.8), remains nonnegative at all possible values of $\vec{f}$, because a negative yield would cause the likelihood function used for the final fit to become ill-defined.

5.4.3 Results constraints on EFT cross section ratios

In the following, we present and discuss the results of the fits introduced in Sec. 5.4.2. In all cases, the signal strength μ_{sig} and the set of parameters of interest $\vec{f}$ describing the tensor structure of interactions in Eq. (4.1) within certain framework are constrained

in decay $H \to ZZ$ / $Z\gamma^*$ / $\gamma^*\gamma^* \to 4\ell$. When reporting $\vec{f}$ results, the signal strength parameters have been left unconstrained.

Within the EFT framework, we carry out the measurement of the parameter set $\vec{f} = (f_{a3}\ ,\ f_{a3}^{Z\gamma},\ f_{a3}^{\gamma\gamma},\ f_{a2},\ f_{a2}^{Z\gamma},\ f_{a2}^{\gamma\gamma},\ f_{\Lambda 1})$, corresponding to the fraction contributions of the seven coupling ratios $\tilde{c}'_{zz}, \tilde{c}'_{z\gamma}, \tilde{c}'_{\gamma\gamma}, c'_{zz}, c'_{z\gamma}, c'_{\gamma\gamma}, c'_{z\Box}$. Figures 5.12 and 5.13 show constraints on these parameters. The numerical results are presented in Table 5.6. Constraints on each operator are presented both with the remaining operators set to zero and with them left unconstrained.

Compared to the published results from the $H \to 4\ell$ channel [67], the constraints on the three common parameters, f_{a2}, f_{a3}, and $f_{\Lambda 1}$, are consistent when considering two key factors. First, the previous publication includes VBF and VH production channels, which contribute a narrow but relatively weak constraint on these parameters, complementing the broader constraint derived from decay information. Second, constraints at large value close to $f_i = \pm 1$ are not always as strong with the new approach. However, this is expected, as the $\mathcal{D}_{\text{alt}}$ discriminants are no longer used, reflecting the focus on a narrower range of f_i values within the valid domain of the EFT framework.

Most importantly, four of the seven parameters are newly introduced relative to the previous CMS publication on this topic [67]. These are the $f_{a3}^{Z\gamma}$, $f_{a3}^{\gamma\gamma}$, $f_{a2}^{Z\gamma}$, and $f_{a2}^{\gamma\gamma}$ parameters, corresponding to $\tilde{c}'_{z\gamma}, \tilde{c}'_{\gamma\gamma}, c'_{z\gamma}, c'_{\gamma\gamma}$. Inclusion of these parameters completes the full set of EFT operators which are necessary to include these results in the global EFT fits. With the exception of a limited set of differential distributions, which are not

Table 5.6: Observed and expected constraints on fractional contribution in the EFT framework.

$\vec{f}$	Scenario	Observed		Expected	
		68% CL	95% CL	68% CL	95% CL
f_{a3}	float all	$0.158^{+0.147}_{-0.076}$	$[0.012, 0.465]$	$0.000^{+0.142}_{-0.149}$	$[-0.461, 0.457]$
	fix others	$0.185^{+0.155}_{-0.121}$	$[0.008, 0.502]$	$0.000^{+0.063}_{-0.064}$	$[-0.227, 0.221]$
$f_{a3}^{Z\gamma}$	float all	$0.000^{+0.081}_{-0.084}$	$[-0.236, 0.228]$	$0.000^{+0.313}_{-0.298}$	$[-0.493, 0.508]$
	fix others	$-0.003^{+0.055}_{-0.110}$	$[-0.265, 0.198]$	$-0.000^{+0.221}_{-0.219}$	$[-0.400, 0.403]$
$f_{a3}^{\gamma\gamma}$	float all	$0.034^{+0.083}_{-0.051}$	$[-0.090, 0.198]$	$0.000^{+0.052}_{-0.048}$	$[-0.153, 0.167]$
	fix others	$0.008^{+0.069}_{-0.026}$	$[-0.087, 0.162]$	$0.000^{+0.030}_{-0.028}$	$[-0.091, 0.102]$
f_{a2}	float all	$0.169^{+0.252}_{-0.107}$	$[-0.001, 0.625]$	$0.000^{+0.530}_{-0.086}$	$[-0.210, 0.826]$
	fix others	$0.334^{+0.246}_{-0.241}$	$[0.003, 0.769]$	$0.000^{+0.138}_{-0.046}$	$[-0.146, 0.794]$
$f_{a2}^{Z\gamma}$	float all	$-0.001^{+0.051}_{-0.056}$	$[-0.183, 0.194]$	$0.000^{+0.333}_{-0.310}$	$[-0.534, 0.567]$
	fix others	$0.020^{+0.103}_{-0.031}$	$[-0.093, 0.263]$	$0.000^{+0.178}_{-0.161}$	$[-0.387, 0.406]$
$f_{a2}^{\gamma\gamma}$	float all	$-0.003^{+0.020}_{-0.068}$	$[-0.192, 0.081]$	$0.000^{+0.031}_{-0.078}$	$[-0.213, 0.107]$
	fix others	$-0.009^{+0.014}_{-0.046}$	$[-0.125, 0.035]$	$0.000^{+0.019}_{-0.021}$	$[-0.077, 0.065]$
$f_{\Lambda 1}$	float all	$0.062^{+0.194}_{-0.078}$	$[-0.125, 0.416]$	$0.000^{+0.222}_{-0.326}$	$[-0.597, 0.472]$
	fix others	$0.091^{+0.130}_{-0.079}$	$[-0.037, 0.352]$	$0.000^{+0.102}_{-0.114}$	$[-0.410, 0.314]$

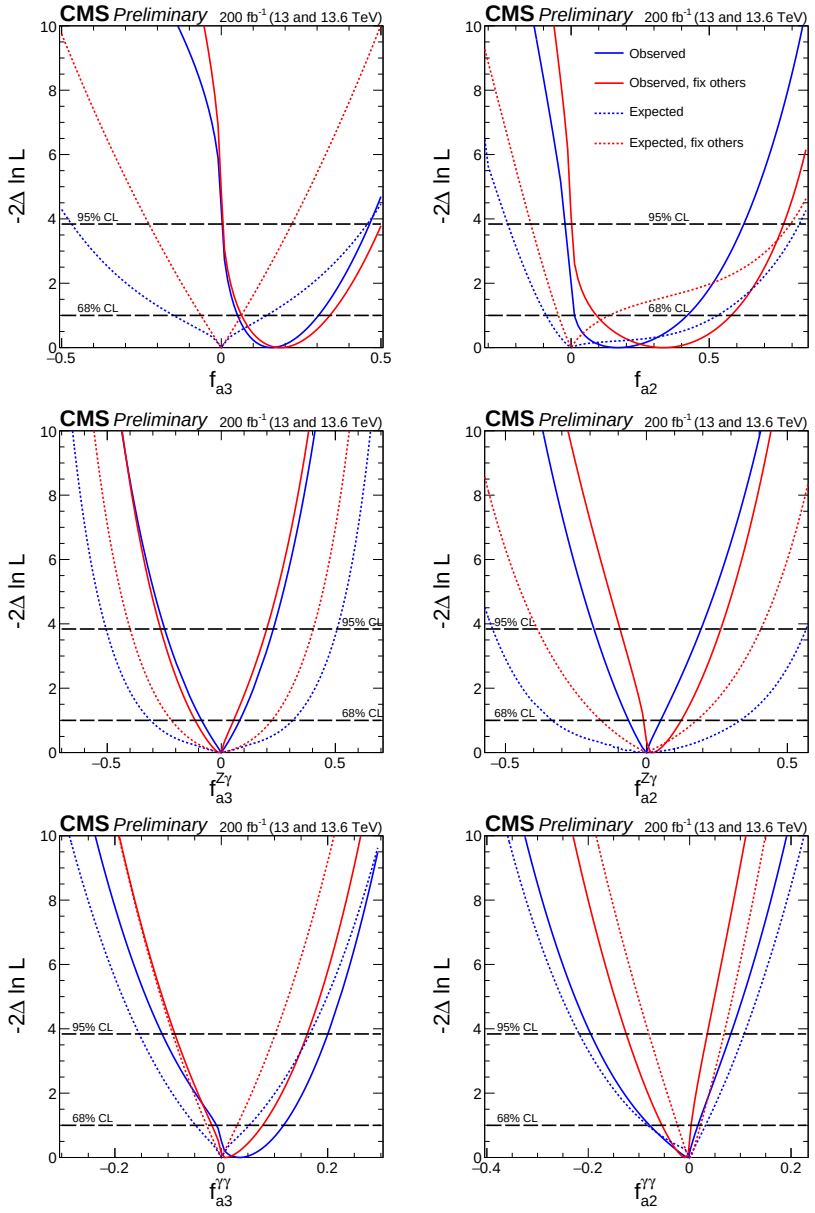

Figure 5.12: Observed (solid) and expected (dashed) likelihood scans of the fractional contribution for $\tilde{c}'_{zz}$ (top-left), c'_{zz} (top-right), $\tilde{c}'_{z\gamma}$ (middle-left), $c'_{z\gamma}$ (middle-right), $\tilde{c}'_{\gamma\gamma}$ (bottom-left), and $c'_{\gamma\gamma}$ (bottom-right). The results are presented for each coupling individually, with the remaining couplings either set to zero (red) or left unconstrained in the fit (blue). The dashed horizontal lines show the 68 and 95% CL exclusion regions.

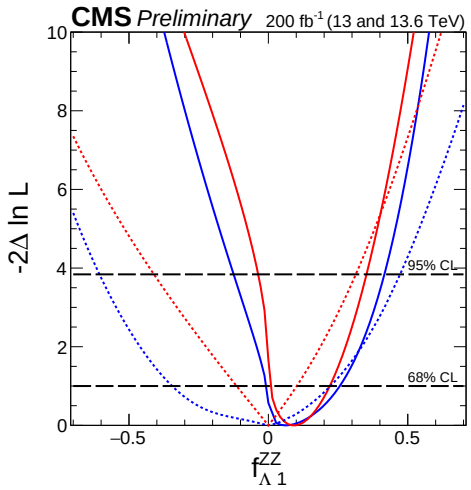

Figure 5.13: Observed (solid) and expected (dashed) likelihood scans of the fractional contribution for $c'_{z\Box}$. The conventions used in Fig. 5.12 have been adopted.

well-suited for EFT interpretation, no public data are available that enable constraints on the EFT operators using kinematic observables from the H $\to 4\ell$ decay.

Overall, the results are consistent with expectations from the SM. In specific instances, particularly f_{a3}, the data exclude the SM at the 95% CL. However, considering the large parameter space explored, such deviations remain statistically consistent with the SM when accounting for the relatively modest CL. This deviation is linked to a data asymmetry in $\mathcal{D}_{CP}$ illustrated in Fig. 5.11.

5.5 Permutation of identical leptons

Let us picture someone throwing two stones in opposite directions, and as they travel, each stone splits into two fragments. With four fragments in the air, we can clearly trace each one back to its original stone, an illustration of the classical physics view of the world, where objects have well-defined origins and trajectories. This is roughly

analogous to the decay $H \to Z_1 Z_2 \to (e^+e^-)(\mu^+\mu^-)$, where we know that the electron pair originated from one Z_1 boson and the muon pair from the other Z_2. However, when we consider the decay $H \to Z_1 Z_2 \to (\mu_1^+\mu_2^-)(\mu_3^+\mu_4^-)$, we can no longer definitively determine which muons originated from which Z boson. The other possibility is equally plausible $H \to Z_1' Z_2' \to (\mu_1^+\mu_4^-)(\mu_3^+\mu_2^-)$. We can certainly assign labels to the muons $(1, 2, 3, 4)$, as we detect them with high precision, but we cannot unambiguously identify which pair originated from which Z boson, this ambiguity is reflected in the two possible pairings: $Z_1 Z_2$ or $Z_1' Z_2'$.

This effect is known as the permutation of identical leptons and applies to both the $H \to 4e$ and $H \to 4\mu$ decay channels. This phenomenon is a manifestation of the entanglement when the state of one Z boson cannot be described independently of the state of another. This observation stands in stark contrast to the classical example of two stones breaking into fragments, as it entirely defies the classical understanding of the world. However, we can actually demonstrate the existence of this effect using our data. While we have accounted for this effect in all results derived from the data since observation of the Higgs boson, we have not formally shown its presence.

The permutation of identical leptons causes significant distortions in the observed distributions, such as m_1, m_2, $\cos\theta_1$, $\cos\theta_2$, and Φ. These distortions become evident when comparing the $H \to 2e2\mu$ decay to the 4e or 4μ decays, as well as in the relative event yields, which are affected by the constructive interference between the two amplitudes in the SM. In order to test the data for the presence of this entanglement effect, we can create a model alternative to the SM, where there is no permutation of identical leptons and no interference of the two amplitudes occurs. Ruling out such a

model in the data would offer a clear demonstration of entanglement.

5.5.1 Kinematic discriminants for permutation of identical leptons

The permutation of identical leptons causes significant distortions in the observed distributions, such as m_1, m_2, $\cos\theta_1$, $\cos\theta_2$, and Φ. These distortions become evident when comparing the H $\rightarrow$ 2e2μ decay to the 4e or 4μ decays, as well as in the event yields, which are affected by the constructive interference between the two amplitudes in the SM. In order to test the data, we create a model alternative to the SM, where there is no permutation of identical leptons and no interference of the two amplitudes occurs, using MELA tools. The MELA tools are used for both, creating an alternative sample of events with re-weighting, and to calculate an optimal

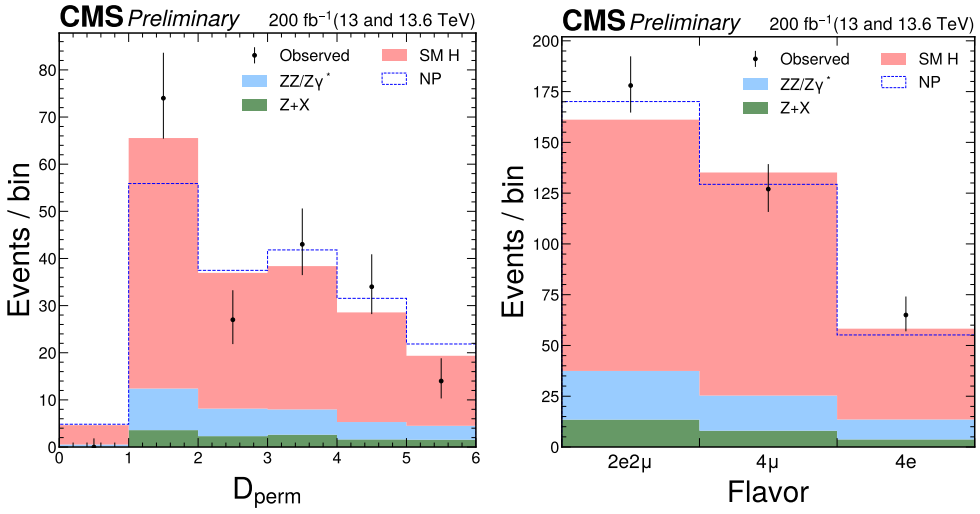

Figure 5.14: Event distribution as a function of the $\mathcal{D}_{\text{perm}}$ discriminant for H $\rightarrow$ 4e and 4μ events (left) and across the three lepton flavor categories 4e, 4μ, and 2e2μ (right). The blue open histogram corresponds to a hypothetical case in which no lepton permutation occurs. A selection of $\mathcal{D}_{\text{bkg}} > 0.6$ is applied to enhance signal-to-background discrimination.

discriminant $\mathcal{D}_{\text{perm}}$, following Eq. (5.1). Observable distributions for 4e and 4μ decays in which no permutation of leptons occurs is shown in Fig. 5.14.

In the SM, the permutation of identical leptons in 4e and 4μ decays leads to constructive interference between amplitudes, making the relative event yields across the three flavor categories sensitive to SM versus BSM effects. This sensitivity is particularly relevant for testing the lepton-permutation hypothesis, but also plays a role in EFT and polarization studies, where alternative models may predict different flavor compositions. Although the flavor category is technically not an explicit observable in the maximum likelihood fit, it effectively acts as one, since the information is encoded in the relative expected yields across the three categories. Figure 5.14 shows the relative yields of the flavor categories, including detector effects.

5.5.2 Results permutation of leptons

The hypothesis test for the presence or absence of permutation of identical leptons is primarily sensitive to the shape of the $\mathcal{D}_{\text{perm}}$ observable , although the relative yield difference in three flavor categories, arising from constructive interference between amplitudes involving permutations of identical leptons, also contributes some sensitivity. Both effects are illustrated in the observed data and expected model distributions shown in Fig. 5.14.

To distinguish between alternative models, the test statistic q is defined using the ratio of signal plus background likelihoods for two signal hypotheses. The likelihood is maximized with respect to the nuisance parameters which include the yields of signal and background processes and constrained parameters describing the systematic

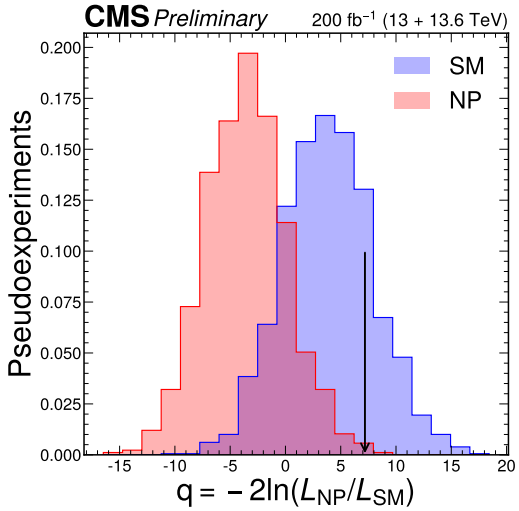

Figure 5.15: The observed value (q_{obs}, black arrow) and expected distributions of the test statistic q for the SM (blue) and the model with no permutation of leptons (NP, red) in the analysis of the H → ZZ → 4ℓ decays.

uncertainties. To quantify the consistency of the observed test statistic q_{obs} with the alternative signal hypothesis j, the probability $p = P(q \leq q_{obs} \,|\, \text{model } j + \text{bkg})$ is determined under the signal-plus-background hypothesis using pseudoexperiments. This probability is then translated into a Z-score, representing the number of standard deviations via the one-sided Gaussian tail integral.

The distribution of q for the SM and the alternative model without permutation of leptons is shown in Fig. 5.15. The numerical results are presented in Table 5.7. The expected separation is 1.9σ, and the observed value q_{obs} corresponds to a deviation of 2.7σ from the model with no permutation of leptons. The presence of permutation of leptons in the H → ZZ → 4μ and 4e decays is established at greater than 99% CL, in agreement with the SM and expectations from QM.

Table 5.7: The observed and average expected values of the p-value and the associated Z-score are shown for a model with no permutation of identical leptons (NP) in the decay $H \to ZZ \to 4\ell$ tested against the SM.

Model	Observed		Expected	
	p-value	Z-score	p-value	Z-score
NP	3.4×10^{-3}	2.7	2.8×10^{-2}	1.9
SM	0.21	0.8	0.5	0

5.6 Polarization

We analyze the $H \to ZZ$ average polarization states using two complementary approaches. In the first approach, we perform the angular analysis of the decay $H \to ZZ \to 4\ell$ to constrain simultaneously different spin polarization states with constraints on f_L and $f_\perp$. This enables a test for the presence of CP violation in the HZZ interactions, provided that $f_\perp$ deviates from zero. In this approach, we do not probe the coherence between different ZZ spin polarization states. Instead, we assume that the distribution of these states remains close to the SM prediction of $\mathcal{P}(m_1, m_2)$, as consistent with observation of the average mass distributions, allowing for significant interference effects.

In the second approach, we set $f_\perp = 0$, thereby assuming conservation of CP symmetry in the HZZ interactions. Given that no CP violation has been observed in any Higgs boson interactions to date [59, 60, 61, 62, 63, 64, 65, 66, 67, 68, 69, 70, 71, 72, 73, 74, 75, 76, 77, 77, 78], we assume CP conservation in pursuing the first complete determination of the polarization density matrix. In this scenario, all elements of the

polarization density matrix in Eq. (4.36) are real with $A_{++} = A_{--}$, leaving only two independent real parameters to be determined in experiment. The first parameter is f_L, and we define the other as a coherence parameter $C_\parallel$ to quantify the interference between the longitudinal and CP-even transverse polarization states:

$$-C_\parallel \sqrt{f_L(1-f_L)} = \int dm_1 dm_2 \, \mathcal{P}(m_1, m_2) \, \frac{A_\parallel(m_1, m_2) A_{00}(m_1, m_2)}{|A_\parallel|^2 + |A_{00}|^2} \,, \tag{5.9}$$

where the sign convention is chosen such that the coherence parameter $C_\parallel$ is positive in the SM. By definition, $C_\parallel$ is constrained to lie within the range -1 and $+1$. In the SM, $f_\perp^{\rm SM} = 0$, $f_L^{\rm SM} = 0.61$, and $C_\parallel^{\rm SM} = 0.91$, reflecting the fact that the longitudinal and CP-even transverse amplitudes are similar in magnitude, have opposite signs, and significantly overlap in mass, as evident from Eqs. (4.33) and (4.34). The values $C_\parallel = \pm 1$ represent complete coherence between the A_{00} and $A_\parallel$ amplitudes when they entirely overlap in mass while sharing identical mass distributions.

With the two parameters f_L and $C_\parallel$ defined in Eqs. (4.37) and (5.9), and under the assumption of CP symmetry conservation, the polarization density matrix is expressed

as follows:

$$\rho = \begin{pmatrix} 0 & 0 & 0 & 0 & 0 & 0 & 0 & 0 & 0 \\ 0 & 0 & 0 & 0 & 0 & 0 & 0 & 0 & 0 \\ 0 & 0 & (1-f_L)/2 & 0 & -C_\parallel\sqrt{f_L(1-f_L)/2} & 0 & (1-f_L)/2 & 0 & 0 \\ 0 & 0 & 0 & 0 & 0 & 0 & 0 & 0 & 0 \\ 0 & 0 & -C_\parallel\sqrt{f_L(1-f_L)/2} & 0 & f_L & 0 & -C_\parallel\sqrt{f_L(1-f_L)/2} & 0 & 0 \\ 0 & 0 & 0 & 0 & 0 & 0 & 0 & 0 & 0 \\ 0 & 0 & (1-f_L)/2 & 0 & -C_\parallel\sqrt{f_L(1-f_L)/2} & 0 & (1-f_L)/2 & 0 & 0 \\ 0 & 0 & 0 & 0 & 0 & 0 & 0 & 0 & 0 \\ 0 & 0 & 0 & 0 & 0 & 0 & 0 & 0 & 0 \end{pmatrix} \tag{5.10}$$

The simultaneous determination of the two parameters f_L and $C_\parallel$, and thus the full determination of the matrix in Eq. (5.10), is the goal of the second approach.

The angular distributions can be expressed as a function of three angular observables $\vec{x} = (\theta_1, \theta_2, \Phi)$, where Φ represents the angle between the two decay planes of the Z bosons, while θ_1 and θ_2 are two helicity angles in the Z boson decays [82, 83]. The diagram illustrating these kinematic observables is shown in Fig. 5.1. The angles θ^* and Φ_1 are defined in decay of the Higgs boson with respect to production axes and are therefore uniformly distributed for a spin-zero state.

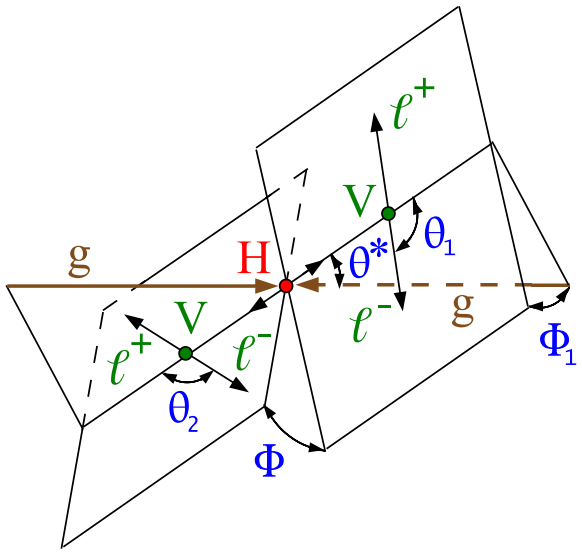

Figure 5.16: The diagram depicting the decay of the Higgs boson $gg \to H \to VV \to 4\ell$. The incoming particles are represented in brown, the intermediate vector bosons and their fermion decay products in green, the Higgs boson in red, and the angles in blue. The angles are defined in the respective rest frames of the particles [82, 83].

After integration over the masses, as indicated in Eqs. (4.37) and (5.9), and enforcing CP symmetry with $f_\perp = 0$, the angular distributions in the Higgs boson decay take the form [82, 83]

$$\begin{aligned}\frac{d\mathcal{P}(\cos\theta_1, \cos\theta_2, \Phi)}{d\cos\theta_1 d\cos\theta_2 d\Phi} &= f_L \times 4\sin^2\theta_1 \sin^2\theta_2 \\ &+(1-f_L)\times\left[\left(1+\cos^2\theta_1\right)\left(1+\cos^2\theta_2\right) + 4A_f^2\cos\theta_1\cos\theta_2 + \sin^2\theta_1\sin^2\theta_2\cos(2\Phi)\right] \\ &-C_\parallel\sqrt{f_L(1-f_L)/2}\times 8\left(\cos\theta_1\sin\theta_1\cos\theta_2\sin\theta_2\cos(\Phi) + A_f^2\sin\theta_1\sin\theta_2\cos(\Phi)\right),\end{aligned} \tag{5.11}$$

where $A_f \simeq 0.15$ is the small asymmetry parameter from $Z \to \ell^+\ell^-$ decays.

The first insight from Eq. (5.11) is that both parameters f_L and $C_\parallel$, fully describing the polarization density matrix in Eq. (5.10), can be derived from the three-dimensional

angular distributions, obtained by averaging over the mass distributions. Second, the term proportional to $C_{\parallel}$ reflects the interference between longitudinal and transverse polarization states, and it is essential to determine $C_{\parallel}$. Ultimately, a proper analysis must incorporate all the terms in Eq. (5.11) in order to place optimal constraints on the full matrix ρ, or on any of its components.

Although Eq. (5.11) does not account for detector effects, for permutations of identical leptons in the H $\rightarrow$ 4μ and 4e channels, for the terms associated with $f_{\perp} \neq 0$, or for the presence of backgrounds, we present it to highlight key features of the angular distributions. All of the aforementioned effects, which are absent in this formula, are fully incorporated in the analysis using the complete detector simulation discussed later. Rather than relying on analytical distributions, using templates of the angular observables that incorporate all relevant effects enables a proper and optimal likelihood-fit analysis.

5.6.1 Observables

The complete kinematic configuration of each Higgs boson decay event is characterized by three angles $(\theta_1, \theta_2, \Phi)$, as described in Section 5.6 and illustrated in Fig. 5.16, along with three invariant masses $(m_1, m_2, m_{4\ell})$ [82]. The production angles (θ^*, Φ_1) are uniformly distributed for all Higgs boson signal models but provide discrimination between signal and background. The reconstructed mass observables m_1, m_2, $m_{4\ell}$ are shown in Fig. 5.17, while the angular observables $\cos\theta_1$, $\cos\theta_2$, and Φ are shown in Fig. 5.18. The distribution of Φ is also shown with events assigned a weight of either $+1$ or -1, determined by the sign of $(\cos\theta_1 \cdot \cos\theta_2)$, which is necessary to illustrate the

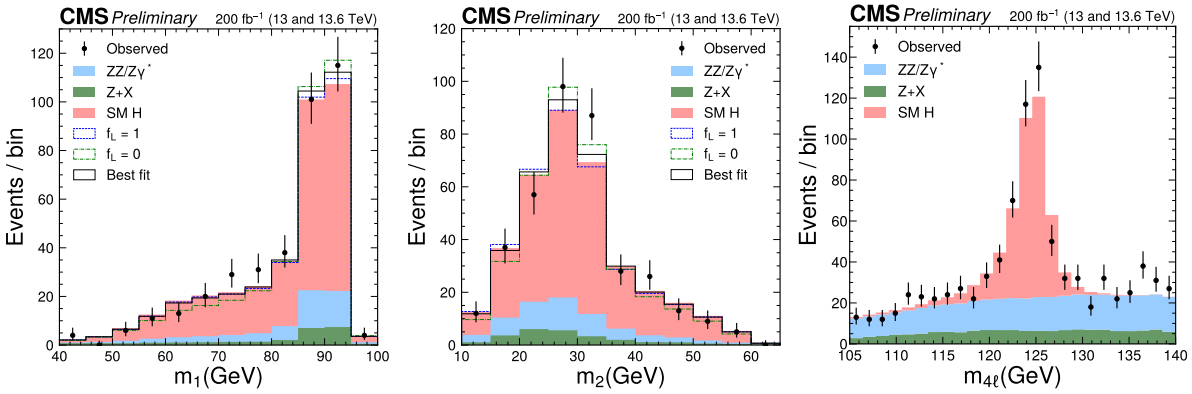

Figure 5.17: The distributions of m_1, m_2, and $m_{4\ell}$ in the decay H $\rightarrow$ ZZ $\rightarrow 4\ell$ are shown in comparison with the expected distributions from the SM (shaded red), purely longitudinal polarization of the Z bosons (dashed blue), or purely transverse polarization (dot-dashed green), all stacked on top of the background contributions (shaded blue and green). The best-fit distribution corresponds to results presented in Section 5.6.3 and Table 5.8 with $f_\perp$ and f_L unconstrained. A selection of $\mathcal{D}_{\text{bkg}} > 0.6$ is applied solely for visualization purposes, to enhance signal-to-background discrimination in the m_1 and m_2 plots, where $\mathcal{D}_{\text{bkg}}$ is introduced in Fig. 5.2 and text.

interference between the longitudinal and CP-even transverse components proportional to $\cos(\Phi)$ in Eq. (5.11).

The mass distributions m_1, m_2, $m_{4\ell}$ are not used directly in the fit, but are examined here to check for consistency with the data. Although the generated m_1 and m_2 distributions are constrained to be identical across all polarization scenarios in the 2e2μ final state, small differences are observed in the reconstructed m_1 and m_2 distributions in Fig. 5.18 for purely transversely polarized events, relative to those from the SM and longitudinally polarized scenarios. This is due to reconstruction effects with slightly different acceptance for extremely polarized events, and due to permutation of leptons in the 4e and 4μ channels. The angular distributions exhibit significant differences between polarization scenarios and are the focus of the

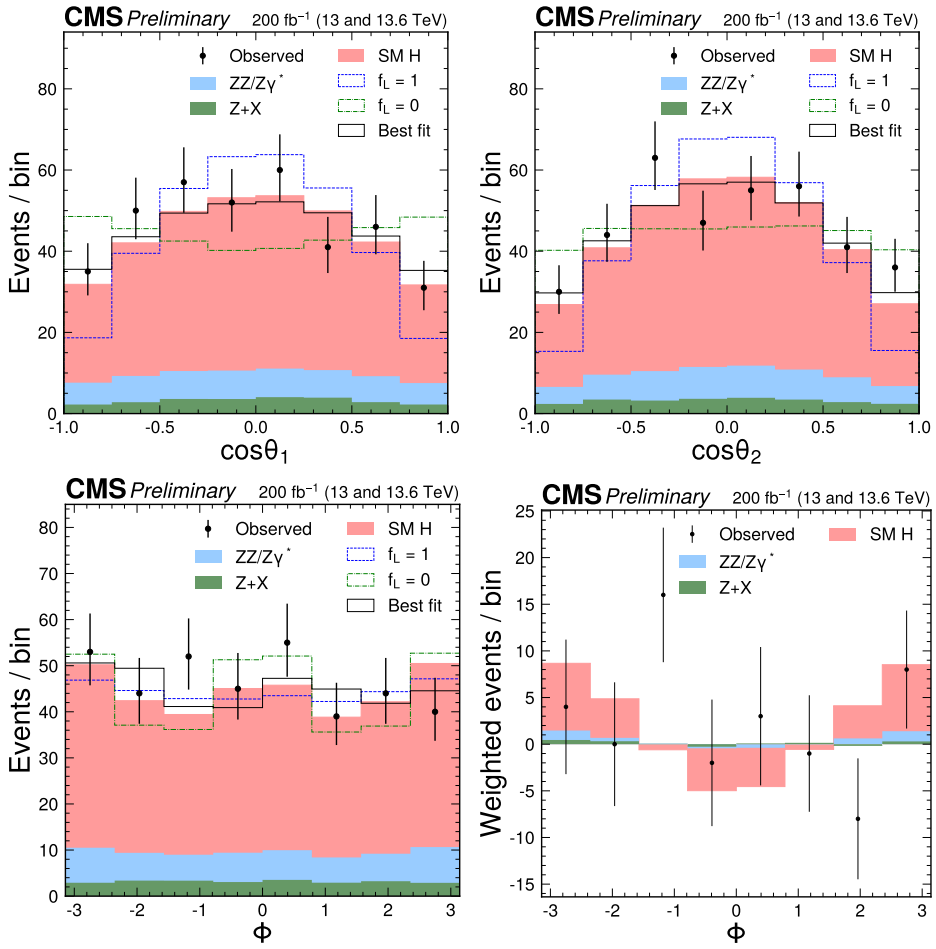

Figure 5.18: The distributions of $\cos\theta_1$, $\cos\theta_2$, and Φ are shown following the notation used in Fig. 5.17. The distribution of Φ is also shown with events assigned a weight of either $+1$ or -1, determined by the sign of $(\cos\theta_1 \cdot \cos\theta_2)$. A selection of $\mathcal{D}_{\text{bkg}} > 0.6$ is applied solely for visualization purposes, to enhance signal-to-background discrimination in the plots.

polarization analysis.

5.6.2 Statistical analysis of polarization fractions

The analysis of the fractions f_L and $f_\perp$, as well as $C_\parallel$, is performed using techniques similar to those described in the EFT framework in Section 5.4.2. Four observables $\vec{x} = (\mathcal{D}_{\text{bkg}}, \cos\theta_1, \cos\theta_2, \Phi)$ are used in all polarization fits, and the three flavor categories are separated. It is essential to eliminate the dependence on the m_1 and m_2 observables, since all polarization parameters are defined after integrating over these masses. Moreover, in order to avoid any second-order effects from the difference in the mass distributions, the m_1 and m_2 are ensured to be identical for any values of the f_L, $f_\perp$, or $C_\parallel$ parameters. This is trivial for $C_\parallel$ but not trivial for the other two parameters.

Therefore, a smooth analytical morphing of the model has been implemented which ensures that the mass distributions $\mathcal{P}(m_1, m_2)$, as introduced in Eq. (4.36), remains unchanged with polarization parameters through coupling constants $a_i^{\text{ZZ}}(m_1^2, m_2^2)$ in Eq. (4.1). In other words, for each set of values of f_L and $f_\perp$, the unique $a_i^{\text{ZZ}}(m_1^2, m_2^2)$ parameterization is employed which ensures consistency of the model. This model guarantees $f_L = 0.61$ and $f_\perp = 0$ for the SM. The templates for $\mathcal{P}_k^{\text{sig}}$ are constructed from simulated events based on this model.

5.6.3 Results CP violation and longitudinal polarization

Without assuming CP conservation, the polarization fit is carried out using two free parameters, f_L and $f_\perp$. The negative value of f_L or $f_\perp$ is a convention in these fits,

which reflects the sign of the $-A_{00}$ or $-iA_{\perp}$ amplitude, respectively, relative to the $A_{\parallel}$ amplitude. In this fit, amplitudes are smoothly interpolated between different f_L values in such a way that the m_1 and m_2 distributions in the H $\rightarrow$ ZZ $\rightarrow$ 2e2μ decay are preserved leading to strong coherence between the amplitudes, including large $C_{\parallel}$ values. As a result, the absolute values of $C_{\parallel}$, whose measurement is discussed in Section 5.6.4, is kept high and close to the SM prediction in these fits, which implies a large overlap of the transverse and longitudinal amplitudes in the (m_1, m_2) plane. These values of $C_{\parallel}$ are indicated by the dotted and dot-dashed lines in Fig 5.22.

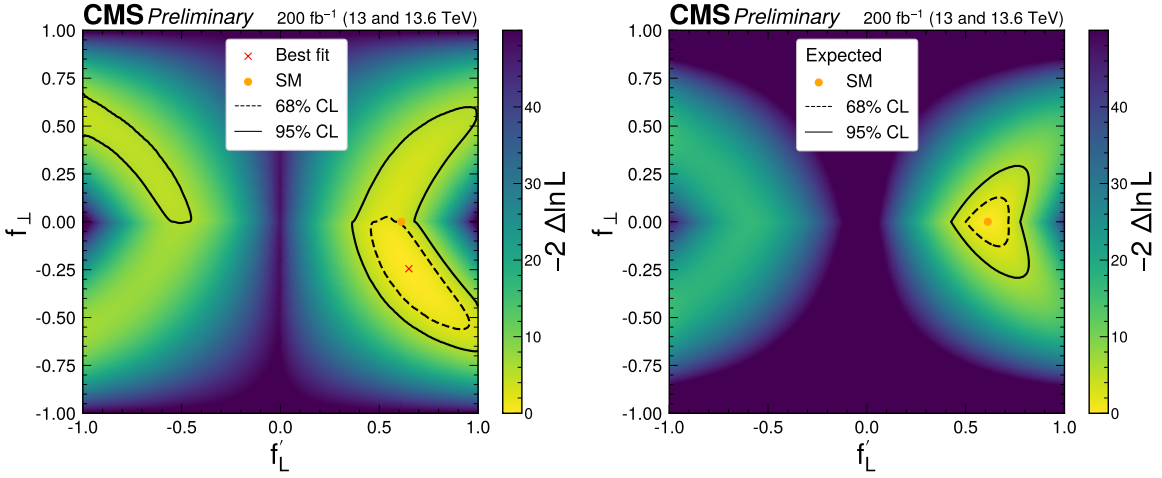

Figure 5.19: The observed (left) and expected (right) likelihood scans in the $(f'_L, f_{\perp})$ parameter plane, where $f'_L = f_L/(1 - |f_{\perp}|)$. The yellow point, corresponding to $f_L = 0.61$ and $f_{\perp} = 0$, represents the SM.

A transformation of parameters $f'_L = f_L/(1 - |f_{\perp}|)$ is convenient to perform a scan of a rectangular plane of two parameters, f'_L and $f_{\perp}$. This is shown in Fig. 5.19. The results for f_L and $f_{\perp}$ are shown in Fig. 5.20. The results of the one-dimensional scans of f_L for $f_{\perp}$ profiled and for $f_{\perp} = 0$, as well as of $f_{\perp}$ with f_L profiled, are shown in Fig. 5.21. The numerical results are shown in Table 5.8.

Both extreme points of polarization $f_L = 1$ (longitudinal) and $f_L = 0$ (transverse) are excluded at more than 6σ. The opposite-sign solution $f_L = -0.61$ is excluded at 2σ level, while the expectation is at more than 4σ. The reduced confidence level of excluding the opposite-sign solution is related to the observed data favoring a lower value of $C_\parallel$, as discussed in Section 5.6.4. This reduction is linked to a smaller asymmetry in $\cos\Phi$ modulation in data compared to expectation illustrated with weighted events in Fig. 5.18.

This measurement sets constraints on elements of the polarization density matrix in Eq. (4.36) without a restriction on CP properties, but assuming large coherence between the amplitudes. Overall, the results are consistent with expectations from the SM. The best-fit value of $(f_L, f_\perp)$ exhibits a deviation from the SM prediction in Fig. 5.20, though it remains consistent within approximately 1σ. This deviation is due to the lower values of both f_L and $f_\perp$ preferred by data. The lower value of f_L appears to be driven by the shape of the $\cos\theta_1$ and $\cos\theta_2$ distributions in Fig. 5.18. The negative value of $f_\perp$ can be attributed to a phase shift in the $\cos(2\Phi)$ component of the Φ distribution, as illustrated in Fig. 5.18. The two deviations are compatible with the SM within statistical uncertainties.

5.6.4 Results measurement of polarization density matrix

The measurement of the polarization density matrix under assumption of CP conservation requires setting constraints in the $(f_L, C_\parallel)$ parameter plane. This scan is shown in Fig. 5.22. The one-dimensional scans of f_L and $C_\parallel$ with the other parameter profiled are shown in Fig. 5.23. The numerical results are shown in Table 5.8.

Table 5.8: Observed and expected constraints on f_L, $f_\perp$, and $C_\parallel$ in three fitting scenarios. The three f_L measurements are reported with either $f_\perp$ or $C_\parallel$ profiled in the fits corresponding to Figs. 5.19 or 5.22, respectively, or with both fixed as indicated in the second column. The $f_\perp$ and $C_\parallel$ results are presented with f_L profiled in the corresponding fits. The reported correlation coefficients correspond to the observed / average expected values in the SM.

$\vec{f}$	Correlation	Observed		Expected	
	obs. / exp.	68% CL	95% CL	68% CL	95% CL
f_L	$-0.268/+0.001$	$0.49^{+0.08}_{-0.07}$	$[-0.48,-0.40]\cup[0.34,0.64]$	0.61 ± 0.07	$[0.47,0.74]$
$f_\perp$		$0.25^{+0.21}_{-0.22}$	$[-0.62,0.40]\cup[0.52,0.60]$	0.00 ± 0.06	$[-0.20,0.20]$
f_L	fix $f_\perp$ & $C_\parallel$	$0.52^{+0.08}_{-0.06}$	$[0.38,0.67]$	0.61 ± 0.07	$[0.47,0.74]$
f_L	$+0.069/+0.054$	$0.53^{+0.06}_{-0.07}$	$[0.38,0.66]$	0.61 ± 0.07	$[0.47,0.74]$
$C_\parallel$		$0.19^{+0.46}_{-0.45}$	$[-0.68,1.00]$	$0.91^{+0.09}_{-0.47}$	$[0.00,1.00]$

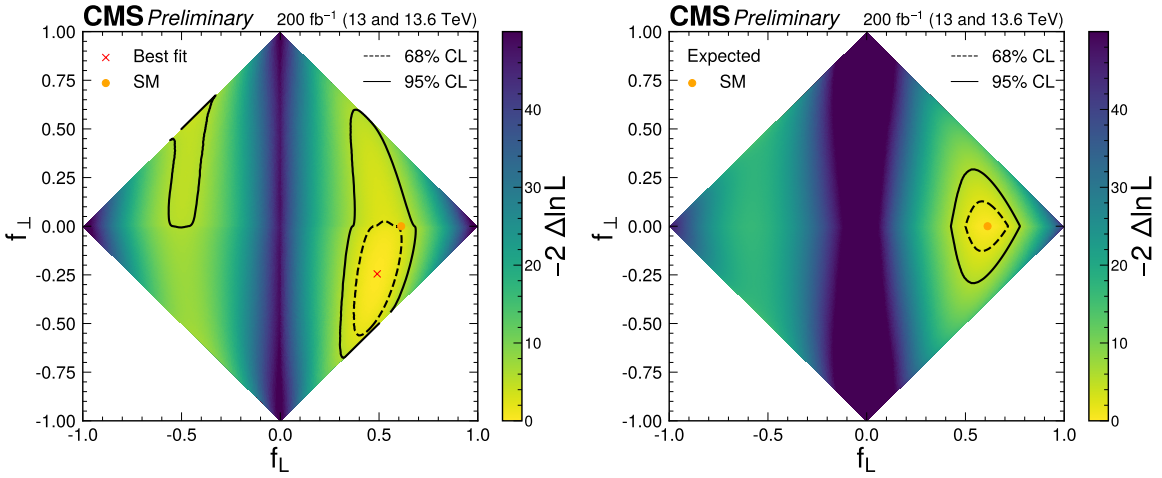

Figure 5.20: The observed (left) and expected (right) likelihood scans in the $(f_L, f_\perp)$ parameter plane, which are equivalent to scans in Fig. 5.19.

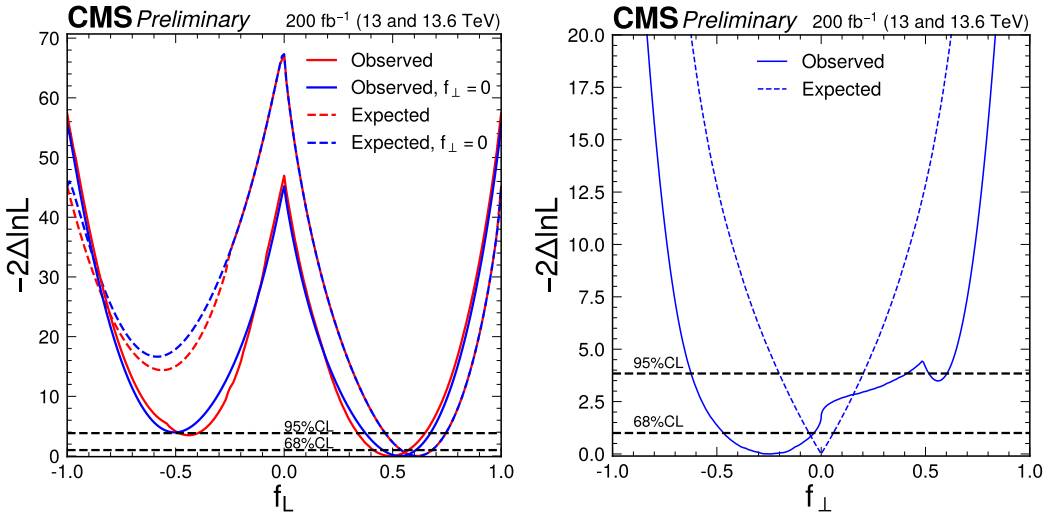

Figure 5.21: The observed (solid) and expected (dashed) likelihood scans of f_L (left) and $f_\perp$ (right). The f_L scan corresponds to either $f_\perp$ profiled (red) or $f_\perp = 0$ (blue) in Fig. 5.19. The $f_\perp$ scan is performed with the f'_L profiled in Fig. 5.19. The expectation corresponds to the SM scenario $f_L = 0.61$ and $f_\perp = 0$.

There is a noticeable deviation of the best-fit value of $C_{\parallel}$ to the lower values compared to the expected value $C_{\parallel} = 0.91$ in the SM. This fluctuation can be traced to the observed data distribution in the asymmetry plot of the angle Φ shown in Fig. 5.18. The asymmetry with the $-\cos(\Phi)$ modulation is clearly visible in the expected SM distribution, which reflects the interference between the longitudinal and CP-even transverse components. However, observed data favors a flat distribution with no asymmetry, resulting in the most likely $C_{\parallel}$ value close to zero. Nonetheless, within statistical uncertainties, all results are consistent with the SM.

In Fig. 5.23, the dotted line, which passes through the SM point, and its mirror line across the $C_{\parallel} = 0$ axis shown as dot-dashed, represent the values of $C_{\parallel}$ used in the model considered in Section 5.6.3 with smoothly interpolated amplitudes between different f_L values. The scan of f_L along these lines corresponds to the f_L scan in Fig. 5.21 (left).

Results of the fits in Fig. 5.22 can be converted into constraints on the elements of the polarization density matrix ρ in Eq. (5.10). Overall, the results are consistent with expectations from the SM. The best-fit value of $(f_L, C_{\parallel})$ exhibits a deviation from the SM prediction in Fig. 5.22, though it remains consistent within approximately 1σ. This deviation is primarily due to the lower value of $C_{\parallel}$ preferred by data and is linked to a smaller asymmetry in $\cos\Phi$ modulation in data compared to SM expectation illustrated with weighted events in Fig. 5.18. The implications of these measurements for studies of quantum entanglement are presented in Section 5.6.5.

5.6.5 Implications for quantum entanglement and Bell-type inequalities

The test for quantum entanglement and conditions for violation of the Bell-type inequality can be performed under assumption of CP conservation, that is $f_\perp = 0$. We consider two scenarios: In one approach ($C_\parallel$ constrained), we consider the values of $C_\parallel$ shown as dotted and dot-dashed lines in Fig. 5.22, that is assuming that (m_1, m_2) distributions for transverse and longitudinal amplitudes overlap substantially. In the second approach ($C_\parallel$ unconstrained), we perform an interpretation without such a constraint, using full two-dimensional constraints in the $(f_L, C_\parallel)$ plane shown in Fig. 5.22. As discussed in Section 4.8.2, we cannot directly demonstrate non-locality or distinguishing entanglement from non-entanglement in our experiment. However,

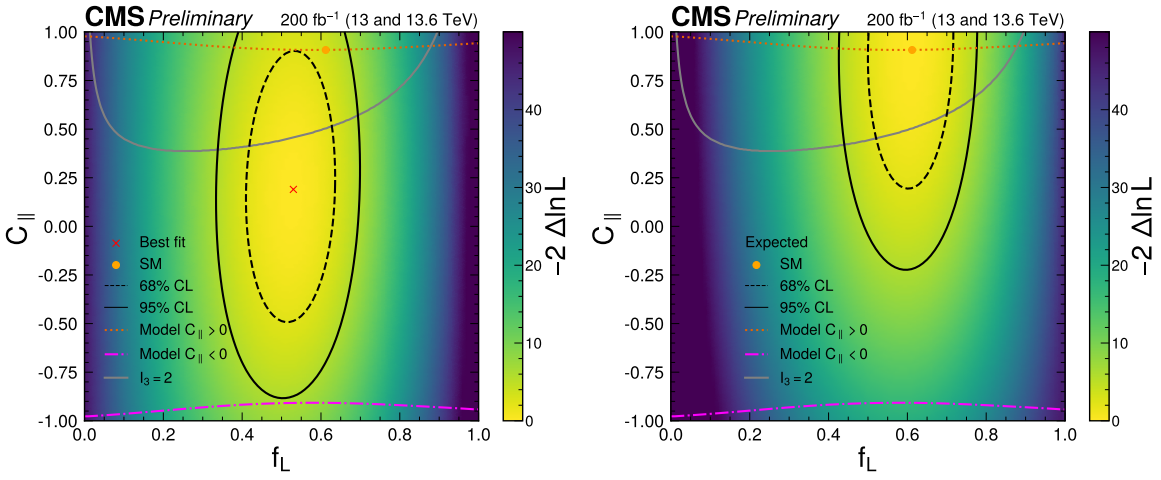

Figure 5.22: The observed (left) and expected (right) likelihood scans in the $(f_L, C_\parallel)$ parameter plane. The yellow point, corresponding to $f_L = 0.61$ and $C_\parallel = 0.91$, represents the SM. The dotted line passing through the SM point indicates the values of $C_\parallel$ associated with a model of smoothly interpolated amplitudes between different f_L values resulting in strong coherence between the transverse and longitudinal amplitudes. The dot-dashed line shows the corresponding values for negative $C_\parallel$. The grey curve represents the case $I_3 = 2$, with points above this curve corresponding to $I_3 > 2$, while points below correspond to $I_3 < 2$.

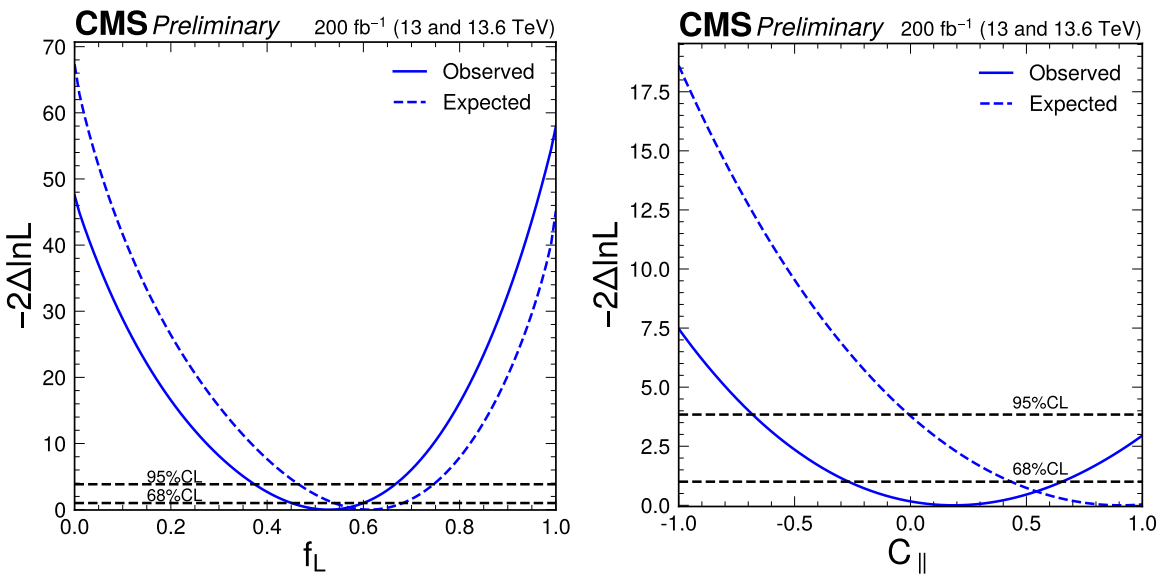

Figure 5.23: The observed (solid) and expected (dashed) likelihood scan of f_L with $C_{\|}$ profiled (left) and $C_{\|}$ with f_L profiled (right), both from the fit corresponding to Fig. 5.22 with expectation corresponding to the SM scenario with $f_L = 0.61$ and $C_{\|} = 0.91$.

we can test if conditions exist for those measurements.

Table 5.9: Observed and expected constraints on the parameter I_3 are shown for two scenarios: one where $|C_{\|}|$ is fixed at large values for each value of f_L, reflecting smoothly varying amplitudes across different f_L values, and another where both f_L and $C_{\|}$ are profiled.

Parameter	Scenario	Observed		Expected	
		68% CL	95% CL	68% CL	95% CL
I_3	fix $C_{\|}$	$2.69^{+0.03}_{-0.08}$	$[2.52, 2.75]$	2.60 ± 0.08	$[2.39, 2.71]$
I_3	float all	$1.60^{+0.70}_{-0.68}$	$[0.28, 2.87]$	$2.60^{+0.21}_{-0.68}$	$[1.26, 2.87]$

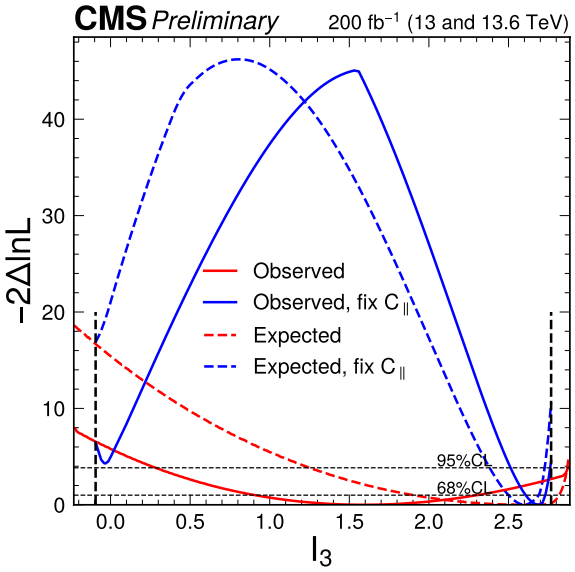

Figure 5.24: Observed (solid) and expected (dashed) likelihood scans of I_3 in two scenarios, with $|C_\parallel|$ fixed to large values (blue) and with both f_L and $C_\parallel$ unconstrained (red).

There is a unique I_3 value associated with every $(f_L, C_\parallel)$ coordinate in Fig. 5.22, and the I_3 values are bounded in the range $-0.23 < I_3 < 2.88$. When the $C_\parallel$ are constrained to the dotted and dot-dashed lines in Fig. 5.22, the I_3 values are further bounded within $-0.09 < I_3 < 2.77$. The likelihood value at each point $(f_L, C_\parallel)$ in Fig. 5.22 can be projected onto the I_3 parameter, and the corresponding constraints are presented in Fig. 5.24 in both scenarios. This interpretation of the data is presented in Table 5.9.

As shown in Fig. 5.22, there exists a region in the two-dimensional plane where $I_3 > 2$, which includes the SM point. In the first approach, where $|C_\parallel|$ is constrained to large values, it is experimentally established that $I_3 > 2$ at 95% CL. Therefore, under the assumption of QM, CP conservation, and large coherence of the transverse and

longitudinal amplitudes, it has been established that conditions exist for measuring violation of the Bell-type inequality in the H $\to$ ZZ decays.

In contrast, the second approach allows $C_{\|}$ to vary freely, resulting in a best-fit value that lies in the $I_3 < 2$ region, while the SM values of $(f_L, C_{\|})$ remain in the $I_3 > 2$ region. Nonetheless, the data remain statistically consistent with both the SM values and with alternative values lying outside the $I_3 > 2$ region. Therefore, in this scenario, it is not possible yet to establish experimentally that $I_3 > 2$ and that conditions exist for measuring violation of the Bell-type inequality in the H $\to$ ZZ decays.

Under any scenario, the exclusion of $f_L = 0$ and $f_L = 1$ is at more than 6σ, as shown in Figs. 5.21 and 5.23. This establishes it unambiguously that the two Z bosons in the H $\to$ ZZ decay are in an entangled state and represent the qutrits. This conclusion is drawn under the assumption of the validity of QM and CP conservation, and therefore does not constitute a general test of non-entanglement.

5.7 Other analysis

The techniques described in this chapter, as well as in Chapter. 4 have also resulted in meaningful contributions to CMS analyses in which I was not a primary analyzer. For example, techniques for phenomenological calculations that I performed in 5.3, have been utilized in off-shell H* $\to 4\ell$ analysis. In this analysis, the restrictions on $\kappa_z < 1$ can be relaxed, resulting in a more general constraint on the light Yukawa couplings.

As a developer of JHUGen, I have implemented many new features that made certain analysis on CMS possible. I integrated the one- and two-loop corrections of $\mathcal{O}(\lambda)$

into the Higgs boson production and decay processes as described in [191]. This allows users to simulate the effect of anomalous Higgs boson trilinear couplings in the $gg \to \mathrm{H} \to 4\ell$ and $VV \to \mathrm{H} \to 4\ell$ channels, including its interference with the background continuum processes. More importantly, incorporating this new process into MELA allowed the reweighting of previously produced $\mathrm{H} \to 4\ell$ samples to any value of λ and even the construction of optimal discriminants to separate SM from anomalous $\lambda \neq 1$. My developments are currently being used in an analysis using off-shell $pp \to H^* \to 4\ell$ events to place the first indirect limits on the Higgs boson trilinear coupling in the off-shell region.

In another instance, my developments have had impacts on analysis outside the field of Higgs physics. The features that I incorporated into JHUGEN and MELA made the spin parity analysis of a recently discovered all-charm tetraquark candidate possible. This candidate was observed decaying to $J/\psi J/\psi \to 4\mu$. Qualitatively, this looks very similar to $X \to \mathrm{ZZ}$ decays, where X is some arbitrary resonance with integer spin. I added new features to JHUGEN and MELA that would allow users to modify the Z couplings to fermions, and its mass and width scheme to correctly model $J/\psi \to 2\mu$ decay. Optimal MELA based discriminants were then used to exclude or constrain various spin-parity hypotheses. My contributions to both JHUGEN and MELA were used to show for the first time that the favored quantum numbers of the tetraquark candidate are $J^{pc} = 2^{++}$ [192].

Chapter 6
Conclusion

This thesis presents the results of several analysis of the Higgs Boson properties. Kinematic effects in the Higgs boson decay to four leptons $H \to 4\ell$ have been studied using full detector simulation and matrix element techniques, optimizing sensitivity to the tensor structure of Higgs boson interactions and spin correlations in the decay process. A simultaneous measurement of eight Higgs boson couplings to electroweak vector bosons has been carried out within the frameworks of anomalous couplings and effective field theory. We also performed a search for γH production and placed simultaneous constraints on four anomalous couplings involving anomalous couplings to photons. We also interpret the production rate for $H \to 4\ell$ in terms of the Yukawa couplings between light quarks and the Higgs boson, excluding the hypothesis that up- or down-type quarks in the first or second generation have the same Yukawa couplings as those in the third generation is excluded with a CL greater than 95%.

A natural extension of the work presented in this thesis is the targeted analysis of other Higgs production modes, such as VH and VBF in the EFT fits. Doing so would place better constraints on certain operators and allow us to constrain the absolute EFT couplings values rather than the coupling ratios. The ultimate goal of this work is to produce a combined fit for all EFT couplings in the four-lepton final state at CMS. This would include information from the off-shell Higgs analysis to constrain the width as well and incorporate EFT effects in the continuum background and would be the most complete picture of Higgs in the EFT framework. Ideally, these results would

be combined into a global fit with other Higgs decay channels and perhaps including data from ATLAS. We also expect improvements as more data is collected at the LHC. HL-LHC which is expected to come online in the early 2030's will produce 3000 fb^{-1} of data by the end of its life cycle. Perhaps this increase in statistics will finally reveal deviations from the SM Higgs couplings and provide us with a hint about where to look next.

Bibliographic references

[1] Mary K. Gaillard, Paul D. Grannis, and Frank J. Sciulli. "The Standard model of particle physics." In: *Rev. Mod. Phys.* 71 (1999), S96–S111. DOI: 10.1103/RevModPhys.71.S96. arXiv: hep-ph/9812285.

[2] Serguei Chatrchyan et al. "Observation of a new boson at a mass of 125 GeV with the CMS experiment at the LHC." In: *Phys. Lett. B* 716 (2012), p. 30. DOI: 10.1016/j.physletb.2012.08.021. arXiv: 1207.7235 [hep-ex].

[3] Sally Dawson et al. "Report of the Topical Group on Higgs Physics for Snowmass 2021: The Case for Precision Higgs Physics." In: *Snowmass 2021*. 2022. arXiv: 2209.07510 [hep-ph].

[4] Emmy Noether. "Invariant Variation Problems." In: *Gott. Nachr.* 1918 (1918), pp. 235–257. DOI: 10.1080/00411457108231446. arXiv: physics/0503066.

[5] Eric Drexler. *Elementary particle interactions in the Standard Model*. Accessed: 2025-10-15.

[6] C. S. Wu, E. Ambler, R. W. Hayward, D. D. Hoppes, and R. P. Hudson. "Experimental Test of Parity Conservation in β Decay." In: *Phys. Rev.* 105 (1957), pp. 1413–1414. DOI: 10.1103/PhysRev.105.1413.

[7] S. L. Glashow. "Partial Symmetries of Weak Interactions." In: *Nucl. Phys.* 22 (1961), pp. 579–588. DOI: 10.1016/0029-5582(61)90469-2.

[8] Steven Weinberg. "A Model of Leptons." In: *Phys. Rev. Lett.* 19 (1967), pp. 1264–1266. DOI: 10.1103/PhysRevLett.19.1264.

[9] Abdus Salam. "Weak and electromagnetic interactions." In: *Elementary particle physics: relativistic groups and analyticity*. Ed. by Nils Svartholm. Proceedings of the eighth Nobel symposium. Stockholm: Almqvist & Wiksell, 1968, p. 367.

[10] Murray Gell-Mann. "A Schematic Model of Baryons and Mesons." In: *Phys. Lett.* 8 (1964), pp. 214–215. DOI: 10.1016/S0031-9163(64)92001-3.

[11] H. L. Anderson, E. Fermi, E. A. Long, and D. E. Nagle. "Total Cross-sections of Positive Pions in Hydrogen." In: *Phys. Rev.* 85 (1952), p. 936. DOI: 10.1103/PhysRev.85.936.

[12] M. Y. Han and Yoichiro Nambu. "Three Triplet Model with Double SU(3) Symmetry." In: *Phys. Rev.* 139 (1965). Ed. by T. Eguchi, B1006–B1010. DOI: 10.1103/PhysRev.139.B1006.

[13] Elliott D. Bloom et al. "High-Energy Inelastic e p Scattering at 6-Degrees and 10-Degrees." In: *Phys. Rev. Lett.* 23 (1969), pp. 930–934. DOI: 10.1103/PhysRevLett.23.930.

[14] David J. Gross and Frank Wilczek. "Ultraviolet Behavior of Nonabelian Gauge Theories." In: *Phys. Rev. Lett.* 30 (1973). Ed. by J. C. Taylor, pp. 1343–1346. DOI: 10.1103/PhysRevLett.30.1343.

[15] P. Nason. "Introduction to QCD." In: *Conf. Proc. C* 9705251 (1997). Ed. by N. Ellis and M. Neubert, pp. 94–149.

[16] F. Englert and R. Brout. "Broken Symmetry and the Mass of Gauge Vector Mesons." In: *Phys. Rev. Lett.* 13 (1964). Ed. by J. C. Taylor, pp. 321–323. DOI: 10.1103/PhysRevLett.13.321.

[17] Peter W. Higgs. "Broken Symmetries and the Masses of Gauge Bosons." In: *Phys. Rev. Lett.* 13 (1964). Ed. by J. C. Taylor, pp. 508–509. DOI: 10.1103/PhysRevLett.13.508.

[18] J. Goldstone. "Field Theories with Superconductor Solutions." In: *Nuovo Cim.* 19 (1961), pp. 154–164. DOI: 10.1007/BF02812722.

[19] Jeffrey Goldstone, Abdus Salam, and Steven Weinberg. "Broken Symmetries." In: *Phys. Rev.* 127 (1962), pp. 965–970. DOI: 10.1103/PhysRev.127.965.

[20] Ian Low and Aneesh V. Manohar. "Spontaneously broken space-time symmetries and Goldstone's theorem." In: *Phys. Rev. Lett.* 88 (2002), p. 101602. DOI: 10.1103/PhysRevLett.88.101602. arXiv: hep-th/0110285.

[21] Makoto Kobayashi and Toshihide Maskawa. "CP Violation in the Renormalizable Theory of Weak Interaction." In: *Prog. Theor. Phys.* 49 (1973), pp. 652–657. DOI: 10.1143/PTP.49.652.

[22] A. D. Sakharov. "Violation of CP Invariance, C asymmetry, and baryon asymmetry of the universe." In: *Pisma Zh. Eksp. Teor. Fiz.* 5 (1967), pp. 32–35. DOI: 10.1070/PU1991v034n05ABEH002497.

[23] Q. R. Ahmad et al. "Direct evidence for neutrino flavor transformation from neutral current interactions in the Sudbury Neutrino Observatory." In: *Phys. Rev. Lett.* 89 (2002), p. 011301. DOI: 10.1103/PhysRevLett.89.011301. arXiv: nucl-ex/0204008.

[24] M. C. Gonzalez-Garcia and Michele Maltoni. "Phenomenology with Massive Neutrinos." In: *Phys. Rept.* 460 (2008), pp. 1–129. DOI: 10.1016/j.physrep.2007.12.004. arXiv: 0704.1800 [hep-ph].

[25] Edward Witten. "Dynamical Breaking of Supersymmetry." In: *Nucl. Phys. B* 188 (1981), p. 513. DOI: 10.1016/0550-3213(81)90006-7.

[26] N. Sakai. "Naturalness in Supersymmetric Guts." In: *Z. Phys. C* 11 (1981), p. 153. DOI: 10.1007/BF01573998.

[27] Jerome Martin. "Everything You Always Wanted To Know About The Cosmological Constant Problem (But Were Afraid To Ask)." In: *Comptes Rendus Physique* 13 (2012), pp. 566–665. DOI: 10.1016/j.crhy.2012.04.008. arXiv: 1205.3365 [astro-ph.CO].

[28] Michela D'Onofrio and Kari Rummukainen. "Standard model cross-over on the lattice." In: *Phys. Rev. D* 93.2 (2016), p. 025003. DOI: 10.1103/PhysRevD.93.025003. arXiv: 1508.07161 [hep-ph].

[29] Chris Llewellyn Smith. "Genesis of the Large Hadron Collider." In: *Phil. Trans. Roy. Soc. Lond. A* 373.2032 (2014), p. 20140037. DOI: 10.1098/rsta.2014.0037.

[30] "Proceedings, ECFA-CERN Workshop on large hadron collider in the LEP tunnel: Lausanne and Geneva, Switzerland, March 21-27 March, 1984." In: (1984). Ed. by M. Jacob. DOI: 10.5170/CERN-1984-010-V-2.

[31] M. Della Negra et al. "CMS: The Compact Muon Solenoid: Letter of intent for a general purpose detector at the LHC." In: (1992).

[32] S. Chatrchyan et al. "The CMS experiment at the CERN LHC." In: *JINST* 3 (2008), S08004. DOI: 10.1088/1748-0221/3/08/S08004.

[33] W. Adam et al. "The CMS Phase-1 Pixel Detector Upgrade." In: *JINST* 16 (2021), P02027. DOI: 10.1088/1748-0221/16/02/P02027. arXiv: 2012.14304 [physics.ins-det].

[34] CMS Collaboration. *CMS detector design*. Accessed: 2025-10-15.

[35] "The CMS electromagnetic calorimeter project: Technical Design Report." In: (1997).

[36] "The CMS hadron calorimeter project: Technical Design Report." In: (1997).

[37] A. M. Sirunyan et al. "Performance of the CMS muon detector and muon reconstruction with proton-proton collisions at $\sqrt{s} = 13$ TeV." In: *JINST* 13.06 (2018), P06015. DOI: 10.1088/1748-0221/13/06/P06015. arXiv: 1804.04528 [physics.ins-det].

[38] Albert M Sirunyan et al. "Performance of the CMS Level-1 trigger in proton-proton collisions at $\sqrt{s} = 13$ TeV." In: *JINST* 15 (2020), P10017. DOI: 10.1088/1748-0221/15/10/P10017. arXiv: 2006.10165 [hep-ex].

[39] Vardan Khachatryan et al. "The CMS trigger system." In: *JINST* 12 (2017), P01020. DOI: 10.1088/1748-0221/12/01/P01020. arXiv: 1609.02366 [physics.ins-det].

[40] A. Hayrapetyan et al. "Performance of the CMS high-level trigger during LHC Run 2." In: *JINST* 19.11 (2024), P11021. DOI: 10.1088/1748-0221/19/11/P11021. arXiv: 2410.17038 [physics.ins-det].

[41] A. M. Sirunyan et al. "Particle-flow reconstruction and global event description with the cms detector." In: *JINST* 12 (2017), P10003. DOI: 10.1088/1748-0221/12/10/P10003. arXiv: 1706.04965 [physics.ins-det].

[42] Matteo Cacciari, Gavin P. Salam, and Gregory Soyez. "The anti-k_{T} jet clustering algorithm." In: *JHEP* 04 (2008), p. 063. DOI: 10.1088/1126-6708/2008/04/063. arXiv: 0802.1189 [hep-ex].

[43] Matteo Cacciari, Gavin P. Salam, and Gregory Soyez. "FastJet user manual." In: *Eur. Phys. J. C* 72 (2012), p. 1896. DOI: 10.1140/epjc/s10052-012-1896-2. arXiv: 1111.6097 [hep-ph].

[44] Vardan Khachatryan et al. "Jet energy scale and resolution in the CMS experiment in pp collisions at 8 TeV." In: *JINST* 12 (2017), P02014. DOI: 10.1088/1748-0221/12/02/P02014. arXiv: 1607.03663 [hep-ex].

[45] Serguei Chatrchyan et al. "Description and Performance of Track and Primary-Vertex Reconstruction with the CMS Tracker." In: *JINST* 9.10 (2014), P10009. DOI: 10.1088/1748-0221/9/10/P10009. arXiv: 1405.6569 [physics.ins-det].

[46] V. Karimaki, A. Heikkinen, T. Lampen, and T. Linden. "Sensor alignment by tracks." In: *13th International Conference on Computing in High-Enery and Nuclear Physics (CHEP 2003)*. [eConf C0303241, TULT008]. 2003. arXiv: physics/0306034 [physics].

[47] CMS Collaboration. *The HIP algorithm for track based alignment and its application to the CMS pixel detector*. CMS Note CMS-NOTE-2006-018. 2006.

[48] David Nathan Brown, A. V. Gritsan, Z. J. Guo, and D. Roberts. "Local alignment of the BABAR silicon vertex tracking detector." In: *Nucl. Instrum. Meth. A* 603 (2009), p. 467. DOI: 10.1016/j.nima.2009.02.001. arXiv: 0809.3823 [physics.ins-det].

[49] W. Adam et al. "Alignment of the CMS silicon strip tracker during stand-alone commissioning." In: *JINST* 4 (2009), T07001. DOI: 10.1088/1748-0221/4/07/T07001. arXiv: 0904.1220 [physics.ins-det].

[50] S Chatrchyan et al. "Alignment of the CMS silicon tracker during commissioning with cosmic rays." In: *JINST* 5 (2010), T03009. DOI: 10.1088/1748-0221/5/03/T03009. arXiv: 0910.2505 [physics.ins-det].

[51] Serguei Chatrchyan et al. "Alignment of the CMS tracker with LHC and cosmic ray data." In: *JINST* 9 (2014), P06009. DOI: 10.1088/1748-0221/9/06/P06009. arXiv: 1403.2286 [physics.ins-det].

[52] Albert M Sirunyan et al. "Precision measurement of the structure of the CMS inner tracking system using nuclear interactions." In: *JINST* 13 (2018), P10034. DOI: 10.1088/1748-0221/13/10/P10034. arXiv: 1807.03289 [physics.ins-det].

[53] Georges Aad et al. "Observation of a new particle in the search for the Standard Model Higgs boson with the ATLAS detector at the LHC." In: *Phys. Lett.*

B 716 (2012), p. 1. DOI: 10.1016/j.physletb.2012.08.020. arXiv: 1207.7214 [hep-ex].

[54] Serguei Chatrchyan et al. "Observation of a new boson with mass near 125 GeV in pp collisions at $\sqrt{s} = 7$ and 8 TeV." In: *JHEP* 06 (2013), p. 081. DOI: 10.1007/JHEP06(2013)081. arXiv: 1303.4571 [hep-ex].

[55] S. L. Glashow. "Partial-symmetries of weak interactions." In: *Nucl. Phys.* 22 (1961), p. 579. DOI: 10.1016/0029-5582(61)90469-2.

[56] Peter W. Higgs. "Broken symmetries, massless particles and gauge fields." In: *Phys. Lett.* 12 (1964), p. 132. DOI: 10.1016/0031-9163(64)91136-9.

[57] G. S. Guralnik, C. R. Hagen, and T. W. B. Kibble. "Global conservation laws and massless particles." In: *Phys. Rev. Lett.* 13 (1964), p. 585. DOI: 10.1103/PhysRevLett.13.585.

[58] Steven Weinberg. "A model of leptons." In: *Phys. Rev. Lett.* 19 (1967), p. 1264. DOI: 10.1103/PhysRevLett.19.1264.

[59] Serguei Chatrchyan et al. "On the mass and spin-parity of the Higgs boson candidate via its decays to Z boson pairs." In: *Phys. Rev. Lett.* 110 (2013), p. 081803. DOI: 10.1103/PhysRevLett.110.081803. arXiv: 1212.6639 [hep-ex].

[60] Serguei Chatrchyan et al. "Measurement of the properties of a Higgs boson in the four-lepton final state." In: *Phys. Rev. D* 89 (2014), p. 092007. DOI: 10.1103/PhysRevD.89.092007. arXiv: 1312.5353 [hep-ex].

[61] Vardan Khachatryan et al. "Constraints on the spin-parity and anomalous HVV couplings of the Higgs boson in proton collisions at 7 and 8 TeV." In: *Phys. Rev. D* 92 (2015), p. 012004. DOI: 10.1103/PhysRevD.92.012004. arXiv: 1411.3441 [hep-ex].

[62] Vardan Khachatryan et al. "Limits on the Higgs boson lifetime and width from its decay to four charged leptons." In: *Phys. Rev. D* 92 (2015), p. 072010. DOI: 10.1103/PhysRevD.92.072010. arXiv: 1507.06656 [hep-ex].

[63] Vardan Khachatryan et al. "Combined search for anomalous pseudoscalar HVV couplings in VH ($H \to b\bar{b}$) production and $H \to VV$ decay." In: *Phys. Lett.*

B 759 (2016), p. 672. DOI: 10.1016/j.physletb.2016.06.004. arXiv: 1602.04305 [hep-ex].

[64] Albert M Sirunyan et al. "Constraints on anomalous Higgs boson couplings using production and decay information in the four-lepton final state." In: *Phys. Lett. B* 775 (2017), p. 1. DOI: 10.1016/j.physletb.2017.10.021. arXiv: 1707.00541 [hep-ex].

[65] Albert M Sirunyan et al. "Measurements of the Higgs boson width and anomalous HVV couplings from on-shell and off-shell production in the four-lepton final state." In: *Phys. Rev.* D99 (2019), p. 112003. DOI: 10.1103/PhysRevD.99.112003. arXiv: 1901.00174 [hep-ex].

[66] Albert M Sirunyan et al. "Constraints on anomalous HVV couplings from the production of Higgs bosons decaying to τ lepton pairs." In: *Phys. Rev.* D100 (2019), p. 112002. DOI: 10.1103/PhysRevD.100.112002. arXiv: 1903.06973 [hep-ex].

[67] Albert M Sirunyan et al. "Constraints on anomalous Higgs boson couplings to vector bosons and fermions in its production and decay using the four-lepton final state." In: *Phys. Rev. D* 104.5 (2021), p. 052004. DOI: 10.1103/PhysRevD.104.052004. arXiv: 2104.12152 [hep-ex].

[68] Armen Tumasyan et al. "Measurement of the Higgs boson width and evidence of its off-shell contributions to ZZ production." In: *Nature Phys.* 18.11 (2022), pp. 1329–1334. DOI: 10.1038/s41567-022-01682-0. arXiv: 2202.06923 [hep-ex].

[69] Armen Tumasyan et al. "Constraints on anomalous Higgs boson couplings to vector bosons and fermions from the production of Higgs bosons using the $\tau\tau$ final state." In: *Phys. Rev. D* 108.3 (2023), p. 032013. DOI: 10.1103/PhysRevD.108.032013. arXiv: 2205.05120 [hep-ex].

[70] Georges Aad et al. "Evidence for the spin-0 nature of the Higgs boson using ATLAS data." In: *Phys. Lett. B* 726 (2013), p. 120. DOI: 10.1016/j.physletb.2013.08.026. arXiv: 1307.1432 [hep-ex].

[71] Georges Aad et al. "Study of the spin and parity of the Higgs boson in diboson decays with the ATLAS detector." In: *Eur. Phys. J. C* 75 (2015), p. 476. DOI: 10.1140/epjc/s10052-015-3685-1. arXiv: 1506.05669 [hep-ex].

[72] Georges Aad et al. "Test of CP Invariance in vector-boson fusion production of the Higgs boson using the Optimal Observable method in the ditau decay channel with the ATLAS detector." In: *Eur. Phys. J. C* 76 (2016), p. 658. DOI: 10.1140/epjc/s10052-016-4499-5. arXiv: 1602.04516 [hep-ex].

[73] Morad Aaboud et al. "Measurement of inclusive and differential cross sections in the H $\to$ ZZ* $\to 4\ell$ decay channel in pp collisions at $\sqrt{s} = 13$ TeV with the ATLAS detector." In: *JHEP* 10 (2017), p. 132. DOI: 10.1007/JHEP10(2017)132. arXiv: 1708.02810 [hep-ex].

[74] Morad Aaboud et al. "Measurement of the Higgs boson coupling properties in the $H \to ZZ^* \to 4\ell$ decay channel at $\sqrt{s} = 13$ TeV with the ATLAS detector." In: *JHEP* 03 (2018), p. 095. DOI: 10.1007/JHEP03(2018)095. arXiv: 1712.02304 [hep-ex].

[75] Morad Aaboud et al. "Measurements of Higgs boson properties in the diphoton decay channel with 36 fb^{-1} of pp collision data at $\sqrt{s} = 13$ TeV with the ATLAS detector." In: *Phys. Rev. D* 98 (2018), p. 052005. DOI: 10.1103/PhysRevD.98.052005. arXiv: 1802.04146 [hep-ex].

[76] Georges Aad et al. "Higgs boson production cross-section measurements and their EFT interpretation in the 4ℓ decay channel at $\sqrt{s}$ =13 TeV with the ATLAS detector." In: *Eur. Phys. J. C* 80.10 (2020). [Erratum: Eur.Phys.J.C 81, 29 (2021), Erratum: Eur.Phys.J.C 81, 398 (2021)], p. 957. DOI: 10.1140/epjc/s10052-020-8227-9. arXiv: 2004.03447 [hep-ex].

[77] G. Aad et al. "Test of CP Invariance in Higgs Boson Vector-Boson-Fusion Production Using the H$\to \gamma\gamma$ Channel with the ATLAS Detector." In: *Phys. Rev. Lett.* 131.6 (2023), p. 061802. DOI: 10.1103/PhysRevLett.131.061802. arXiv: 2208.02338 [hep-ex].

[78] Georges Aad et al. "Test of CP-invariance of the Higgs boson in vector-boson fusion production and its decay into four leptons." In: (2023). arXiv: 2304.09612 [hep-ex].

[79] D. de Florian et al. *Handbook of LHC Higgs cross sections: 4. Deciphering the nature of the Higgs sector*. CERN Report CERN-2017-002-M. 2016. DOI: 10.23731/CYRM-2017-002. arXiv: 1610.07922 [hep-ph].

[80] Adam Falkowski. *Higgs Basis: Proposal for an EFT basis choice for LHC HXSWG*. Technical Report LHCHXSWG-INT-2015-001. https://cds.cern.ch/record/2001958. 2015.

[81] Andrei V. Gritsan, Jeffrey Roskes, Ulascan Sarica, Markus Schulze, Meng Xiao, and Yaofu Zhou. "New features in the JHU generator framework: constraining Higgs boson properties from on-shell and off-shell production." In: (2020). arXiv: 2002.09888 [hep-ph].

[82] Yanyan Gao, Andrei V. Gritsan, Zijin Guo, Kirill Melnikov, Markus Schulze, and Nhan V. Tran. "Spin determination of single-produced resonances at hadron colliders." In: *Phys. Rev. D* 81 (2010), p. 075022. DOI: 10.1103/PhysRevD.81.075022. arXiv: 1001.3396 [hep-ph].

[83] Sara Bolognesi, Yanyan Gao, Andrei V. Gritsan, Kirill Melnikov, Markus Schulze, Nhan V. Tran, and Andrew Whitbeck. "Spin and parity of a single-produced resonance at the LHC." In: *Phys. Rev. D* 86 (2012), p. 095031. DOI: 10.1103/PhysRevD.86.095031. arXiv: 1208.4018 [hep-ph].

[84] Ian Anderson, Sara Bolognesi, Fabrizio Caola, Yanyan Gao, Andrei V. Gritsan, Christopher B. Martin, Kirill Melnikov, Markus Schulze, Nhan V. Tran, Andrew Whitbeck, and Yaofu Zhou. "Constraining anomalous HVV interactions at proton and lepton colliders." In: *Phys. Rev. D* 89 (2014), p. 035007. DOI: 10.1103/PhysRevD.89.035007. arXiv: 1309.4819 [hep-ph].

[85] Andrei V. Gritsan, Raoul Röntsch, Markus Schulze, and Meng Xiao. "Constraining anomalous Higgs boson couplings to the heavy flavor fermions using matrix element techniques." In: *Phys. Rev. D* 94 (2016), p. 055023. DOI: 10.1103/PhysRevD.94.055023. arXiv: 1606.03107 [hep-ph].

[86] Till Martini, Ren-Qi Pan, Markus Schulze, and Meng Xiao. "Probing the CP structure of the top quark Yukawa coupling: Loop sensitivity versus on-shell sensitivity." In: *Phys. Rev. D* 104.5 (2021), p. 055045. DOI: 10.1103/PhysRevD.104.055045. arXiv: 2104.04277 [hep-ph].

[87] Steven Weinberg. "Baryon and Lepton Nonconserving Processes." In: *Phys. Rev. Lett.* 43 (1979), pp. 1566–1570. DOI: 10.1103/PhysRevLett.43.1566.

[88] W. Buchmuller and D. Wyler. "Effective Lagrangian Analysis of New Interactions and Flavor Conservation." In: *Nucl. Phys. B* 268 (1986), pp. 621–653. DOI: 10.1016/0550-3213(86)90262-2.

[89] Chung Ngoc Leung, S. T. Love, and S. Rao. "Low-Energy Manifestations of a New Interaction Scale: Operator Analysis." In: *Z. Phys. C* 31 (1986), p. 433. DOI: 10.1007/BF01588041.

[90] A. Dedes, W. Materkowska, M. Paraskevas, J. Rosiek, and K. Suxho. "Feynman rules for the Standard Model Effective Field Theory in R_ξ -gauges." In: *JHEP* 06 (2017), p. 143. DOI: 10.1007/JHEP06(2017)143. arXiv: 1704.03888 [hep-ph].

[91] B. Grzadkowski, M. Iskrzynski, M. Misiak, and J. Rosiek. "Dimension-Six Terms in the Standard Model Lagrangian." In: *JHEP* 10 (2010), p. 085. DOI: 10.1007/JHEP10(2010)085. arXiv: 1008.4884 [hep-ph].

[92] John M. Campbell and R. K. Ellis. "MCFM for the Tevatron and the LHC." In: *Nucl. Phys. B Proc. Suppl.* 205-206 (2010). Ed. by Johannes Blümlein, Sven-Olaf Moch, and Tord Riemann, pp. 10–15. DOI: 10.1016/j.nuclphysbps.2010.08.011. arXiv: 1007.3492 [hep-ph].

[93] John M. Campbell, R. Keith Ellis, and Ciaran Williams. "Vector boson pair production at the LHC." In: *JHEP* 07 (2011), p. 018. DOI: 10.1007/JHEP07(2011)018. arXiv: 1105.0020 [hep-ph].

[94] John M. Campbell, R. Keith Ellis, and Ciaran Williams. "Bounding the Higgs width at the LHC using full analytic results for $gg \to e^- e^+ \mu^- \mu^+$." In: *JHEP* 04 (2014), p. 060. DOI: 10.1007/JHEP04(2014)060. arXiv: 1311.3589 [hep-ph].

[95] John M. Campbell and R. Keith Ellis. "Higgs constraints from vector boson fusion and scattering." In: *JHEP* 04 (2015), p. 030. DOI: 10.1007/JHEP04(2015)030. arXiv: 1502.02990 [hep-ph].

[96] John M. Campbell, R. Keith Ellis, and Walter T. Giele. "A Multi-Threaded Version of MCFM." In: *Eur. Phys. J. C* 75.6 (2015), p. 246. DOI: 10.1140/epjc/s10052-015-3461-2. arXiv: 1503.06182 [physics.comp-ph].

[97] Serguei Chatrchyan et al. "Measurement of Higgs boson production and properties in the WW decay channel with leptonic final states." In: *JHEP* 01 (2014), p. 096. DOI: 10.1007/JHEP01(2014)096. arXiv: 1312.1129 [hep-ex].

[98] Vardan Khachatryan et al. "Constraints on the Higgs boson width from off-shell production and decay to Z-boson pairs." In: *Phys. Lett. B* 736 (2014), p. 64. DOI: 10.1016/j.physletb.2014.06.077. arXiv: 1405.3455 [hep-ex].

[99] Vardan Khachatryan et al. "Observation of the diphoton decay of the Higgs boson and measurement of its properties." In: *Eur. Phys. J. C* 74 (2014), p. 3076. DOI: 10.1140/epjc/s10052-014-3076-z. arXiv: 1407.0558 [hep-ex].

[100] Vardan Khachatryan et al. "Search for a Higgs boson in the mass range from 145 to 1000 GeV decaying to a pair of W or Z bosons." In: *JHEP* 10 (2015), p. 144. DOI: 10.1007/JHEP10(2015)144. arXiv: 1504.00936 [hep-ex].

[101] Albert M Sirunyan et al. "Measurements of $t\bar{t}H$ production and the CP structure of the Yukawa interaction between the Higgs boson and top quark in the diphoton decay channel." In: (2020). arXiv: 2003.10866 [hep-ex].

[102] Albert M Sirunyan et al. "Search for a new scalar resonance decaying to a pair of Z bosons in proton-proton collisions at $\sqrt{s} = 13\,\text{TeV}$." In: *JHEP* 06 (2018), p. 127. DOI: 10.1007/JHEP06(2018)127. arXiv: 1804.01939 [hep-ex].

[103] "Search for a heavy Higgs boson decaying to a pair of W bosons in proton-proton collisions at $\sqrt{s} = 13$ TeV." In: (2019).

[104] Albert M Sirunyan et al. "Constraints on anomalous Higgs boson couplings to vector bosons and fermions in its production and decay using the four-lepton final state." In: *Phys. Rev. D* 104.5 (2021), p. 052004. DOI: 10.1103/PhysRevD.104.052004. arXiv: 2104.12152 [hep-ex].

[105] Adam Falkowski, Benjamin Fuks, Kentarou Mawatari, Ken Mimasu, Francesco Riva, and Veronica Sanz. "Rosetta: an operator basis translator for Standard Model effective field theory." In: *Eur. Phys. J.* C75.12 (2015), p. 583. DOI: 10.1140/epjc/s10052-015-3806-x. arXiv: 1508.05895 [hep-ph].

[106] Yi Chen, Nhan Tran, and Roberto Vega-Morales. "Scrutinizing the Higgs signal and background in the $2e2\not{p}$ golden channel." In: *JHEP* 01 (2013), p. 182. DOI: 10.1007/JHEP01(2013)182. arXiv: 1211.1959 [hep-ph].

[107] Yi Chen, Roni Harnik, and Roberto Vega-Morales. "Probing the Higgs Couplings to Photons in $h \to 4\ell$ at the LHC." 2014. arXiv: 1404.1336 [hep-ph].

[108] L3 Collaboration. "Search for anomalous couplings in the higgs sector at lep." In: *Phys. Lett. B* 589 (2004), pp. 89–102. DOI: 10.1016/j.physletb.2004.03.048. arXiv: 04.03037 [hep-ph].

[109] H. Khanpour, S. Khatibi, and M. Mohammadi Najafabadi. "Probing higgs boson couplings in h+γ production at the lhc." In: *Phys. Lett. B* 773 (2017), pp. 462–469. DOI: 10.1016/j.physletb.2017.09.005. arXiv: 1702.05753 [hep-ph].

[110] Liaoshan Shi, Zhijun Liang, Bo Liu, and Zhenhui He. "Constraining the anomalous Higgs boson coupling in $H+\gamma$ production." In: *Chin. Phys. C* 43.4 (2019), p. 043001. DOI: 10.1088/1674-1137/43/4/043001. arXiv: 1811.02261 [hep-ph].

[111] Abdelhak Djouadi, Jan Kalinowski, Margarete Muehlleitner, and Michael Spira. "HDECAY: Twenty$_{++}$ years after." In: *Comput. Phys. Commun.* 238 (2019), pp. 214–231. DOI: 10.1016/j.cpc.2018.12.010. arXiv: 1801.09506 [hep-ph].

[112] Duarte Fontes, Margarete Muhlleitner, Jorge C. Romao, Rui Santos, Joao P. Silva, and Jonas Wittbrodt. "The C2HDM revisited." In: *JHEP* 02 (2018), p. 073. DOI: 10.1007/JHEP02(2018)073. arXiv: 1711.09419 [hep-ph].

[113] Ian Low, Joseph Lykken, and Gabe Shaughnessy. "Have We Observed the Higgs (Imposter)?" In: *Phys. Rev. D* 86 (2012), p. 093012. DOI: 10.1103/PhysRevD.86.093012. arXiv: 1207.1093 [hep-ph].

[114] Roberto Contino, Margherita Ghezzi, Christophe Grojean, Margarete Mühlleitner, and Michael Spira. "eHDECAY: an Implementation of the Higgs Effective Lagrangian into HDECAY." In: *Comput. Phys. Commun.* 185 (2014), pp. 3412–3423. DOI: 10.1016/j.cpc.2014.06.028. arXiv: 1403.3381 [hep-ph].

[115] Ilaria Brivio, Yun Jiang, and Michael Trott. "The SMEFTsim package, theory and tools." In: *JHEP* 12 (2017), p. 070. DOI: 10.1007/JHEP12(2017)070. arXiv: 1709.06492 [hep-ph].

[116] J. Alwall, R. Frederix, S. Frixione, V. Hirschi, F. Maltoni, O. Mattelaer, H. S. Shao, T. Stelzer, P. Torrielli, and M. Zaro. "The automated computation of tree-level and next-to-leading order differential cross sections, and their matching to parton shower simulations." In: *JHEP* 07 (2014), p. 079. DOI: 10.1007/JHEP07(2014)079. arXiv: 1405.0301 [hep-ph].

[117] Ansgar Denner, Stefan Dittmaier, and Alexander Mück. "PROPHECY4F 3.0: A Monte Carlo program for Higgs-boson decays into four-fermion final states in and beyond the Standard Model." In: *Comput. Phys. Commun.* 254 (2020), p. 107336. DOI: 10.1016/j.cpc.2020.107336. arXiv: 1912.02010 [hep-ph].

[118] Ansgar Denner, Stefan Dittmaier, Stefan Kallweit, and Alexander Mück. "HAWK 2.0: A Monte Carlo program for Higgs production in vector-boson fusion and Higgs strahlung at hadron colliders." In: *Comput. Phys. Commun.* 195 (2015), pp. 161–171. DOI: 10.1016/j.cpc.2015.04.021. arXiv: 1412.5390 [hep-ph].

[119] P. A. Zyla et al. "Review of Particle Physics." In: *PTEP* 2020.8 (2020), p. 083C01. DOI: 10.1093/ptep/ptaa104.

[120] Richard D. Ball et al. "Parton distributions for the LHC Run II." In: *JHEP* 04 (2015), p. 040. DOI: 10.1007/JHEP04(2015)040. arXiv: 1410.8849 [hep-ph].

[121] Serguei Chatrchyan et al. "Measurement of the weak mixing angle with the Drell-Yan process in proton-proton collisions at the LHC." In: *Phys. Rev. D* 84 (2011), p. 112002. DOI: 10.1103/PhysRevD.84.112002. arXiv: 1110.2682 [hep-ex].

[122] A. Bredenstein et al. "Precise predictions for the Higgs-boson decay H $\to$ WW/ZZ $\to$ 4 leptons." In: *Phys. Rev. D* 74 (2006), p. 013004. DOI: 10.1103/PhysRevD.74.013004. arXiv: hep-ph/0604011.

[123] Ansgar Denner, Stefan Dittmaier, Stefan Kallweit, and Alexander Muck. "Electroweak corrections to Higgs-strahlung off W/Z bosons at the Tevatron and the LHC with HAWK." In: *JHEP* 03 (2012), p. 075. DOI: 10.1007/JHEP03(2012)075. arXiv: 1112.5142 [hep-ph].

[124] J. Alwall et al. "A Standard format for Les Houches event files." In: *Comput. Phys. Commun.* 176 (2007), pp. 300–304. DOI: 10.1016/j.cpc.2006.11.010. arXiv: hep-ph/0609017.

[125] Federico Granata, Jonas M. Lindert, Carlo Oleari, and Stefano Pozzorini. "NLO QCD+EW predictions for HV and HV +jet production including parton-shower effects." In: *JHEP* 09 (2017), p. 012. DOI: 10.1007/JHEP09(2017)012. arXiv: 1706.03522 [hep-ph].

[126] Georges Aad et al. "Test of CP invariance in vector-boson fusion production of the Higgs boson in the $H \to \tau\tau$ channel in proton−proton collisions at $\sqrt{s} =$ 13 TeV with the ATLAS detector." In: (2020). arXiv: 2002.05315 [hep-ex].

[127] A.V. Gritsan and the Particle Data Group. "Polarization in B decays." In: *Review of Particle Physics* 110 (2024). https://pdg.lbl.gov/2024/reviews/rpp2024-rev-b-decays-polarization.pdf, p. 030001. DOI: 10.1103/PhysRevD.110.030001.

[128] Bernard Aubert et al. "Vector-tensor and vector-vector decay amplitude analysis of $B^0 \to \phi$ K*0." In: *Phys. Rev. Lett.* 98 (2007), p. 051801. DOI: 10.1103/PhysRevLett.98.051801. arXiv: hep-ex/0610073 [hep-ex].

[129] J. A. Aguilar-Saavedra, A. Bernal, J. A. Casas, and J. M. Moreno. "Testing entanglement and Bell inequalities in $H \to ZZ$." In: *Phys. Rev. D* 107.1 (2023), p. 016012. DOI: 10.1103/PhysRevD.107.016012. arXiv: 2209.13441 [hep-ph].

[130] Dorival Gonçalves, Ajay Kaladharan, Frank Krauss, and Alberto Navarro. "Quantum Entanglement is Quantum: ZZ Production at the LHC." In: (2025). arXiv: 2505.12125 [hep-ph].

[131] S. A. Abel, M. Dittmar, and Herbert K. Dreiner. "Testing locality at colliders via Bell's inequality?" In: *Phys. Lett. B* 280 (1992), pp. 304–312. DOI: 10.1016/0370-2693(92)90071-B.

[132] Philip Bechtle, Cedric Breuning, Herbi K. Dreiner, and Claude Duhr. "A critical appraisal of tests of locality and of entanglement versus non-entanglement at colliders." In: (2025). arXiv: 2507.15947 [hep-ph].

[133] Steven A. Abel, Herbi K. Dreiner, Rhitaja Sengupta, and Lorenzo Ubaldi. "Colliders are Testing neither Locality via Bell's Inequality nor Entanglement versus Non-Entanglement." In: (2025). arXiv: 2507.15949 [hep-ph].

[134] Albert Einstein, Boris Podolsky, and Nathan Rosen. "Can quantum mechanical description of physical reality be considered complete?" In: *Phys. Rev.* 47 (1935), pp. 777–780. DOI: 10.1103/PhysRev.47.777.

[135] David Bohm. "A Suggested interpretation of the quantum theory in terms of hidden variables. 1." In: *Phys. Rev.* 85 (1952), pp. 166–179. DOI: 10.1103/PhysRev.85.166.

[136] Daniel Collins, Nicolas Gisin, Noah Linden, Serge Massar, and Sandu Popescu. "Bell Inequalities for Arbitrarily High-Dimensional Systems." In: *Phys. Rev. Lett.* 88.4 (2002), p. 040404. DOI: 10.1103/PhysRevLett.88.040404.

[137] J. S. Bell. "On the Einstein-Podolsky-Rosen paradox." In: *Physics Physique Fizika* 1 (1964), pp. 195–200. DOI: 10.1103/PhysicsPhysiqueFizika.1.195.

[138] Jeffrey Davis, Andrei V. Gritsan, Lucas S. Mandacaru Guerra, Savvas Kyriacou, Jeffrey Roskes, and Markus Schulze. "Constraining anomalous Higgs boson couplings to virtual photons." In: *Phys. Rev. D* 105.9 (2022), p. 096027. DOI: 10.1103/PhysRevD.105.096027. arXiv: 2109.13363 [hep-ph].

[139] John M. Campbell and R. K. Ellis. "MCFM for the Tevatron and the LHC." In: *Nucl. Phys. Proc. Suppl.* 205-206 (2010), p. 10. DOI: 10.1016/j.nuclphysbps.2010.08.011. arXiv: 1007.3492 [hep-ph].

[140] Stefano Frixione, Paolo Nason, and Carlo Oleari. "Matching NLO QCD computations with parton shower simulations: the POWHEG method." In: *JHEP* 11 (2007), p. 070. DOI: 10.1088/1126-6708/2007/11/070. arXiv: 0709.2092 [hep-ph].

[141] E. Bagnaschi, G. Degrassi, P. Slavich, and A. Vicini. "Higgs production via gluon fusion in the POWHEG approach in the SM and in the MSSM." In: *JHEP* 02 (2012), p. 088. DOI: 10.1007/JHEP02(2012)088. arXiv: 1111.2854 [hep-ph].

[142] Paolo Nason and Carlo Oleari. "NLO Higgs boson production via vector-boson fusion matched with shower in POWHEG." In: *JHEP* 02 (2010), p. 037. DOI: 10.1007/JHEP02(2010)037. arXiv: 0911.5299 [hep-ph].

[143] Gionata Luisoni, Paolo Nason, Carlo Oleari, and Francesco Tramontano. "$HW^{\pm}/HZ$ + 0 and 1 jet at NLO with the POWHEG BOX interfaced to GoSam and their merging within MiNLO." In: *JHEP* 10 (2013), p. 083. DOI: 10.1007/JHEP10(2013)083. arXiv: 1306.2542 [hep-ph].

[144] Heribertus B. Hartanto, Barbara Jager, Laura Reina, and Doreen Wackeroth. "Higgs boson production in association with top quarks in the POWHEG BOX." In: *Phys. Rev. D* 91 (2015), p. 094003. DOI: 10.1103/PhysRevD.91.094003. arXiv: 1501.04498 [hep-ph].

[145] Massimiliano Grazzini, Stefan Kallweit, and Dirk Rathlev. "ZZ production at the LHC: fiducial cross sections and distributions in NNLO QCD." In: *Phys. Lett. B* 750 (2015), p. 407. DOI: 10.1016/j.physletb.2015.09.055. arXiv: 1507.06257 [hep-ph].

[146] Stefan Gieseke, Tobias Kasprzik, and Johann H. Kuehn. "Vector-boson pair production and electroweak corrections in HERWIG++." In: *Eur. Phys. J. C* 74 (2014), p. 2988. DOI: 10.1140/epjc/s10052-014-2988-y. arXiv: 1401.3964 [hep-ph].

[147] Julien Baglio, Le Duc Ninh, and Marcus M. Weber. "Massive gauge boson pair production at the LHC: a next-to-leading order story." In: *Phys. Rev. D* 88 (2013). [Erratum: doi:10.1103/PhysRevD.94.099902], p. 113005. DOI: 10.1103/PhysRevD.88.113005. arXiv: 1307.4331 [hep-ph].

[148] Federico Demartin, Fabio Maltoni, Kentarou Mawatari, Ben Page, and Marco Zaro. "Higgs characterisation at NLO in QCD: CP properties of the top-quark Yukawa interaction." In: *Eur. Phys. J.* C74 (2014), p. 3065. DOI: 10.1140/epjc/s10052-014-3065-2. arXiv: 1407.5089 [hep-ph].

[149] Richard D. Ball, Valerio Bertone, Francesco Cerutti, Luigi Del Debbio, Stefano Forte, Alberto Guffanti, Jose I. Latorre, Juan Rojo, and Maria Ubiali. "Unbiased global determination of parton distributions and their uncertainties at NNLO and at LO." In: *Nucl. Phys. B* 855 (2012), p. 153. DOI: 10.1016/j.nuclphysb.2011.09.024. arXiv: 1107.2652 [hep-ph].

[150] Torbjörn Sjöstrand, Stefan Ask, Jesper R. Christiansen, Richard Corke, Nishita Desai, Philip Ilten, Stephen Mrenna, Stefan Prestel, Christine O. Rasmussen, and Peter Z. Skands. "An introduction to PYTHIA 8.2." In: *Comput. Phys. Commun.* 191 (2015), p. 159. DOI: 10.1016/j.cpc.2015.01.024. arXiv: 1410.3012 [hep-ph].

[151] S. Agostinelli et al. "GEANT4 – a simulation toolkit." In: *Nucl. Instrum. Meth. A* 506 (2003), p. 250. DOI: 10.1016/S0168-9002(03)01368-8.

[152] Albert M Sirunyan et al. "Measurements of properties of the Higgs boson decaying into the four-lepton final state in pp collisions at $\sqrt{s} = 13\,\text{TeV}$." In: *JHEP* 11 (2017), p. 047. DOI: 10.1007/JHEP11(2017)047. arXiv: 1706.09936 [hep-ex].

[153] Albert M Sirunyan et al. "Measurements of production cross sections of the Higgs boson in the four-lepton final state in proton–proton collisions at $\sqrt{s} =$ 13 TeV." In: *Eur. Phys. J. C* 81.6 (2021), p. 488. DOI: 10.1140/epjc/s10052-021-09200-x. arXiv: 2103.04956 [hep-ex].

[154] Roger J. Barlow. "Extended maximum likelihood." In: *Nucl. Instrum. Meth. A* 297 (1990), p. 496. DOI: 10.1016/0168-9002(90)91334-8.

[155] Aram Hayrapetyan et al. "The CMS Statistical Analysis and Combination Tool: Combine." In: *Comput. Softw. Big Sci.* 8.1 (2024), p. 19. DOI: 10.1007/s41781-024-00121-4. arXiv: 2404.06614 [physics.data-an].

[156] Wouter Verkerke and David P. Kirkby. "The RooFit toolkit for data modeling." In: *13th International Conference for Computing in High-Energy and Nuclear Physics (CHEP03)*. CHEP-2003-MOLT007. 2003. arXiv: physics/0306116 [physics].

[157] R. Brun and F. Rademakers. "ROOT: An object oriented data analysis framework." In: *Nucl. Instrum. Meth. A* 389 (1997), p. 81. DOI: 10.1016/S0168-9002(97)00048-X.

[158] S. S. Wilks. "The large-sample distribution of the likelihood ratio for testing composite hypotheses." In: *Annals Math. Statist.* 9 (1938), p. 60. DOI: 10.1214/aoms/1177732360.

[159] Georges Aad et al. "Evidence for the Higgs Boson Decay to a Z Boson and a Photon at the LHC." In: *Phys. Rev. Lett.* 132.2 (2024), p. 021803. DOI: 10.1103/PhysRevLett.132.021803. arXiv: 2309.03501 [hep-ex].

[160] Aram Hayrapetyan et al. "Observation of WWγ production and search for Hγ production in proton-proton collisions at $\sqrt{s} = 13$ TeV." In: *Phys. Rev. Lett.* 132.12 (2024), p. 121901. DOI: 10.1103/PhysRevLett.132.121901. arXiv: 2310.05164 [hep-ex].

[161] Albert M Sirunyan et al. "Search for narrow Hγ resonances in proton-proton collisions at $\sqrt{s} = 13$ TeV." In: *Phys. Rev. Lett.* 122.8 (2019), p. 081804. DOI: 10.1103/PhysRevLett.122.081804. arXiv: 1808.01257 [hep-ex].

[162] Morad Aaboud et al. "Search for heavy resonances decaying to a photon and a hadronically decaying $Z/W/H$ boson in pp collisions at $\sqrt{s} = 13$ TeV

with the ATLAS detector." In: *Phys. Rev. D* 98.3 (2018), p. 032015. DOI: 10.1103/PhysRevD.98.032015. arXiv: 1805.01908 [hep-ex].

[163] Georges Aad et al. "Search for heavy resonances decaying into a photon and a hadronically decaying Higgs boson in pp collisions at $\sqrt{s} = 13$ TeV with the ATLAS detector." In: *Phys. Rev. Lett.* 125 (2020), p. 251802. DOI: 10.1103/PhysRevLett.125.251802. arXiv: 2008.05928 [hep-ex].

[164] Ali Abbasabadi, David Bowser-Chao, Duane A. Dicus, and Wayne W. Repko. "Higgs - photon associated production at hadron colliders." In: *Phys. Rev. D* 58 (1998), p. 057301. DOI: 10.1103/PhysRevD.58.057301. arXiv: hep-ph/9706335.

[165] Ilaria Brivio. "SMEFTsim 3.0 — a practical guide." In: *JHEP* 04 (2021), p. 073. DOI: 10.1007/JHEP04(2021)073. arXiv: 2012.11343 [hep-ph].

[166] J. Alwall, R. Frederix, S. Frixione, V. Hirschi, F. Maltoni, O. Mattelaer, H. S. Shao, T. Stelzer, P. Torrielli, and M. Zaro. "The automated computation of tree-level and next-to-leading order differential cross sections, and their matching to parton shower simulations." In: *JHEP* 2014 (2014). DOI: 10.1007/jhep07(2014)079. arXiv: 1405.0301.

[167] Lukas Allwicher, Darius A. Faroughy, Florentin Jaffredo, Olcyr Sumensari, and Felix Wilsch. "Drell-Yan tails beyond the Standard Model." In: *JHEP* 03 (2023), p. 064. DOI: 10.1007/JHEP03(2023)064. arXiv: 2207.10714 [hep-ph].

[168] Albert M Sirunyan et al. "Electron and photon reconstruction and identification with the CMS experiment at the CERN LHC." In: *JINST* 16.05 (2021). DOI: 10.1088/1748-0221/16/05/P05014.

[169] Glen Cowan, Kyle Cranmer, Eilam Gross, and Ofer Vitells. "Asymptotic formulae for likelihood-based tests of new physics." In: *Eur. Phys. J. C* 71 (2011). [Erratum: Eur.Phys.J.C 73, 2501 (2013)], p. 1554. DOI: 10.1140/epjc/s10052-011-1554-0. arXiv: 1007.1727 [physics.data-an].

[170] Thomas Junk. "Confidence level computation for combining searches with small statistics." In: *Nucl. Instrum. Meth. A* 434 (1999), p. 435. DOI: 10.1016/S0168-9002(99)00498-2. arXiv: hep-ex/9902006 [hep-ex].

[171] A. L. Read. "Presentation of search results: the CL_s technique." In: *J. Phys. G* 28 (2002), p. 2693. DOI: 10.1088/0954-3899/28/10/313.

[172] J. A. Aguilar-Saavedra, J. M. Cano, and J. M. No. "More light on Higgs flavor at the LHC: Higgs boson couplings to light quarks through $h + \gamma$ production." In: *Phys. Rev. D* 103.9 (2021), p. 095023. DOI: 10.1103/PhysRevD.103.095023. arXiv: 2008.12538 [hep-ph].

[173] Yaofu Zhou. "Constraining the Higgs boson coupling to light quarks in the $H \to ZZ$ final states." In: *Phys. Rev. D* 93 (2016), p. 013019. DOI: 10.1103/PhysRevD.93.013019. arXiv: 1505.06369 [hep-ph].

[174] Yaofu Zhou. "Probing Anomalous Couplings of the Higgs Boson to Weak Bosons and Fermions with Precision Calculations." CERN-THESIS-2019-007. PhD thesis. Johns Hopkins University, 2019.

[175] Elisa Balzani, Ramona Gröber, and Marco Vitti. "Light-quark Yukawa couplings from off-shell Higgs production." In: *JHEP* 10 (2023), p. 027. DOI: 10.1007/JHEP10(2023)027. arXiv: 2304.09772 [hep-ph].

[176] Fady Bishara, Ulrich Haisch, Pier Francesco Monni, and Emanuele Re. "Constraining Light-Quark Yukawa Couplings from Higgs Distributions." In: *Phys. Rev. Lett.* 118.12 (2017), p. 121801. DOI: 10.1103/PhysRevLett.118.121801. arXiv: 1606.09253 [hep-ph].

[177] Georges Aad et al. "Measurement of the total and differential Higgs boson production cross-sections at $\sqrt{s} = 13$ TeV with the ATLAS detector by combining the H $\to$ ZZ$^*\to$ 4ℓ and H $\to \gamma\gamma$ decay channels." In: *JHEP* 05 (2023), p. 028. DOI: 10.1007/JHEP05(2023)028. arXiv: 2207.08615 [hep-ex].

[178] Aram Hayrapetyan et al. "Measurements of inclusive and differential cross sections for the Higgs boson production and decay to four-leptons in proton-proton collisions at $\sqrt{s} = 13$ TeV." In: *JHEP* 08 (2023), p. 040. DOI: 10.1007/JHEP08(2023)040. arXiv: 2305.07532 [hep-ex].

[179] Geoffrey T. Bodwin, Frank Petriello, Stoyan Stoynev, and Mayda Velasco. "Higgs boson decays to quarkonia and the $H\bar{c}c$ coupling." In: *Phys. Rev. D* 88.5 (2013), p. 053003. DOI: 10.1103/PhysRevD.88.053003. arXiv: 1306.5770 [hep-ph].

[180] Armen Tumasyan et al. "Search for Higgs Boson Decay to a Charm Quark-Antiquark Pair in Proton-Proton Collisions at s=13 TeV." In: *Phys. Rev. Lett.*

131.6 (2023), p. 061801. DOI: 10.1103/PhysRevLett.131.061801. arXiv: 2205.05550 [hep-ex].

[181] Georges Aad et al. "Direct constraint on the Higgs-charm coupling from a search for Higgs boson decays into charm quarks with the ATLAS detector." In: *Eur. Phys. J. C* 82 (2022), p. 717. DOI: 10.1140/epjc/s10052-022-10588-3. arXiv: 2201.11428 [hep-ex].

[182] Georges Aad et al. "A detailed map of Higgs boson interactions by the ATLAS experiment ten years after the discovery." In: *Nature* 607.7917 (2022). [Erratum: Nature 612, E24 (2022)], pp. 52–59. DOI: 10.1038/s41586-022-04893-w. arXiv: 2207.00092 [hep-ex].

[183] Armen Tumasyan et al. "A portrait of the Higgs boson by the CMS experiment ten years after the discovery." In: *Nature* 607.7917 (2022). [Erratum: Nature 623, (2023)], pp. 60–68. DOI: 10.1038/s41586-022-04892-x. arXiv: 2207.00043 [hep-ex].

[184] Michael Spira. "QCD effects in Higgs physics." In: *Fortsch. Phys.* 46 (1998), pp. 203–284. DOI: 10.1002/(SICI)1521-3978(199804)46:3<203::AID-PROP203>3.0.CO;2-4. arXiv: hep-ph/9705337.

[185] Guo-yuan Huang and Shun Zhou. "Precise Values of Running Quark and Lepton Masses in the Standard Model." In: *Phys. Rev. D* 103.1 (2021), p. 016010. DOI: 10.1103/PhysRevD.103.016010. arXiv: 2009.04851 [hep-ph].

[186] Robert V. Harlander, Stefan Liebler, and Hendrik Mantler. "SusHi: A program for the calculation of Higgs production in gluon fusion and bottom-quark annihilation in the Standard Model and the MSSM." In: *Comput. Phys. Commun.* 184 (2013), pp. 1605–1617. DOI: 10.1016/j.cpc.2013.02.006. arXiv: 1212.3249 [hep-ph].

[187] Robert V. Harlander. "Higgs production in heavy quark annihilation through next-to-next-to-leading order QCD." In: *Eur. Phys. J. C* 76.5 (2016), p. 252. DOI: 10.1140/epjc/s10052-016-4093-x. arXiv: 1512.04901 [hep-ph].

[188] Georges Aad et al. "Evidence of off-shell Higgs boson production from ZZ leptonic decay channels and constraints on its total width with the ATLAS detector." In: *Phys. Lett. B* 846 (2023). [Erratum: Phys.Lett.B 854, 138734

(2024)], p. 138223. DOI: 10.1016/j.physletb.2024.138734. arXiv: 2304.01532 [hep-ex].

[189] Aram Hayrapetyan et al. "Measurement of the Higgs boson mass and width using the four-lepton final state in proton-proton collisions at s=13 TeV." In: *Phys. Rev. D* 111.9 (2025), p. 092014. DOI: 10.1103/PhysRevD.111.092014. arXiv: 2409.13663 [hep-ex].

[190] Ilaria Brivio et al. "Truncation, validity, uncertainties." In: (2022). arXiv: 2201.04974 [hep-ph].

[191] Ulrich Haisch and Gabriël Koole. "Off-shell Higgs production at the LHC as a probe of the trilinear Higgs coupling." In: *JHEP* 02 (2022), p. 030. DOI: 10.1007/JHEP02(2022)030. arXiv: 2111.12589 [hep-ph].

[192] Aram Hayrapetyan et al. "Determination of the spin and parity of all-charm tetraquarks." In: (2025). arXiv: 2506.07944 [hep-ex].